FERROMAGNETIC RESONANCE STUDY OF MAGNETIC FILMS VIA TRANSMISSION LINE PERTURBATION AND ELECTRICAL METHODS

SOH WEE TEE

NATIONAL UNIVERSITY OF SINGAPORE

2016

FERROMAGNETIC RESONANCE STUDY OF MAGNETIC FILMS VIA TRANSMISSION LINE PERTURBATION AND ELECTRICAL METHODS

SOH WEE TEE
(B. Sc. (Hons.), National University of Singapore, Singapore)

A THESIS SUBMITTED
FOR THE DEGREE OF DOCTOR OF PHILOSOPHY
DEPARTMENT OF PHYSICS
NATIONAL UNIVERSITY OF SINGAPORE

2016

Declaration

I hereby declare that this thesis is my original work and it has been written by me in its entirety. I have duly acknowledged all the sources of information which have been used in the thesis.

This thesis has also not been submitted for any degree in any university previously.

Soh Wee Tee

Digitally signed by Soh Wee Tee
DN: cn=Soh Wee Tee, o, ou, email=a0046479@u.nus.edu, c=SG
Date: 2016.11.14 15:12:52 +08'00'

Soh Wee Tee

11 November 2016

“And ye shall seek me, and find me, when ye shall search for me with all your heart.”

Acknowledgements

As with all good things that usually must come to an end, this thesis concludes the last four years of my fulfilling and experiential journey in research. Firstly, all of this would not have been possible without the opportunity offered to me by my supervisor, Prof Ong Chong Kim, to conduct my research in his lab under his constant and patient guidance. Outside of research, Prof Ong had also been a great mentor and inspiration to me. I also thank my co-supervisor, Dr Tan Chin Yaw for his constant support and advice in both my research as well as my modules. I also extend my gratitude to Dr Nguyen N. Phuoc for all his advice and help with regards to film deposition, and to my fellow labmates Loo Yoke Leng and Wang Haigang for their company and support. I would also like to thank Dr Yakovlev Nikolai and Daniel Tay Zhi Jian for their help in Magnto-optical Kerr effect measurements.

Throughout these last four years, I am also immensely lucky and honoured to have the support, company, and guidance from various visiting research fellows and students, without whom I would be all alone and quite lonely in lab. In particular, I am grateful to Dr Bin Peng for his guidance when he had been attached to our lab, and also for his continued support even after his return to China. I am also thankful to Dr Chai Guozhi, Dr Sun Weiqiang, Dr Wu Zhe, Dr Zhong Xiaoxi, Dr Zhao Qiang, Feng Tao and Liu Yichao for their company and support during my candidature.

Finally, I would like to thank my family for their support and encouragement throughout my candidature, without which none of this would have been even possible.

Table of Contents

Summary

This thesis examines two main methods to characterise the dynamic properties of magnetic thin film systems: transmission line perturbation and electrical methods. Firstly, using the transmission line perturbation method, we studied the magnetisation dynamics of NiFe films with and without stripe domains. Our results highlighted some of the unique features of stripe domains in these films, notably a field-dependent rotatable anisotropy field. Secondly, using the electrical detection of ferromagnetic resonance (FMR) based on spin rectification effect (SRE), we demonstrated that both the dynamic magnetic properties and magneto-transport properties of magnetic films can be simultaneously detected and quantified accurately. We also propose a method to accurately separate SRE from inverse Spin Hall effect-induced voltages in NiFe/Pt bilayers. Finally, we extend the method for local electrical measurements of spin dynamics with a shorted-coaxial probe, and demonstrate how SRE can be used to separate and quantify both the static and dynamic magnetic dipolar fields due to oscillating spins.

List of tables

Page

List of figures

Page

List of Acronyms

AMR	Anisotropic magneto-resistance
AHE	Anomalous Hall effect
CPW	Coplanar waveguide
FMR	Ferromagnetic resonance
IREE	Inverse Rashba-Edelstein effect
ISHE	Inverse spin Hall effect
LLG	Landau–Lifshitz–Gilbert
MAMR	Microwave-assisted magnetisation reversal
MEMS	Micro-Electro Mechanical Systems
MFM	Magnetic force microscopy
MSSW	Magnetostatic surface spin wave
MSBVSW	Magnetostatic backward volume spin waves
SGE	Spin galvanic effect
SHE	Spin Hall effect
SRE	Spin rectification effect
SSE	Spin Seeback effect
STO	Spin torque oscillator
STT	Spin torque transfer
VNA	Vector network analyzer
VSM	Vibrating sample magnetometer
XRD	X-Ray Diffraction
YIG	Yttrium iron garnet

1 Introduction

Magnetic thin films[1-3] play integral roles in high frequency microwave devices today, insofar as having enormous applications ranging from information storage to communication devices. At microwave frequencies, due to the electronic screening effect, microwaves cannot permeate significantly more than the skin depth from the surface of a metallic film, a point which renders a thin film structure more suitable than bulk and is conveniently in line with the push for miniaturization in today's high-tech industry. The high frequency applicability of magnetic thin films is determined by both their static response, such as saturation magnetisation, static permeability and coercivity, as well as by their dynamic response, such as complex permeability and damping mechanisms. While their desired properties depend on the specific application, it is in general desirable to have a large saturation magnetisation, low coercivity, high permeability in a wide-frequency range as well as low damping. Crucially, a large ferromagnetic resonance (FMR) frequency greater than a few gigahertz (GHz) is required in practice, since the dynamic magnetic response (positive, real permeability) falls off rapidly as the working frequency increases above FMR frequency.

As such, an important research focus is the push for high zero-field FMR frequencies as well as its wide-band tunability while maintaining desirable static and dynamic magnetic properties. At the same time, magnetic damping which relates to relaxation timescales and switching responses must also be well-understood and controlled. Soft ferromagnetic films, particularly NiFe (Permalloy)[4-8] and FeCo[9-14] have been quite extensively studied over the past decades. Generally, both ferromagnetic alloys possess high saturation magnetisation (typically 10 kG for NiFe and 18 kG for FeCo) and relatively low intrinsic damping (around 0.01). Having almost zero magneto-crystalline anisotropy, their zero-field FMR frequency

can also be easily tuned by manipulating the different magnetic anisotropies via various techniques such as oblique deposition, exchange bias and doping, and hence are attractive candidates for realizing low loss, wide-band tunable devices. Both ferromagnetic alloys have also been studied and well-utilized in spintronics research, particularly being used as spin current sources via spin pumping[15,16] and spin Seebeck effect (SSE)[17], and even as spin current detectors via the spin Hall effect (SHE)[18].

Driven by the need for tailoring magnetic properties to various microwave applications, it is also of high importance that sensitive and accurate methods for the high frequency characterisation of magnetic thin films are readily made available. Because the volume of the film is extremely small compared to that of the substrate, an accurate, sensitive and convenient characterisation technique can pose a significant challenge for the industry. Three main methods are currently employed for this purpose: pick-up coil method, transmission line perturbation method and electrical methods via magneto-resistance.

The pick-up coil method[19] mainly consists of detecting the flux linkage changes between a pick-up coil and another coil with a magnetic sample placed within, which requires inductive coupling between the sample and pickup coils. Unwanted effects from electric fields produces noise, while such long-distance inductive coupling is also highly susceptible to outside noise, thus is generally unsuitable for small samples and very thin films. This method is reliable and accurate at lower MHz frequencies, but becomes much less sensitive at higher GHz frequencies due to its large sizes leading to spurious resonance effects.

In the transmission line perturbation method[20], a magnetic sample placed near a transmission line changes its characteristic impedance perturbatively (keeping the propagation mode largely unchanged), this changes are measured by a vector network analyzer (VNA) from which the sample's permeability can be calculated by circuit analysis.

Planar transmission lines such as microstrip and coplanar waveguide (CPW) are mostly used for films on flat substrates, and allows for wide range frequency measurements limited only by the transmission line propagation characteristics. The sample-transmission line coupling and setup is usually more contained and compact than in a pick-up coil method, and can thus allow for a more sensitive and accurate measurement of the frequency-dependent complex permeability.

The electrical method[21] for measuring FMR has generated substantial research interest recently, due to its high sensitivity to magnetisation dynamics as well as having direct implications to many spintronics applications. It involves electric current-to-magnetoresistance coupling, whereby an oscillating magnetisation at FMR results in an oscillating magneto-resistance which can be subsequently detected by means such as rectification with an ac current (spin rectification effect), which is the main theme of this thesis. Because the electric current is obviously totally confined within the conducting sample, this method is the most contained and compact in terms of vicinity noise elimination, and hence can be extremely sensitive to magnetisation dynamics. A further advantage of the electrical method is that the magneto-transport properties relating to the corresponding magneto-resistance such as anisotropic magneto-resistance[22] (AMR) and anomalous Hall effect[23] (AHE) can be simultaneously characterised simply by geometry considerations.

In this dissertation, we will focus on the shorted microstrip perturbation method and the electrical method based on spin rectification effect (SRE) to investigate a variety of interesting magnetic systems, with a focus on their impact to the field of spintronics. In spintronics, where spin current phenomena mediated by conduction electrons is involved, electrical detection of magnetisation statics and dynamics is usually much more appropriate

and advantageous than inductive methods. We shall briefly describe the theory behind the above two methods below.

1.1 Shorted microstrip perturabation method

The shorted microstrip perturbation method is based on a homemade[20] microstrip fixture developed in our lab that improves upon the reflection approach first proposed by Bekker *et al*[24] in 2005. This one-port reflection approach is much simpler to analyze than the two-port, transmission approach.

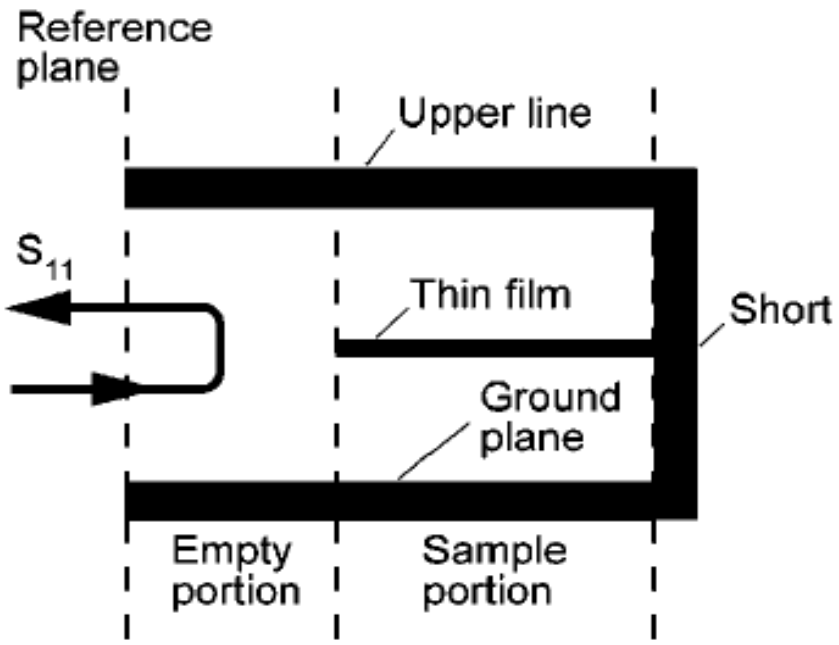

Figure 1.1 Schematic diagram[20] showing the cross section of a shorted microstrip fixture used in the transmission line perturbation method

The fixture consists of a brass casing acting as ground for the microstrip line with air as its substrate. (Figure 1.1) The magnetic film with substrate to be characterised is placed in

the air gap between the line and ground, which changes the effective propagation constant of the microstrip transmission line. This changes the reflection coefficient measured by a network analyzer, from which the permeability of the film can be extracted via circuit analysis after contribution from the substrate is eliminated. The essential steps to obtain the frequency dependent complex permeability of the film are as follows.

1. The microstrip fixture is first calibrated using the standard one-port short-load-open-through (SLOT) calibration for a preset measurement frequency range. Following, the reflection coefficient $S_{11}^{emp}(f)$ of the empty fixture at the port is measured, from which the effective permittivity of the transmission line shown in Figure 1.1 can be determined as

$$\varepsilon_{eff}^{emp}(f) = \left(\frac{ic \ln\left[-S_{11}^{emp}(f)\right]}{4\pi f (l_{emp} + l_{sample})} \right)^2, \qquad (1.1)$$

where f is the measurement frequency, c is the speed of light in vacuum, l_{emp} and l_{sample} are the length of the empty and sample region respectively. i is $\sqrt{-1}$.

2. The sample film on a substrate is then placed between the air gap and a static magnetic field is applied parallel to the microwave magnetic field (in-plane and perpendicular to the long-axis of the microstrip such that the film magnetisation is saturated parallel to the microwave magnetic field and therefore does not affect the effective permeability of the line. This sample can then be treated as consisting only of the substrate only, and the reflection coefficient of the transmission line loaded with substrate $S_{11}^{sub}(f)$ is

measured, from which the corresponding effective permittivity can be calculated as

$$\varepsilon_{eff}{}^{sub}(f)=\left(\frac{ic\ln\left[-S_{11}{}^{sub}(f)\right]}{4\pi fl_{sample}}-\frac{l_{emp}\sqrt{\varepsilon_{eff}{}^{emp}(f)}}{l_{sample}}\right)^2. \qquad (1.2)$$

3. The above static magnetic field is then removed and the reflection coefficient of the line loaded with flim and substrate $S_{11}^{film}(f)$ is measured, from which the corresponding effective permeability of the line loaded with film and substrate can be obtained as

$$\mu_{eff}(f)=\left(\frac{ic\ln\left[-S_{11}{}^{film}(f)\right]}{4\pi fl_{sample}\sqrt{\varepsilon_{eff}{}^{sub}(f)}}-\frac{l_{emp}\sqrt{\varepsilon_{eff}{}^{emp}(f)}}{l_{sample}\sqrt{\varepsilon_{eff}{}^{sub}(f)}}\right)^2. \qquad (1.3)$$

4. Once $\mu_{eff}(f)$ is found, the permeability of the film can be calculated as

$$\mu_{film}(f)=\frac{K}{t}\left(\mu_{eff}(f)-1\right), \qquad (1.4)$$

where *K* is a constant of the microstrip line obtained from calibration with a known sample and *t* is the film thickness.

1.2 Spin rectification effect

In addition to pick-up coil and transmission line perturbation methods, a recent phenomenon first discovered in 1960 by Juretschke[25] and subsequently demonstrated with a coplanar waveguide[21] in 2007 allows for very sensitive electrical detection of FMR in thin

films. This phenomenon, called the spin rectification effect (SRE), essentially converts microwave into a dc current via second order ac current-to-magnetoresistance coupling near FMR. In a ferromagnetic metal with conductivity σ and saturation magnetisation M_s subjected to an electric field $\vec{E}$ and magnetic field $\vec{H}$, the current density $\vec{J}$ within can be described by the generalized Ohm's Law

$$\vec{J} = \sigma\vec{E} - \frac{\sigma\Delta\rho}{M_s^2}\left(\vec{J}\bullet\vec{M}\right)\vec{M} + \sigma R_{HE}\left(\vec{J}\times\vec{H}\right) + \sigma R_{AHE}\left(\vec{J}\times\vec{M}\right). \qquad (1.5)$$

Here, R_{AHE} is the anomalous Hall coefficient, R_{HE} is the ordinary Hall coefficient and $\Delta\rho$ is the change of resistivity due to anisotropic magneto-resistance (AMR). $\vec{M}$ is the instantaneous magnetisation. In the presence of a microwave of angular frequency ω and absence of a dc electric bias, $\vec{J}$, $\vec{E}$, $\vec{H}$ and $\vec{M}$ are all time-dependent quantities: $\vec{J}(t) = \vec{J}_0 + \vec{j}(t)$, $\vec{E}(t) = \vec{e}(t)$, $\vec{H}(t) = \vec{H}_0 + \vec{h}(t)$, $\vec{M}(t) = \vec{M}_0 + \vec{m}(t)$, where $\vec{j}(t)$ is the microwave current, $\vec{e}(t)$ is the microwave electric field, $\vec{h}(t)$ is the microwave magnetic field and $\vec{m}(t)$ is the dynamic magnetisation. Since only even order product coupling between two time-dependent quantities can result in a dc current, we may keep only second order time-dependent terms in equation (1.5), leading to a dc current density

$$\vec{j}_{DC}^{\,SRE} = -\frac{\sigma\Delta\rho}{M_s^2}\left[\left\langle\vec{j}\times\vec{m}\right\rangle\times\vec{M} + \left\langle\vec{j}\cdot\vec{m}\right\rangle\vec{M}\right] + \sigma R_{HE}\left\langle\vec{j}\times\vec{h}\right\rangle + \sigma R_{AHE}\left\langle\vec{j}\times\vec{m}\right\rangle, \qquad (1.6)$$

where $\langle ... \rangle$ denotes a time-average over a period $2\pi/\omega$. Equation (1.6) tells us quantitatively that by virtue of the coupling between a microwave current $\vec{j}$ and the oscillating magneto-resistance (AMR and/or anomalous Hall effect (AHE)), the latter being

due to the precessional motion of spins induced by the microwave field $\vec{h}$, a dc current can result. It is important to note that the dc current due to SRE is only observable in thin films below the thickness of microwave skin depth δ_s since microwave fields decay exponentially as thickness increases, which results in regions with zero microwave fields shunting the SRE current, drastically decreasing the generated microwave voltage. The resulting dc current $\vec{j}_{DC}^{\,SRE}$ is sensitive to both FMR (due to its dependence on $\vec{m}(t)$) as well as the magneto-transport properties of the material, specifically AMR and AHE, and therefore can be an effective way to simultaneously measure its dynamic magnetic and magneto-transport properties. Furthermore, SRE is a phase-sensitive phenomenon, since the product coupling of two time-dependent quantities is strongly dependent on their relative phases. As a simple illustration, the coupling of two sinusoidal quantities phase-shifted by ζ leads to $\cos(\omega t)\cos(\omega t+\zeta) = \frac{1}{2}\left[\cos(2\omega t+\zeta)+\cos(\zeta)\right]$, where the first term time-averages to zero while the second dc term is clearly phase-dependent.

In recent years, SRE has been used as a very sensitive tool to electrically detect FMR, spin waves[26] and domain wall resonances[27]. Its phase sensitive nature also allows the fundamental phase relation between spin dynamics and microwaves to be directly probed, as demonstrated in an interferometry experiment[28]. Nonlinear effects due to FMR[29,30] and microwave-assisted magnetisation reversal (MAMR)[31] can also be sensitively studied via SRE, while its sensitivity to field configurations even allows it to be used as a rf field detector[32]. However, SRE can be undesirable in certain situations, particularly in the field of spintronics involving the electrical detection of spin phenomena such as dc spin pumping, spin Hall effect (SHE) and spin transfer torque (STT), in which SRE may mix with the signals of interest. This requires a good understanding of SRE in order to extract the signal of

interest, often via geometry considerations since SRE is highly dependent on field configurations, and can be particularly cumbersome to achieve. The issue of separating SRE and spin Hall voltages will be discussed and investigated thoroughly later on in this thesis.

1.3 Comparison of the accuracy and sensitivity of transmission line perturbation and electrical methods

In terms of accuracy and sensitivity, the electrical method for magnetic film characterisation is expected to be significantly better than the transmission line perturbation method. This is mainly because the latter is much more susceptible to noise: any slight disturbance along the transmission line (ie. nearby objects placed a few centimetres away) can produce capacitative, inductive and resistive noise that can signifcantly affect the measured S-parameters. Furthermore, as described in section 1.1, the transmission line perturbation method involves a lot more steps (due to the need to eliminate spurious signals from substrates) to extract the signal of interest (i.e permeability) therefore has more room for errors, compared to just one measurement step to measure the voltage in the electrical method from which the magnetic information can be directly extracted. The electrical method has no such issues on outside noise elimination since the current is totally confined within the sample, and is also compatible with lock-in measurement techniques that can further reduce noise and enhance sensitivity. However, one obvious drawback of the electrical method is that it cannot characterize non-conducting samples.

1.4 Ferromagnetic resonance and dynamics in thin films

Throughout this thesis, the dynamic magnetic properties of various magnetic thin film structures are studied via the above two methods. It is therefore important to first understand the theory governing magnetisation dynamics in films. In this section, we present the theory of FMR for ferromagnetic thin films modelled via the Landau–Lifshitz–Gilbert (LLG) equation, from which the dynamic susceptibility can be obtained. For a sample with magnetisation $\vec{M}$ subjected to an effective field $\vec{H}$ (which may include anisotropy and demagnetizing fields etc), the evolution of $\vec{M}$ with time *t* is given by the following LLG equation

$$\frac{d\vec{M}}{dt} = -\gamma \vec{M} \times \vec{H} + \frac{\alpha}{M_s} \vec{M} \times \frac{d\vec{M}}{dt}, \qquad (1.7)$$

where γ is the gyromagnetic constant and α is the Gilbert damping constant describing the longitudinal relaxation that brings $\vec{M}$ towards equilibrium. M_s is the saturation magnetisation. This relaxation mechanism represents the decay of spin precession due to energy dissipation to the lattice via spin-orbit coupling. For a thin film sample lying in the $\hat{x} - \hat{z}$ plane, with an effective static field $\vec{H}_0 = H_0 \hat{z}$ along $+\hat{z}$ and dynamic microwave excitation field $\vec{h} = h_x e^{i\omega t}\hat{x} + (h_y e^{i\omega t} - 4\pi m_y)\hat{y} + h_z e^{i\omega t}\hat{z}$ so that the total effective field $\vec{H} = \vec{H}_0 + \vec{h}$, equation (1.7) can be linearized as (assuming the dynamic components of $\vec{M}$ follow a time-dependence of $e^{i\omega t}$),

$$\frac{1}{\omega_m}\begin{pmatrix} \omega_x + i\alpha\omega & -i\omega & 0 \\ i\omega & \omega_y + i\alpha\omega & 0 \\ 0 & 0 & 0 \end{pmatrix}\begin{pmatrix} m_x \\ m_y \\ m_z \end{pmatrix} = \begin{pmatrix} h_x \\ h_y \\ h_z \end{pmatrix}, \qquad (1.8)$$

where $\omega_m = \gamma M_s$, $\omega_x = \gamma H_0$ and $\omega_y = \gamma(H_0 + 4\pi M_s)$. Note that in deriving (1.8), only terms first order in the dynamic quantities *h* and *m* are kept. Since equation (1.8) is of the form $\chi^{-1}\vec{m} = \vec{h}$, the dynamic susceptibility χ can be obtained directly by matrix inversion as

$$\begin{aligned} \chi &= \frac{\omega_m}{(\omega_x + i\alpha\omega)(\omega_y + i\alpha\omega) - \omega^2} \begin{pmatrix} \omega_y + i\alpha\omega & i\omega & 0 \\ -i\omega & \omega_x + i\alpha\omega & 0 \\ 0 & 0 & 0 \end{pmatrix} \\ &= \begin{pmatrix} \chi_{xx} & i\chi_{xy} & 0 \\ -i\chi_{xy} & \chi_{yy} & 0 \\ 0 & 0 & 0 \end{pmatrix}. \end{aligned} \tag{1.9}$$

The FMR condition can be obtained directly from (1.9) if one set the denominator to zero so that χ diverges, which leads to (for $\alpha \ll 1$) the FMR frequency $\omega_0 = \sqrt{\omega_x \omega_y}$ that is exactly the famous Kittel's equation[33]. In order to obtain the H_0 field-dependent susceptibility spectra in a simple form, we shall make the following substitutions and approximations:

1. $4\pi M_s \gg H_0$. This approximation is valid since the external field H_0 applied within our experimental settings is at least two orders of magnitude smaller than the saturation magnetisation $4\pi M_s$ of the ferromagnetic films studied.
2. $\alpha \ll 1$. Clearly valid since typical intrinsic damping constants for metallic ferromagnetic films are of the order of 0.01.
3. The following substitutions define the FMR field H_r and linewidth ΔH, and the applied external field (which may include any anisotropy fields) H_0:

$$\begin{aligned} \omega_0 &= \gamma\sqrt{H_r(H_r+4\pi M_s)} \\ \omega &= \gamma\sqrt{H_0(H_0+4\pi M_s)} \\ \gamma\Delta H &= 2\alpha\omega \end{aligned} \qquad (1.10)$$

From the above, after much straightforward simplification, the dynamic susceptibility χ in equation (1.9) can be written as

$$\chi = \begin{pmatrix} A_{xx} & iA_{xy} & 0 \\ -iA_{xy} & A_{yy} & 0 \\ 0 & 0 & 0 \end{pmatrix} \left| D + iL \right| e^{i\phi}, \qquad (1.11)$$

with $A_{xx} = \gamma 4\pi M_s / \alpha\omega$, $A_{xy} = 1/\alpha$ and $A_{yy} = \gamma H / \alpha\omega$.

$D = 2\Delta H\left(H_0 - H_r\right) / \left[4\left(H_0 - H_r\right)^2 + \Delta H^2\right]$ and $L = \Delta H^2 / \left[4\left(H_0 - H_r\right)^2 + \Delta H^2\right]$ are, respectively, the asymmetric (dispersive) and symmetric (Lorentzian) lineshapes with $\phi = \tan^{-1}(L/D)$ being the FMR phase difference between the dynamic magnetic field $\vec{h}$ and magnetisation $\vec{m}$. Equation (1.11) therefore completely describes the linear response of the dynamic magnetisation under an excitation microwave magnetic field, with parameters H_r, ΔH and $4\pi M_s$ which fully encompass the dynamic magnetic properties of the film.

1.5 Objectives and outline of the thesis

In this thesis, we studied a variety of magnetic thin film systems using transmission line perturbation method and electrical detection of FMR to demonstrate their viability in characterising the various systems. The characterisation method chosen for each of the magnetic systems presented depends largely on its suitability and the sensitiveness of the sample to the measurement method. However, the bulk of this thesis focuses on the electrical

method for FMR detection using a variety of measurement fixtures developed in our lab, mainly due to its higher sensitivity and compatibility with spin electronics. The outline of this thesis and its specific objectives are as follows.

In Chapter 2, we first studied a series of NiFe films via transmission line perturbation method to investigate the influence of stripe domains to their magnetic properties, with the objective of elucidating the behaviour of the rotatable anisotropy field associated with stripe domains as well as their damping characteristics.

Once the transmission line perturbation technique is made clear, we detail in Chapter 3 the electrical technique detect and quantify, via SRE, both the dynamic magnetic and magneto-transport properties of obliquely-sputtered FeAlSi films simultaneously. We characterise the oblique angular dependence of the various magnetic properties of the films.

Due to the compatibility of the electrical method with spin current phenomena, we also, in Chapter 4, develop and demonstrate a systematic method to separate the spin Hall effect from SRE in NiFe/Pt films to accurately determine the spin Hall angle of Pt. This addresses the issue of separating SRE from spin-current related signals of interest in spintronics systems.

In Chapter 5, we shall extend the electrical method of FMR measurement further by designing a coaxial probe that allows for the localized electrical excitation and detection of spin dynamics. The feasibility of this localized technique is demonstrated by performing measurements on a YIG substrate patterned with NiFe and Pt films to detect and characterise the YIG spin wave modes.

Finally, Chapter 6 further extends the capability of the electrical technique by demonstrating, using the coaxial probe, the detection and quantification of dipolar fields

originating from YIG spin waves in a bulk YIG substrate. The detection mechanism is based on SRE within a NiFe layer deposited on the YIG which is mediated by the dipolar fields due to excited YIG spin waves.

1.6 References

[1] J. K. Howard, Journal of Vacuum Science & Technology A: Vacuum, Surfaces, and Films **4,** 1 (1986).

[2] S. X. Wang, N. X. Sun, M. Yamaguchi, and S. Yabukami, Nature **407,** 150 (2000).

[3] C. A. F. Vaz, J. A. C. Bland, and G. Lauhoff, Reports on Progress in Physics **71,** 056501 (2008).

[4] D. O. Smith, M. S. Cohen, and G. P. Weiss, Journal of Applied Physics **31,** 1755 (1960).

[5] R. J. Prosen, J. O. Holmen, and B. E. Gran, Journal of Applied Physics **32,** S91 (1961).

[6] T. J. Silva, C. S. Lee, T. M. Crawford, and C. T. Rogers, Journal of Applied Physics **85,** 7849 (1999).

[7] C. T. Yu, H. Jiang, L. Shen, P. J. Flanders, and G. J. Mankey, Journal of Applied Physics **87,** 6322 (2000).

[8] B. K. Kuanr, R. E. Camley, and Z. Celinski, Journal of Magnetism and Magnetic Materials **286,** 276 (2005).

[9] N. X. Sun and S. X. Wang, Journal of Applied Physics **92,** 1477 (2002).

[10] F. Xu, N. N. Phuoc, X. Zhang, Y. Ma, X. Chen, and C. K. Ong, Journal of Applied Physics **104,** 093903 (2008).

[11] F. Xu, X. Chen, N. N. Phuoc, X. Y. Zhang, Y. G. Ma, and C. K. Ong, Journal of Magnetism and Magnetic Materials **322,** 3262 (2010).

[12] N. N. Phuoc, G. Chai, and C. K. Ong, Journal of Applied Physics **112,** 083925 (2012).

[13] S. M. Rezende, M. A. Lucena, A. Azevedo, F. M. de Aguiar, J. R. Fermin, and S. S. P. Parkin, Journal of Applied Physics **93,** 7717 (2003).

[14] C. Bilzer, T. Devolder, J.-V. Kim, G. Counil, C. Chappert, S. Cardoso, and P. P. Freitas, Journal of Applied Physics **100,** 053903 (2006).

[15] Y. Tserkovnyak, A. Brataas, and G. Bauer, Physical Review B **66,** 224403 (2002).

[16] Y. Tserkovnyak, A. Brataas, and G. E. Bauer, Physical Review Letters **88,** 117601 (2002).

[17] K. Uchida, S. Takahashi, K. Harii, J. Ieda, W. Koshibae, K. Ando, S. Maekawa, and E. Saitoh, Nature **455,** 778 (2008).

[18] J. E. Hirsch, Physical Review Letters **83,** 1834 (1999).

[19] M. Yamaguchi, O. Acher, Y. Miyazawa, K. I. Arai, and M. Ledieu, Journal of Magnetism and Magnetic Materials **242–245, Part 2,** 970 (2002).

[20] Y. Liu, L. Chen, C. Y. Tan, H. J. Liu, and C. K. Ong, Review of Scientific Instruments **76,** 063911 (2005).

[21] Y. Gui, N. Mecking, X. Zhou, G. Williams, and C. M. Hu, Physical Review Letters **98,** 107602 (2007).

[22] T. McGuire and R. Potter, IEEE Transactions on Magnetics **11,** 1018 (1975).

[23] N. Nagaosa, J. Sinova, S. Onoda, A. H. MacDonald, and N. P. Ong, Reviews of Modern Physics **82,** 1539 (2010).

[24] V. Bekker, K. Seemann, and H. Leiste, Journal of Magnetism and Magnetic Materials **270,** 327 (2004).

[25] H. J. Juretschke, Journal of Applied Physics **31,** 1401 (1960).

[26] Y. Gui, N. Mecking, and C. Hu, Physical Review Letters **98,** 217603 (2007).

[27] S. Sangiao and M. Viret, Physical Review B **89,** 104412 (2014).

[28] A. Wirthmann, X. Fan, Y. S. Gui, K. Martens, G. Williams, J. Dietrich, G. E. Bridges, and C. M. Hu, Physical Review Letters **105,** 017202 (2010).

[29] Y. S. Gui, A. Wirthmann, and C. M. Hu, Physical Review B **80,** 184422 (2009).

[30] Y. Gui, A. Wirthmann, N. Mecking, and C. M. Hu, Physical Review B **80,** 060402(R) (2009).

[31] X. Fan, Y. S. Gui, A. Wirthmann, G. Williams, D. Xue, and C.-M. Hu, Applied Physics Letters **95,** 062511 (2009).

[32] L. H. Bai, Y. S. Gui, A. Wirthmann, E. Recksiedler, N. Mecking, C. M. Hu, Z. H. Chen, and S. C. Shen, Applied Physics Letters **92,** 032504 (2008).

[33] C. Kittel, Physical Review **71,** 270 (1947).

2 Magnetisation dynamics in NiFe films with stripe domains

2.1 Introduction

The static and high frequency properties of soft magnetic films such as NiFe and FeCo also exhibit a dependence on film thickness, with applications ranging from Micro-Electro Mechanical Systems (MEMS)[1] for thick films (up to few microns) to high density data storage[2] for thin films (tens of nanometres). For most applications, excellent soft magnetic properties such as high saturation magnetisation and permeability are usually desired.

One cumbersome issue limiting the applicability of soft magnetic films stems from the formation of stripe domains[3] in thicker films, which can drastically affect its soft magnetic properties as well as introducing unwanted losses via magnetic hysteresis and increased damping from eddy losses. Since its discovery in the 1960s[3-5], magnetic stripe domain formation in films such as NiFe and FeCo alloys have been extensively studied to elucidate its character, focusing mainly on its static magnetic properties[3-8] due to its relevance to most applications such as magnetic recording and data storage. More recently, the focus of research in stripe domain films have shifted towards the understanding of its dynamic magnetic properties[8-12] in the microwave regime. One key finding of such dynamic studies is that the ferromagnetic resonance (FMR) frequency is sharply up-shifted in the presence of stripe domains, which is attributed to an anisotropy field that is isotropic and rotatable with the stripe direction. While the appearance of the rotatable anisotropy and stripe domains is known to be correlated, a clear qualitative relationship between these stripe domain structures and the rotatable anisotropy field values is still lacking. Furthermore, as the magnitude of this stripe domain-induced anisotropy can be significantly larger than any uniaxial anisotropy

present, a better understanding of their relationship will also allow for the potential control of this rotatable anisotropy for tunable microwave applications.

Till now, interesting dynamic phenomena associated with stripe domain structures are still being discovered and explored. In particular, the multiple-peak behaviour in the FMR spectra of stripe domain NiFe films have recently[10] been characterised and interpreted in terms of localised domain modes depending on the rf pumping field orientation. The presence of multiple excitation modes clearly illustrates the highly unsaturated nature of such films, which could have significant extrinsic contributions to magnetic damping that have yet been well-characterised.

The above yet unaddressed issues provides the main motivation for this work, where we have conducted a comparative study on NiFe films of various thicknesses to investigate the dynamic response of the magnetic films to the in-plane static magnetisation process. We find that the rotatable anisotropy field is not a fixed value but varies strongly with the in-plane static applied field which is quantitatively related to the formation of stripe domains. Also, the frequency linewidth spectra for films with stripe domains show three distinct regimes as the static magnetic field is swept, being correlated to the static magnetisation process and the interplay between the dynamic anisotropy field and static applied field.

2.2 Theoretical Background

In a magnetic thin film, the magnetisation lie predominantly in-plane and a large out-of-plane magnetic field of the order of the saturation magnetisation is usually required to tilt the magnetisation completely out of plane. This is due to the strong out-of-plane demagnetizing field which arises due to the field continuity boundary condition that states

that the magnetic field must be continuous across a boundary. As a simple illustration (Figure 2.1), suppose that the magnetisation in a thin film with permeability μ and saturation magnetisation $4\pi M_s$ were to lie out of plane, then the internal field in the out-of-plane direction would be $B = 4\pi M_s$. If no external field is applied, $B = 0$ outside the film. Therefore, a B field discontinuity would have occurred at the boundary of the film, violating $\nabla \cdot B = 0$. This means that an internal demagnetizing field H_d must be present that exactly cancels the field produced by M_s, so that the internal field $B = 4\pi M_s - H_d = 0$ can be matched to the external field at the boundary.

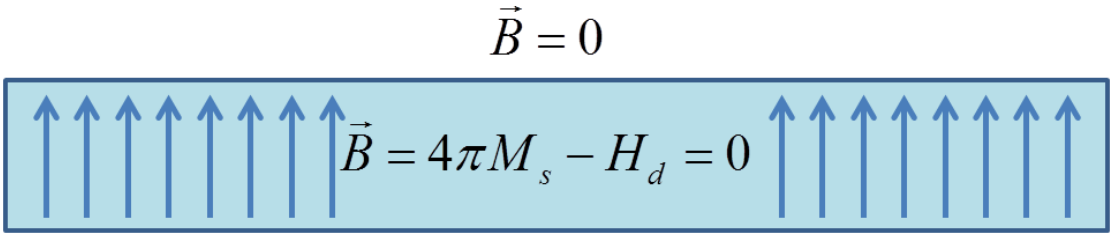

Figure 2.1 Cross section view of the magnetic field $\vec{B}$ within and outside of a film whose magnetisation lies out-of-plane.

Thus, in order to align the magnetisation out of plane, a large out-of-plane field $H > H_d = 4\pi M_s$ must be applied to counter this demagnetizing field, which can be up to 1kG for Permalloy (NiFe) or 1.8kG for FeCo so that under normal conditions, the magnetisation of a thin film always lies in plane.

In view of the large demagnetizing field which arises in a thin film geometry that tend to align the magnetisation in-plane, the presence of strong perpendicular (out-of-plane) anisotropy K_p, whose origin can be magneto-crystalline and/or stress anisotropy[10,13], can often effectively negate the out-of-plane demagnetizing field, such that the magnetisation

may have a significant out-of-plane component even in the absence of any external field. This often leads to the formation of peculiar domain structures characterised by periodic stripes aligned along the anisotropy/external field or even maze-like patterns for large perpendicular anisotropy. These stripe domains, which can be directly imaged using a Magnetic Force Microscope (MFM), represents a periodic arrangement of alternating in-plane and out-of-plane magnetisations. The extent of the stripe domain structures can be characterised by the quality factor[4] $Q = K_p / 2\pi M_s^2$, being the ratio of perpendicular anisotropy to shape anisotropy. The shape anisotropy is the result of the demagnetizing field that tend to counter the perpendicular anisotropy. If $Q \geq 1$, the magnetisation lies predominantly out-of-plane to form maze-like stripe structures. For intermediate values of Q, stripe domains structures are only energetically favourable above a certain critical film thickness t_c.

2.3 Experimental details

We fabricated a series of NiFe films with thicknesses (t_{NiFe}) ranging from 35 nm to 525 nm on Si (100) substrates, via rf magnetron sputtering at room temperature. The base chamber pressure is about 7×10^{-7} Torr, with Ar pressure kept at 2×10^{-3} Torr during deposition. A capping layer of SiO_2 (~10 nm) is then deposited on top of each NiFe film to protect against oxidation. A magnetic field of ~200 Oe is also applied to induce a small uniaxial anisotropy in the films. The thickness of each layer is controlled by the deposition time and rate, and verified by a thickness profile meter with a resolution of ~1 nm. After deposition, a Vibrating Sample Magnetometer (VSM) is used to measure the hysteresis loops of the samples at room temperature. The static magnetic topology of the samples is also measured using a Magnetic Force Microscope (MFM). The high frequency permeability

spectra of the films are also measured by a homemade microstrip fixture via a Vector Network Analyser (VNA), from which the dynamic hysteretic behaviour of the FMR frequency and linewidth is characterised.

2.4 Results and Discussion

2.4.1 Determining the critical thickness for stripe domains in NiFe films

In this section, the critical thickness for the appearance of stripe domains in our NiFe films is determined based on measurement results and analysis. We first present the hysteresis loops of a few representative NiFe films with various thicknesses in Figure 2.2. From Figure 2.2, we see that for t_{NiFe}=35, 100 nm, the hysteresis loops are typical of films with uniaxial anisotropy in which square loops and slanted loops are obtained along the easy and hard axes respectively. For films thicker than 170 nm (t_{NiFe}=170, 230 nm in Figure 2.2), the loops for both easy and hard axes become indistinguishable with each other, acquiring a distinct shape characterised by a marked decrease in magnetisation from saturation value as the field decreases and a non-zero remanence. Such hysteresis loops are unique[8] to films with stripe domains. When the in-plane applied field is large, all domains are saturated and the magnetisation points in the field direction and reaches saturation. As the field decreases below a certain value H_s, stripe domains starts to form, with the stripes being aligned in the field direction. Within each stripe, a significant number of spins are canted out-of-plane such that the in-plane magnetisation is reduced so that even when the field reaches zero, the stripe domains still retain some in-plane magnetisation. (Figure 2.2c inset) The superposing of the easy and hard axes loops suggests that such stripe domains formation is isotropic. The

coercivity is also seen to be much larger for flims with stripe domains for t_{NiFe}=170, 230 nm, usually implying that the anisotropy has increased.

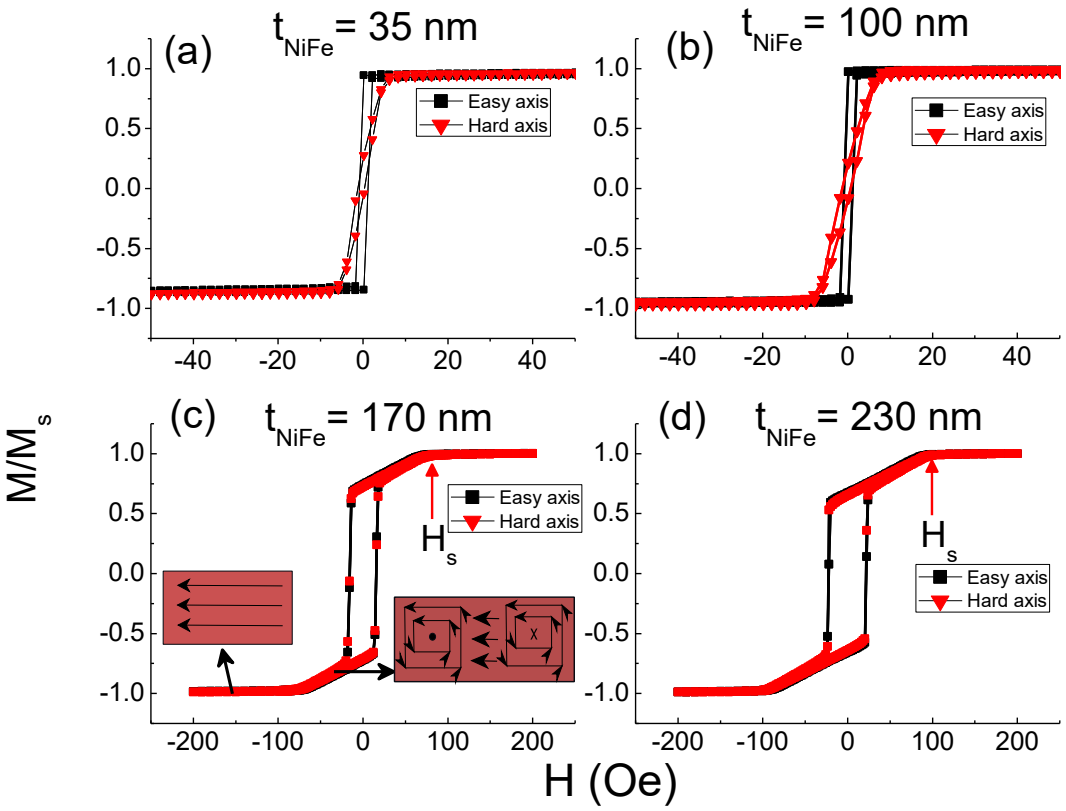

Figure 2.2 Normalised M-H hysteresis curves as measured by VSM for (a) t_{NiFe}=35 nm, (b) t_{NiFe}=100 nm, (c) t_{NiFe}=170 nm and (d) t_{NiFe}=230 nm. Inset (c): The proposed magnetic domain structures within the film at the corresponding magnetisation states.

As noted in M-H measurements, t_{NiFe}=170nm is the thickness above which stripe domains start to appear. This is also well-supported by atomic force microscopy and magnetic force microscopy results, as weak stripe domains can be seen in the corresponding MFM image presented in Figure 2.3 (b) below. As the film thickness increases, the stripe domain structures widen and become more pronounced, as seen in Figure 2.3 (d) for t_{NiFe}=340nm. For films with thicknesses below 170nm, MFM measurements reveal no domain structures. The measured root-mean-square roughness for all films is less than 1 nm,

indicating that the films are smooth and of good quality. Our smaller-area scans also reveal no significant difference between the grain sizes of films with no stripe domains (100 nm) and those with stripe domains (>170 nm), thus the difference in magnetic properties are not likely to be due to grain sizes and their distribution.

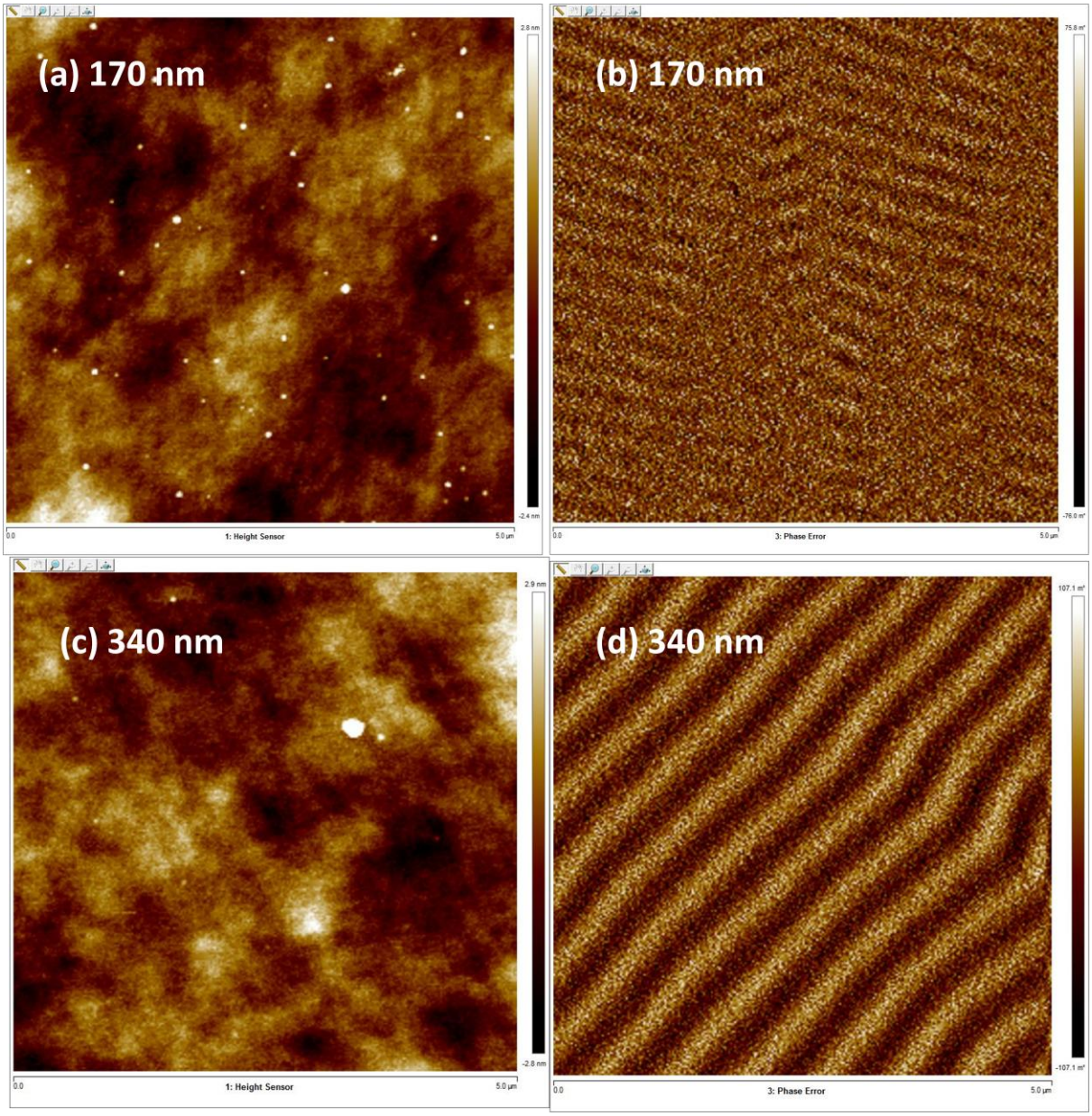

Figure 2.3 Atomic force microscopy image of the physical topology of a 5μm by 5μm area of the (a) 170nm thick NiFe film and (c) 340 nm thick NiFe film and their corresponding magnetic force microscopy image of the same area (b) and (d) respectively.

Subsequently, once the static magnetic properties of the films have been characterised, we turn to its dynamic properties as determined from our permeability measurements. The imaginary part of the permeability for t_{NiFe}=100nm is shown in Figure 2.4 under various applied static magnetic fields, from which the FMR frequency f_{fmr} and

linewidth Df can be determined from a lorentzian fit to its peak position and width respectively. The FMR frequency and linewidth generally increases with applied field in accordance with theory, as can be seen from Figure 2.4. Comparing across film thicknesses, we observe that the zero-field f_{fmr} increases drastically from about 0.7 GHz to 1.5 GHz as t_{NiFe} increases above 170 nm. (Figure 2.5(a)) The coercivity is also seen to exhibit the same behaviour at t_{NiFe}=170 nm, increasing sharply from nearly zero to more than 10 Oe. (Figure 2.5(b)) These drastic changes in magnetic properties at t_{NiFe}=170nm points to a magnetic transition at 170nm due to the formation of stripe domains. Therefore, we conclude that t_{NiFe}=170±30nm is the critical thickness for the formation of stripe domains in our NiFe films.

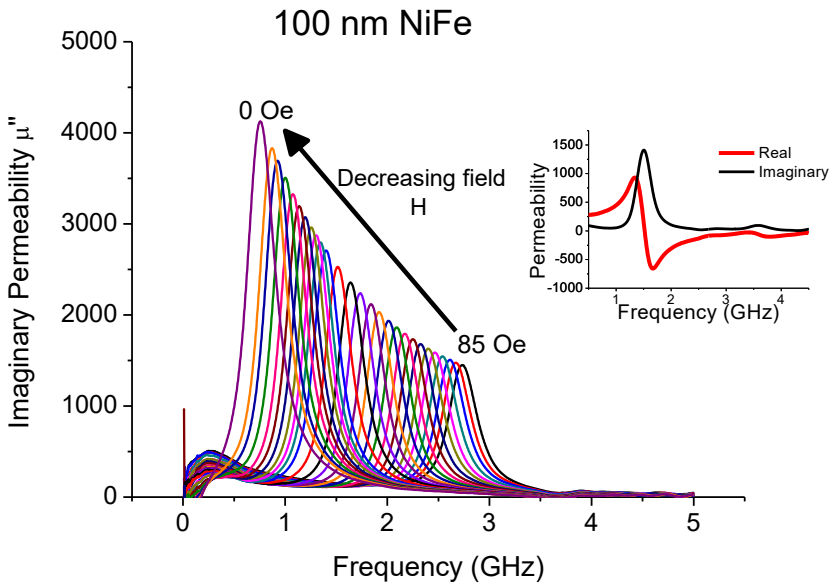

Figure 2.4 For t_{NiFe}=100nm, the imaginary part of the magnetic permeability as a function of frequency as measured using a shorted microstrip fixture, under various applied static magnetic fields from 85 to 0 Oe. Inset shows the real and imaginary parts of the permeability spectra for t_{NiFe}=170 nm under zero applied field.

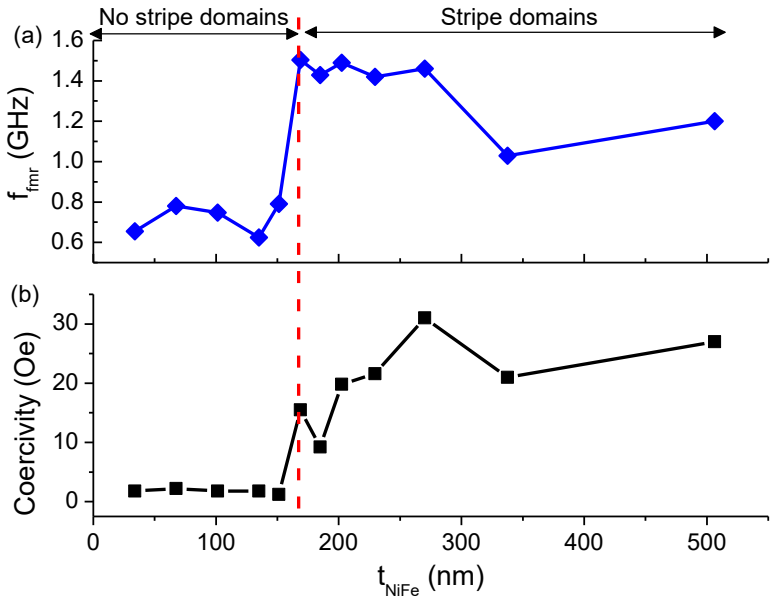

Figure 2.5 (a) FMR frequency under zero applied static magnetic field and (b) coercivity as a function of NiFe film thicknesses.

2.4.2 Characterisation of the rotatable anisotropy field

As noted in literature, the formation of stripe domains is often associated with the appearance of a peculiar form of anisotropy called the rotatable anisotropy. This rotatable anisotropy appears to only manifests[14,15] itself in dynamic measurements such as FMR, as static measurements such as M-H loops are unable to reveal its existence. This rotatable anisotropy is said to lead to the large increase in zero-field FMR frequency as well as the coercivity in films with stripe domains. It has been suggested[14] that a small transverse ac field can lead to this rotatable anisotropy, due to the dragging of spins by this ac field away from the stripe direction that increases the magnetic free pole energy in the volume. However, the experiments in Ref. [14] were done at much lower frequencies of ~10^3 Hz, thus, a quantitative analysis of this rotatable anisotropy field at much higher microwave frequencies in conjunction with the appearance of stripe domains is still lacking. In our experiment, the

external static field can be varied continuously and applied along various in-plane angular orientations within the film while the permeability is measured. This allows us to obtain a comparative study of the variations of the dynamic magnetic properties in response to the static magnetisation process in films with stripe domains.

From the permeability spectra obtained, we can determine the FMR frequency f_{fmr} as a function of applied field H for various in-plane angles θ, where θ is measured from the easy axis. This is described by the following Kittel's formula

$$f_{fmr} \cong \frac{\gamma}{2\pi}\sqrt{\left(H + H_k^{dyn}\right)\left(H + 4\pi M\right)} \qquad (2.1),$$

where H_k^{dyn} is the dynamic anisotropy field and M is the macroscopic magnetisation in the direction of H. In our experimental settings, $4\pi M \gg H$ since the magnetisation for all cases are saturated to ~10kG or nearly saturated even with stripe domains. Thus, equation (2.1) can also be approximated as

$$f_{fmr}^{\ 2} \cong \frac{\gamma^2}{4\pi^2} 4\pi M \left(H + H_k^{dyn}\right). \qquad (2.2)$$

Figure 2.6(a) shows a plot of $f_{fmr}^{\ 2}$ against H for two representative films with (t_{NiFe}=170nm) and without (t_{NiFe}=100nm) stripe domains. We see that the plots for both films only deviates when H decreases below the saturation field H_s for stripe domains in the t_{NiFe}=170nm film. To explain the difference in $f_{fmr}^{\ 2}$ behaviour between the two films, we make use of equation (2.2), noting that the magnetisation processes for each film are different. (Figure 2.2) For t_{NiFe}=100nm, M is nearly constant at ~10kG as H decreases to zero. For t_{NiFe}=170nm, M does not stay constant but starts to decrease from saturation as H decreases below H_s, reaching a finite remenance of about 70% of saturation value at H=0. Thus, M in equation (2.2) is

clearly not constant when stripe domains appear, which may account for the difference in behaviour between the two plots. We argue that equation (2.2) holds even when *M* becomes unsaturated, since in the macroscopic picture even when *M* cants out-of-plane, the direction of *M* perpendicular to the transverse microwave magnetic field still contributes to FMR. Then, a quick deduction using equation (2.2) shows that f_{fmr}^2 should decrease with decreasing *M*, contrary to what was observed for t_{NiFe}=170nm in Figure 2.2 where f_{fmr}^2 is observed to *increase* instead with decreasing *M* as *H* decreases below H_s. Thus, the decrease in *M* for t_{NiFe}=170nm is not a significant cause for the deviation between the two plots. We quantitatively prove this point by calculating, based on equation (2.1), f_{fmr}^2 for t_{NiFe}=170nm (Figure 2.6(a), dotted line) based on known values of *M* (taken from VSM results), *H*, and H_k^{dyn}, assuming that H_k^{dyn} is constant. Note that H_k^{dyn} can be fitted from the linear part of the f_{fmr}^2 against H plot, where *M* is saturated. Clearly, the calculated curve and experimental data do not fit when $H<H_s$ when stripe domains starts to form. This points us towards the role of H_k^{dyn} in stripe domains films, suggesting that its value does not stay constant throughout the demagnetisation process by the decreasing applied field *H*.

From equation (2.1) at each θ, with all known values of *M*, *H* and f_{fmr}^2, H_k^{dyn} is given by

$$H_k^{dyn} = \sqrt{\frac{4\pi^2 f_{fmr}^2}{\gamma^2} + 4\pi^2 M^2} - 4\pi M - H. \qquad (2.3)$$

We plot the variation of H_k^{dyn} with *H* as obtained using experimental data with equation (2.3) in Figure 2.6(b) for t_{NiFe}=170nm and t_{NiFe}=100nm. For t_{NiFe}=170nm, we can see that H_k^{dyn} is nearly linearly increasing with decreasing *H* for $H<H_s$ but stays almost constant for $H>H_s$. This interesting trend can be attributed to the presence of rotatable anisotropy

associated with stripe domains, which we can quantify by further performing an angular FMR measurement with H applied various angles θ. The measured angular dependence of H_k^{dyn} is shown in Figure 2.6(c) for various applied fields, where a clear sinusoidal behaviour is seen, with the plots also shifting isotropically upwards towards higher H_k^{dyn} as H decreases from 80 to 0 Oe. The sinusoidal behaviour stems from uniaxial anisotropy H_k^{sta}, while we attribute the isotropic shift to be due to rotatable anisotropy H_{rot}. Thus, we can quantify the anisotropies by fitting the plots to $H_k^{dyn} = H_{rot} + H_k^{sta} \cos 2\theta$, which is in good agreement with experimental data. Figure 2.6(d) shows H_{rot}, derived from such a fitting procedure, as a function of H. For films with stripe domains (t_{NiFe}=170, 230nm), it is evident that H_{rot} follows the same trend as H_k^{dyn} in Figure 2.6(c), being drastically increased as H decreases below H_s. This shows that H_{rot} varies strongly with H below H_s while the static uniaxial anisotropy H_k^{sta} stays constant. When $H>H_s$, H_{rot} is seen to saturate at around 9 and 13 Oe for t_{NiFe}=170nm and t_{NiFe}=230nm respectively.

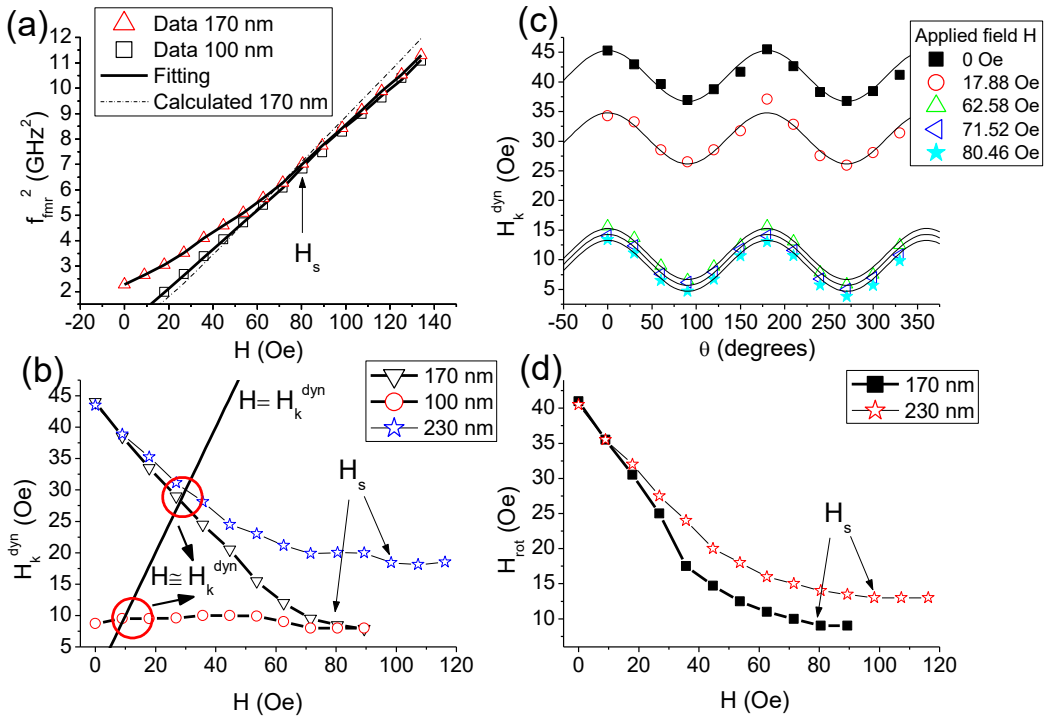

Figure 2.6(a) Plot of f_{fmr}^2 against H for two representative films with (170nm) and without (100nm) stripe domains. (b) Variation of H_k^{dyn} with H for t_{NiFe}=100, 170 and 230nm. (c) For t_{NiFe}=170nm, the angular dependence of H_k^{dyn} with θ for various H. (d) Dependence of H_{rot} with H for t_{NiFe}=170 and 230nm. Adapted with permission from Ref. [16].

From the analysis above, it is clear that H_{rot} is quantitatively associated with stripe domain films and can be suppressed by increasing the applied field above saturation. This points to a competition between the in-plane field H and the perpendicular anisotropy, such that when H is high enough to decouple the magnetisation from the influence of perpendicular anisotropy, the film becomes saturated and stripe domains disappears. As such, it should be expected that the saturation field H_s is proportional to the perpendicular anisotropy H_p which was consistent with that given by Murayama's model[4] as

$$H_s = H_p\left(1-\frac{t_c}{t_{NiFe}\sqrt{1+Q}}\right), \qquad (2.4)$$

where t_c is the critical thickness for the formation of stripe domains.

2.4.3 Damping behaviour of NiFe films with and without stripe domains

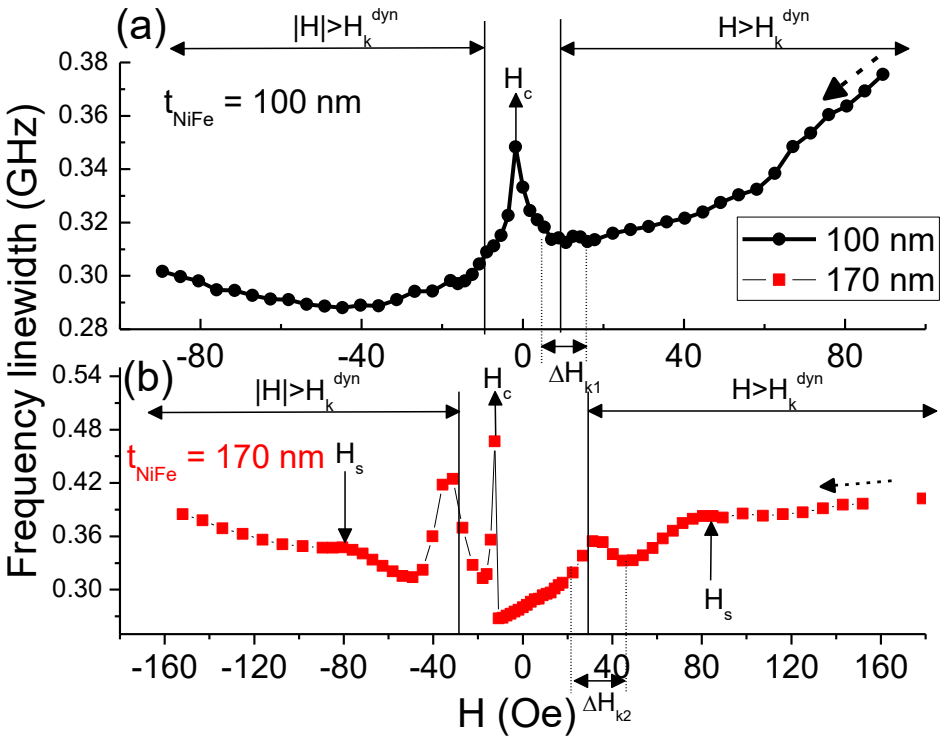

Figure 2.7(a) Δf as H decreases from positive to negative (opposite direction) for t_{NiFe}=100nm (with stripe domains) and t_{NiFe}=170nm (without stripe domains), where the transition regions can be clearly seen.

The field-dependent behaviour of Δf for a representative film without stripe domains (t_{NiFe}=100nm) and for a film with stripe domains (t_{NiFe}=170nm) shows categorically different behaviours. (Figure 2.7) For films without stripe domains Δf is seen to vary smoothly with H and increases sharply as H tends to zero. For films with stripe domains, Δf exhibit abrupt changes with H and reaches a minimum as H tends to zero. For both films, at the coercivity field H_c where the magnetisation flips, Δf shoots up to a maximum.

To explain these interesting behaviours, we first note that Δf can be expressed as

$$\Delta f = \frac{\partial f}{\partial H}\Delta H, \qquad (2.5)$$

with

$$\Delta H = \Delta H_0 + \frac{4\pi}{\gamma\sqrt{3}}\alpha f_{fmr}, \qquad (2.6)$$

where α and ΔH_0 are the Gilbert damping constant and inhomogeneous linewidth[17] respectively. The second term in (2.6) represents the intrinsic Gilbert damping which is linear in frequency f_{fmr}. The first term ΔH_0 consists of mainly (for this case) frequency-independent contribution due to local linewidth broadening as a result of an overlap of local precession linewidths of individual magnetic grains dispersed in magnetic anisotropy and magnetisation.

Thus, by comparing (2.1), (2.5) and (2.6), one can explain the observed behaviours of Δf . For t_{NiFe}=100nm, the gradient of f vs H plot ($\partial f/\partial H$) is clearly increased at low H~20 Oe (Figure 2.8(a)). From (2.5), since Δf is proportional to $\partial f/\partial H$, Δf thus increases accordingly at low H. (Figure 2.8(d)) Furthermore, an additional contribution to the increase in Δf here is likely due to the increase in ΔH_0 at lower field where the magnetic dispersion is more pronounced. By the magnetic ripple theory, the mean angular variation φ of the magnetisation along the easy axis varies[18-20] as $\left(1+H/H_k^{dyn}\right)^{-3/8}$. This means that φ starts to increase significantly whenever $H<H_k^{dyn}$, and this increased magnetisation dispersion further results in an increase in Δf . This is consistent with our observed results (Figure 2.7(a) and 2.8(d)), where Δf is seen to increase sharply just as H decreases below H_k^{dyn}. At higher H, Δf increases fairly linearly with H as expected due to the intrinsic Gilbert damping contribution.

To explain the behaviour of Δf for the film with stripe domains (t_{NiFe}=170nm), we first note that the plot of f_{fmr} against H exhibits linear behaviour with two distinct gradients $\partial f / \partial H$ in the regions when $H>H_s$ and $H<H_s$ (Figure 2.8(b)). We may fit the slopes in these two regions $H>H_s$ and $H<H_s$ to obtain the gradients as $k_1 \approx 1.21\times10^7$ Hz Oe^{-1} and $k_2 \approx 1.45\times10^7$ Hz Oe^{-1} respectively. Clearly, k_1 is smaller than k_2. We can then deduce from (2.5) based on the gradients k_1 and k_2 that the Δf variation with H would also show distinct gradients for these two regions of H, which is indeed consistent with that observed in Figure 2.8(e). The transition from saturated state to stripe domains at H_s is thus shown to be strongly manifested in both the f_{fmr} and Δf plots, which can be explained quite quantitatively using equations (2.1), (2.5) and (2.6). As discussed earlier, the stripe domain transition at H_s causes drastic changes in the magnitude of the in-plane magnetisation state M as well as inducing an additional rotatable anisotropy H_{rot}. The stripe domain transition therefore manifests in the f_{fmr} and Δf through changes in M and H_{rot}.

In addition to this transition at H_s, we also see that Δf abruptly increases as H decreases below 40 Oe, while maintaining the same gradient. We note that this transition at H~40 Oe is close to the value of H_k^{dyn} which we have found earlier from H_{rot} measurements, thus reinforcing the earlier point that the magnetisation dispersion is significantly increased when $H<H_k^{dyn}$ thus causing Δf to increase as well. However, since the Gilbert damping and $\partial f / \partial H$ stays constant, the gradient of Δf stays constant as well at this point. This Δf transition at $H \simeq H_k^{dyn}$ is much more abrupt than the corresponding one for t_{NiFe}=100nm where stripe domains are absent, thus stripe domains may have an interesting contribution to magnetisation dispersion at low fields which is yet unclear at this point. Lastly, the f_{fmr} and Δf spectra for another film with stripe domains (t_{NiFe}=230nm) are also presented in Figure

2.8(c), showing similar features whereby Δf shows distinct regions which are correlated with $\partial f / \partial H$ and H_k^{dyn}. In particular, we see that a change in $\partial f / \partial H$ at *H~95* Oe is marked by a corresponding change in the gradient of Δf versus *H* plot. An abrupt increase in Δf is also seen when $H \simeq H_k^{dyn}$.

As discussed in Youssef *et al*[21], the frequency linewidths Δf for all the films are observed to decrease drastically with increasing film thickness when stripe domains are formed. (i.e Δf decreases from 0.28 to 0.2GHz when t_{NiFe} increases from 170nm to 230nm at *H=0*) However, despite having different values at *H=0*, Δf increases to roughly the same value of 0.39GHz as $H \sim H_s$, which is consistent with the fact that once saturated, the magnetisation state of the films are similar and therefore their damping properties should be the same.

The above discussion thus far treats the magnetisation in the macroscopic picture whereby only the average magnetisation in a specific direction is considered, which is reasonable since only a single resonance mode is observed in the permeability spectra in our experimental setting. However, as also pointed out[21] , the appearance of multiple modes and their interactions in film with stripe domains may also contribute some of the above observations when $H < H_s$. Such multiple resonance modes are not observed in our analysed films, which is likely due to the fact that they are close to the critical thickness for stripe domains, thus such multiple mode analysis is not needed here.

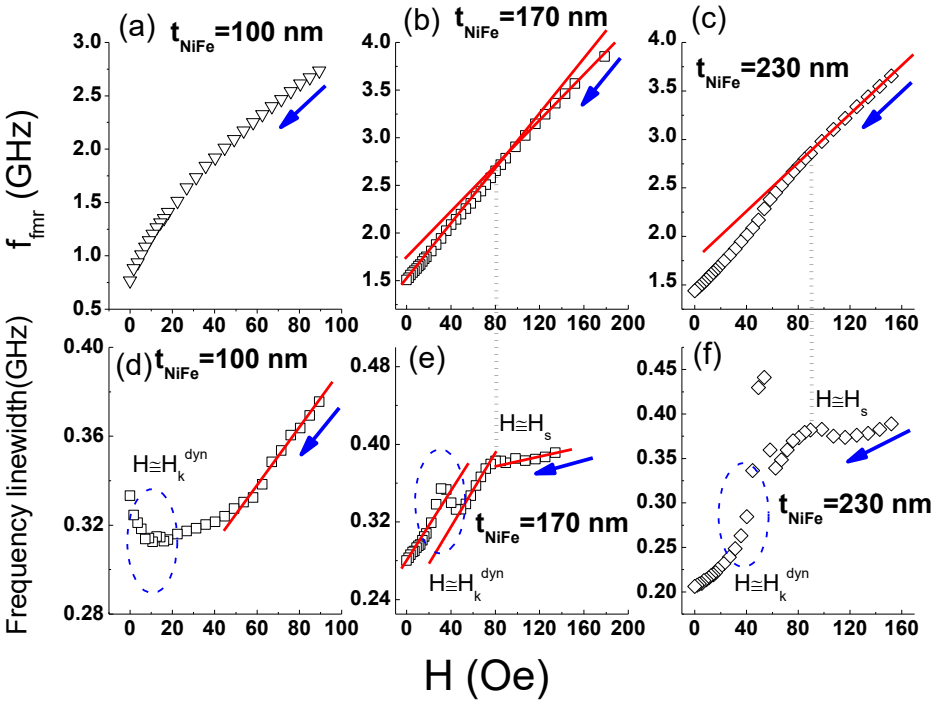

Figure 2.8 f_{fmr} and Δf as a function of H, on the same scale for comparison, for various films. Blue arrows represent the direction of change of H. Adapted with permission from Ref. [16].

2.5 Conclusion

In this chapter, we have measured, using a shorted microstrip transmission line perturbation method, the high frequency permeability spectra for a series of NiFe films with and without stripe domains, over a range of film thicknesses from 35-525nm. We have identified that the critical thickness for the formation of stripe domains in our films is 170nm, based on both static and dynamic measurements. From the results, we have demonstrated that the formation of stripe domains is associated with the appearance of a rotatable anisotropy field that varies in magnitude with the applied static magnetic field. This rotatable anisotropy field, which is attributed to the increase of magnetic free pole energy as a result of the dragging of spins away from the equibrium strip direction by the ac field, can be much larger than any induced uniaxial anisotropy and thus provides an alternative method to tune the

dynamic magnetic properties of films. In addition, the frequency linewidth for films with stripe domains show distinct regions as the static field is varied, being strongly correlated with the static magnetisation processes as well as the relative magnitude of the applied static field to the total dynamic anisotropy field.

2.6 References

[1] N. M. Dempsey, A. Walther, F. May, D. Givord, K. Khlopkov, and O. Gutfleisch, Applied Physics Letters **90,** 092509 (2007).

[2] C. Chappert, A. Fert, and F. N. Van Dau, Nat Mater **6,** 813 (2007).

[3] H. Fujiwara, Applied Physics Letters **8,** 262 (1966).

[4] Y. Murayama, Journal of the Physical Society of Japan **21,** 2253 (1966).

[5] Y. Sugita, Applied Physics Letters **10,** 229 (1967).

[6] M. Labrune and J. Miltat, Journal of Applied Physics **75,** 2156 (1994).

[7] N. Amos, R. Fernandez, R. Ikkawi, B. Lee, A. Lavrenov, A. Krichevsky, D. Litvinov, and S. Khizroev, Journal of Applied Physics **103,** 07E732 (2008).

[8] G. Wang, C. Dong, W. Wang, Z. Wang, G. Chai, C. Jiang, and D. Xue, Journal of Applied Physics **112,** 093907 (2012).

[9] O. Acher, C. Boscher, B. Brulé, G. Perrin, N. Vukadinovic, G. Suran, and H. Joisten, Journal of Applied Physics **81,** 4057 (1997).

[10] N. Vukadinovic, M. Labrune, J. Youssef, A. Marty, J. Toussaint, and H. Le Gall, Physical Review B **65,** 054403 (2001).

[11] C. A. Ramos, E. Vassallo Brigneti, J. Gómez, and A. Butera, Physica B: Condensed Matter **404,** 2784 (2009).

[12] Y. Talbi, P. Djemia, Y. Roussigné, J. BenYoussef, N. Vukadinovic, and M. Labrune, Journal of Physics: Conference Series **200,** 072107 (2010).

[13] P. Zou, W. Yu, and J.A. Bain, IEEE Trans. Magn. **38**, 3501 (2002).

[14] L. M. Alvarez-Prado, G. T. Perez, R. Morales, F. H. Salas, and J. M. Alameda, Phys Revs B **56**, 3306 (1997).

[15] G. Chai, N. N. Phuoc, and C. K. Ong, Sci Rep **2,** 832 (2012).

[16] W. Tee Soh, N. N. Phuoc, C. Y. Tan, and C. K. Ong, Journal of Applied Physics **114,** 053908 (2013).

[17] B. Kuanr, R. E. Camley, and Z. Celinski, Applied Physics Letters **87,** 012502 (2005).

[18] H. Hoffmann, Journal of Applied Physics **35,** 1790 (1964).

[19] D. Spenato, A. Fessant, J. Gieraltowski, H. Le Gall, and C. Tannous, Journal of Applied Physics **85,** 6010 (1999).

[20] R. J. Prosen, J. O. Holmen, and B. E. Gran, Journal of Applied Physics **32,** S91 (1961).

[21] J. Ben Youssef, N. Vukadinovic, D. Billet, and M. Labrune, Physical Review B **69,** 174402 (2004).

3 Dependence of dynamic magnetisation and magneto-transport properties of FeAlSi films with oblique sputtering studied via spin rectification effect

3.1 Introduction

Sendust, an alloy of Fe, Al and Si (denoted FeAlSi thereafter) typically in ratios of 85:6:9, which was invented in Sendai, Japan in the 1930s is widely used in bulk form as the active material in low frequency kHz devices such as power transformers and filter inductors due to its excellent magnetic properties[1-5], among which includes negligible magneto-crystalline anisotropy, high permeability and saturation magnetisation (~13 kG) as well as relatively large resistances compared to other metallic ferromagnets for lower eddy current losses. However, in the regime of higher GHz frequencies where thin films are more applicable, the dynamic magnetic properties of FeAlSi are not well-known. Rather, metallic ferromagnetic alloys such as NiFe (Permalloy) and FeCo, which also exhibits excellent soft magnetic properties, have thus far dominated research in this area, in which both their static and high frequency dynamic magnetic properties have been well-studied and characterised that enables their further use in high frequency tuneable applications.

In the field of spintronics, it is quite often favourable for the magnetic films to also possess large electrical (magnetic) response to magnetic (electrical) stimulus, notably the magneto-resistance and anomalous Hall effects (AHE). In addition, the generation of transverse spin currents via charge currents (i.e. spin Hall effect) in non-magnetic heavy metals, which is currently of high research interest owing to its relatively high efficiency as spin current sources, has its magnetic analogue in ferromagnetic films via the AHE. As such, ferromagnetic films with high AHE would be promising candidates as spin current

sources/detectors. Currently, NiFe, which possess much lower AHE than its AMR, has been widely studied[6-11] in inverse spin Hall effect (ISHE) experiments as spin current sources via spin pumping at ferromagnetic resonance, and thus its AHE and AMR are mostly seen as a hindrance due to their spurious mixing with the ISHE signal of interest, whose consequence is the subject of the following chapter. ISHE generates a transverse charge current due to a spin current, which is the reverse process of SHE.

Recent experiments[12,13] have begun investigating NiFe as spin current detectors, in which its AHE would now play a major role equivalent to SHE in non-magnetic metals (i.e Pt). It has been found that, despite having relatively low AHE, NiFe possess significant SHE comparable to Pt, thus allowing it to play a new role as efficient ferromagnetic spin current detectors. However, it is not yet known if FeAlSi films can exhibit significant AHE and/or SHE. On the other hand, single-crystal Fe_3Si has been found[14] to exhibit significantly higher spin pumping efficiency than NiFe, while the relatively high T_c magnetic semiconductor, Co-doped FeSi, can possess[15] very high AHE. As such, similar alloys like FeAlSi may also possess desirable spin transport properties which have yet been well-studied.

Over the past few years, some studies[5] have been done by our group on FeAiSi films based on the shorted microstrip transmission line perturbation method, whereby some of its dynamic magnetic properties such as FMR frequency, anisotropy and saturation magnetisation have been characterised. However due to limitations of the transmission line perturbation method, other high frequency properties such as damping (not sensitive enough) and magneto-transport (requires electrical measurement) are not characterised.

In this chapter, we present an experimental study of FeAlSi films via SRE (Section 1.2), in which the electrical detection of FMR allows for the simultaneous characterisation of the dynamic magnetic and magneto-transport properties. In addition, the dependence of

oblique deposition on the properties of FeAlSi films is also investigated via SRE. Oblique deposition[16-18] changes the structural alignment of magnetic grains and has been known to be able to induce anisotropy in both the magnetisation[19-23] and dc resistance[24] thus offering a method to tune these quantities for applications. Here, we show that oblique deposition can significantly influence AHE and AMR as well. The high frequency characteristics of these films are studied as well to illustrate their dependence on oblique deposition.

3.2 Experimental Procedures

A series of obliquely deposited (with oblique angles β ranging from 0-45°) 50 nm-thick FeAlSi films on $5\text{ mm} \times 10\text{ mm} \times 0.5\text{ mm}$ thick Si (100) substrates are prepared via room-temperature rf magnetron sputtering at base pressure of 7×10^{-7} Torr, with Ar sputtering pressure of 5.5×10^{-3} Torr. (Figure 3.1)The target is 3-inch diameter FeAlSi alloy. (by weight, 85 % Fe, 6 % Al and 9% Si) Before sputtering of FeAlSi, 2 mm-wide Cu contacts are first sputtered and patterned at opposite edges of Si substrates as sites for electrical contacts. The sputtered area of FeAlSi films is thus $5\text{ mm} \times 6\text{ mm}$. A magnetic field of around 200 Oe is applied during sputtering to induce uniaxial anisotropy and a capping layer of SiO_2 (~10 nm) is deposited to prevent oxidation. The axis of uniaxial anisotropy is fixed along $\phi_H = 90°$.

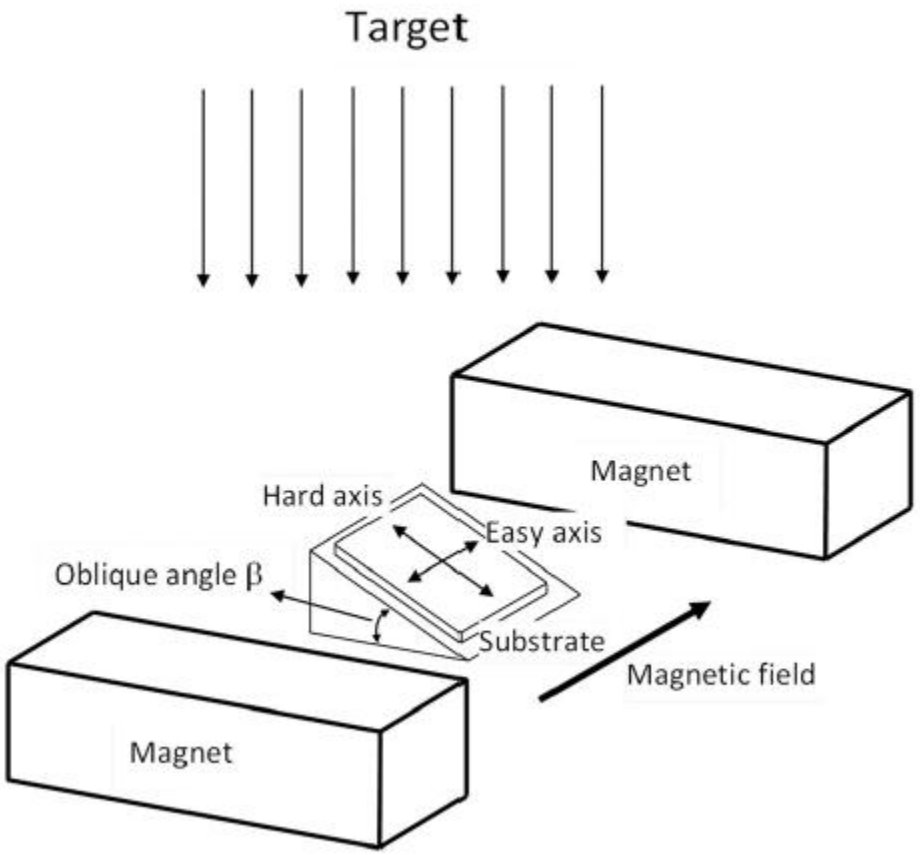

Figure 3.1 Schematic diagram of the setup during oblique deposition of the films.

The samples are measured via SRE based on our homemade shorted microstrip fixture, where dc voltages are measured sensitively by a lock-in amplifier at kHz modulation under an applied microwave at 18 dBm power. At fixed microwave frequency, we measure the dc voltages as a function of an in-plane applied field H (dc voltage spectra). We then repeat the measurement for various microwave frequencies. Furthermore, we measure the dc voltage spectra for various in-plane H angles under a fixed microwave frequency.

3.3 Calculating the SRE DC voltages based on the measurement setup

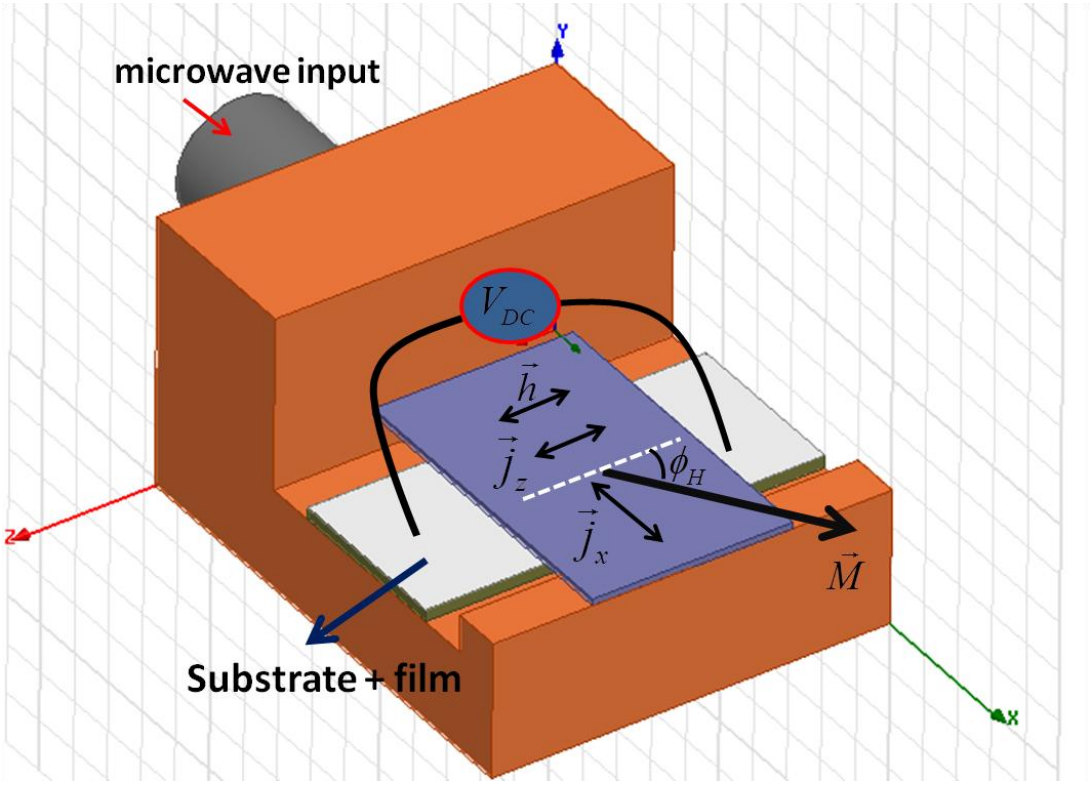

Figure 3.2 Schematic diagram of the SRE measurement configuration in our shorted microstrip fixture. A cross-section in the *x*-y plane is given in Figure 1.1. Adapted with permission from Ref. [25].

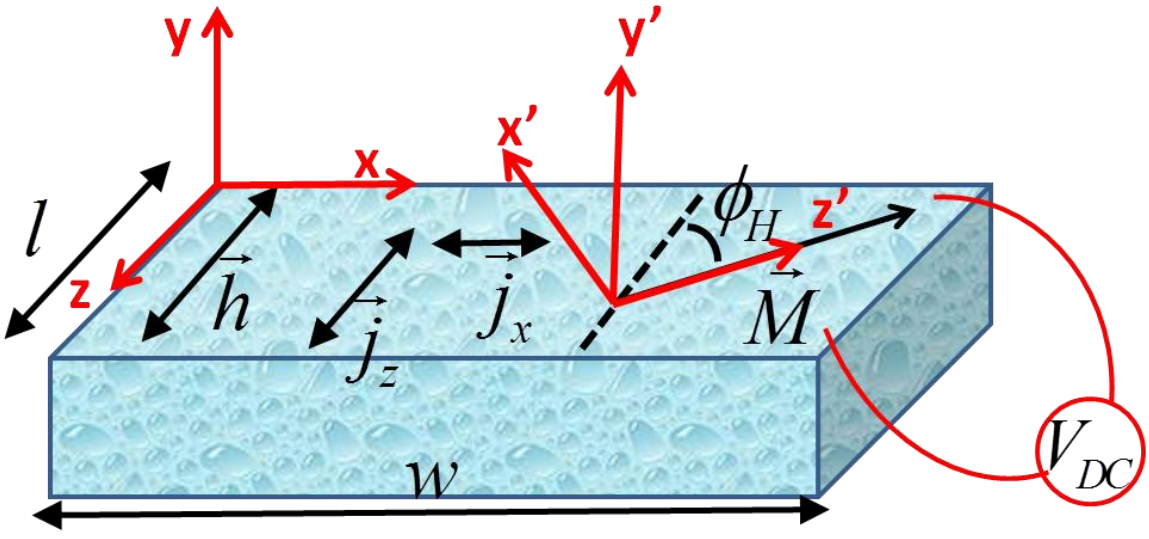

Figure 3.3 Not drawn to relative scale, the field configurations within the film. The static lab co-ordinates (*x*, *y*, *z*) are fixed in the dc measurement direction while the rotating co-ordinates (*x'*, *y'*, *z'*) rotates with $\vec{M}$.

The dc measurement configuration for our samples within the shorted microstrip fixture is shown in Figure 3.2. Under excitation by a microwave field $\vec{h}$, an oscillating magnetisation $\vec{m}(t)$ is induced which couples to the microwave current $\vec{j}$ via AMR and AHE, producing a non-zero dc current density by SRE as described by equation (1.6). To find the in-plane angular ϕ_H dependence of the SRE voltage, we first need to find the ϕ_H dependence of the dynamic magnetisation $\vec{m}$. Thus, we define two sets of co-ordinates (Figure 3.3): the lab co-ordinates (*x*, *y*, *z*) fixed with the V_{DC} measurement direction and the co-ordinates (*x'*, *y'*, *z'*) that rotates with $\vec{M}$ which is assumed to be saturated along $\vec{H}$. The co-ordinates are thus related by a rotation matrix $R_y(\phi_H)$ along the *y*-axis. Thus, the dynamic magnetisation $\vec{m}$ in the lab frame is simply

$$\vec{m}_{x,y,z} = R_y(\phi_H)\,\chi_{x',y',z'} R_y(-\phi_H)\,\vec{h}_{x,y,z}, \qquad (3.1)$$

where $\chi_{x',y',z'}$ is the susceptibility matrix in the rotating $\vec{M}$ frame previously derived in section 1.3 of chapter 1. Once $\vec{m}$ is known and with $\vec{j} = (j_x, 0, j_z)^T$, it is straightforward to plug in these quantities and calculate from equation (1.6) that the resultant measured SRE dc voltage V_{DC} is

$$V_{DC} = A_L L + A_D D, \qquad (3.2)$$

where

$$\begin{aligned} A_L &= -\sin\Phi\left[V_{AMR}{}^{x}\sin\phi_H\cos 2\phi_H - V_{AMR}{}^{z}\sin\phi_H\sin 2\phi_H\right] - V_{AHE}\cos\Phi\sin\phi_H, \\ A_D &= \cos\Phi\left[V_{AMR}{}^{x}\sin\phi_H\cos 2\phi_H - V_{AMR}{}^{z}\sin\phi_H\sin 2\phi_H\right] - V_{AHE}\sin\Phi\sin\phi_H. \end{aligned}$$

Here, $V_{AMR}{}^{x(z)} = A_{xx} h j_{x(z)} l \Delta\rho / (8\pi M_s)$ and $V_{AHE} = A_{xy} R_{AHE} j_x h l / 2$ refers to the AMR and AHE contributions respectively, with $\Delta\rho$ being the change in resistivity due to AMR and R_{AHE} the AHE coefficient. $l = 6$ mm is the FeAiSi sample length along V_{DC}. *L* and *D* are the Lorentzian and dispersive lineshapes as a function of applied field *H*, respectively. From a fit of the voltage against field spectra at various angles ϕ_H (at various microwave frequencies) to equation (3.2), one obtains the angular (frequency) dependence of resonance field H_r, field linewidth ΔH, Lorentzian amplitude A_L and dispersive amplitude A_D. Notably, j_x and j_z produces AMR voltages with orthogonal angular dependences and therefore can be separated from each other, as well as from V_{AHE} via an angular measurement and fitting.

3.4 Finite-element method to simulate the field configurations of microstrip fixture

Oblique angle (deg)	σ_{zz} ($\times 10^5$ Ω^{-1}m^{-1})	σ_{xx} ($\times 10^5$ Ω^{-1}m^{-1})	$\lvert\vec{j}_x\rvert$ ($\times 10^7$ Am^{-2})
0	6.48	6.48	1.65
17	6.48	6.09	1.63
27	6.07	5.70	1.55
39	6.48	5.32	1.57
42	5.85	4.93	1.47
45	6.40	4.54	1.49

Table 3.1. Simulation parameters based on measured conductivities σ_{xx} and σ_{zz}, and simulated microwave current magnitude $\lvert\vec{j}_x\rvert$ at the centre of the film.

Thus far, we have seen from equation (3.2) that the SRE voltage V_{DC} depends critically on the relative orientations of the microwave magnetic field *h* and current *j* generated by the fixture on the film. To elucidate the magnitude and directions of the current density and field distributions within our films, finite-element simulations[26] are performed using Ansoft HFSS to model the coupling between our microstrip fixture and FeAlSi films. The measured conductivities σ_{zz} are used as parameters in our simulations. Because σ_{xx} is not measureable due to the presence of a capping SiO_2 layer, a gradual decrease of 36% in σ_{xx} is assumed from 0 to 45 deg oblique samples resulting from the possible anisotropy in resistivity due to oblique sputtering. The simulation parameters for various films are given in Table 3.1. Contributions to the first order due to the anomalous Hall Effect and anisotropic magneto-resistance can be neglected in our simulations, since these effects are only considered to the second order in our measured dc voltages. Figure 3.4 shows the current density distribution for 0 deg oblique FeAlSi (50 nm) film at 2.9 GHz and 18 dBm power, as seen from the top view.

From Figure 3.4, it is seen that the current density is strongest below the microstrip, where our FeAlSi film resides. In this region, the current density dominantly flows in *x* direction, since the *z* components cancel due to symmetry. Therefore, only j_x is significant, which is consistent with results from our angular measurements and fitting that we will see later. Comparing the simulated current density j_x (at the centre of the film) across all oblique samples, we see that despite a 36% decrease in σ_{xx} postulated due to oblique deposition, j_x remains relatively unchanged with only a ~5% variation. Thus, our assumption of $j_x \sim 1\times10^7$ Am^{-2} is justified. Figure 3.5 shows the simulated microwave magnetic field $\vec{h}$ distribution within the sample. Clearly, the dominant contribution of $\vec{h}$ lies in the *z*-direction,

with magnitudes which are consistent with our experimental determination via FMR experiments performed with a Vector Network Analyzer. This is also consistent with the fact that *j* lies dominantly in the *x* direction, for a quasi-TEM mode propagation in the microstrip line.

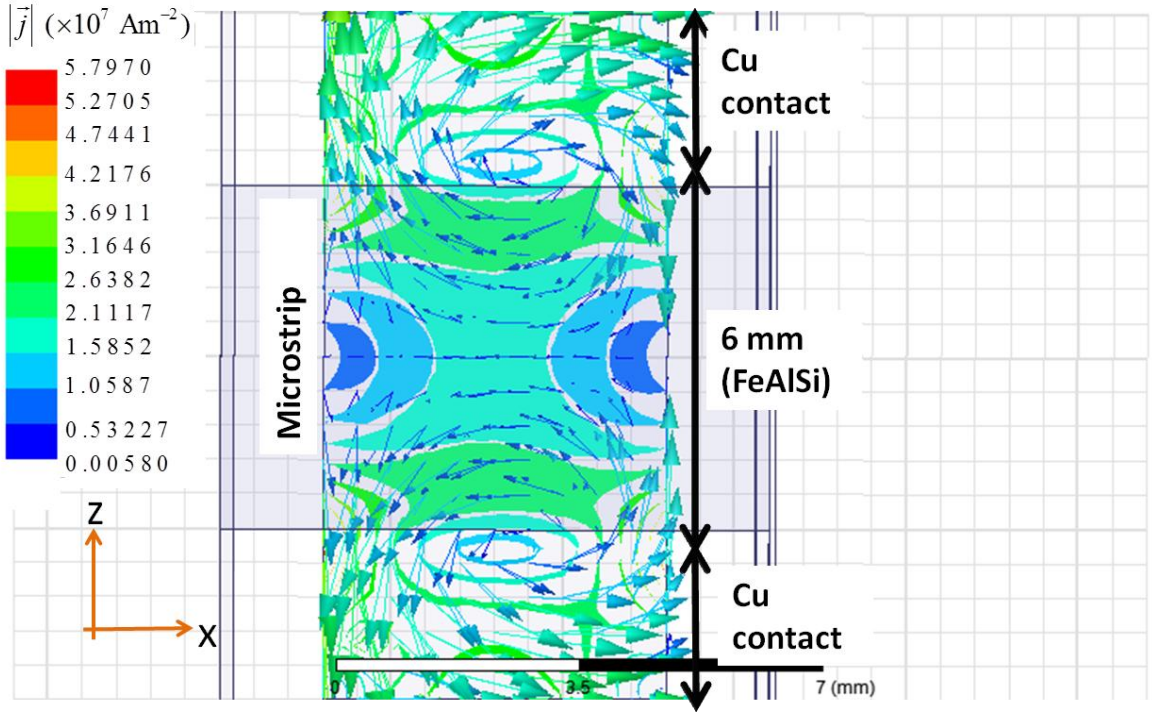

Figure 3.4 Direction (arrows) and magnitude (colour scale) of the current density distributions for the 0 deg oblique FeAlSi film, as seen from top view.

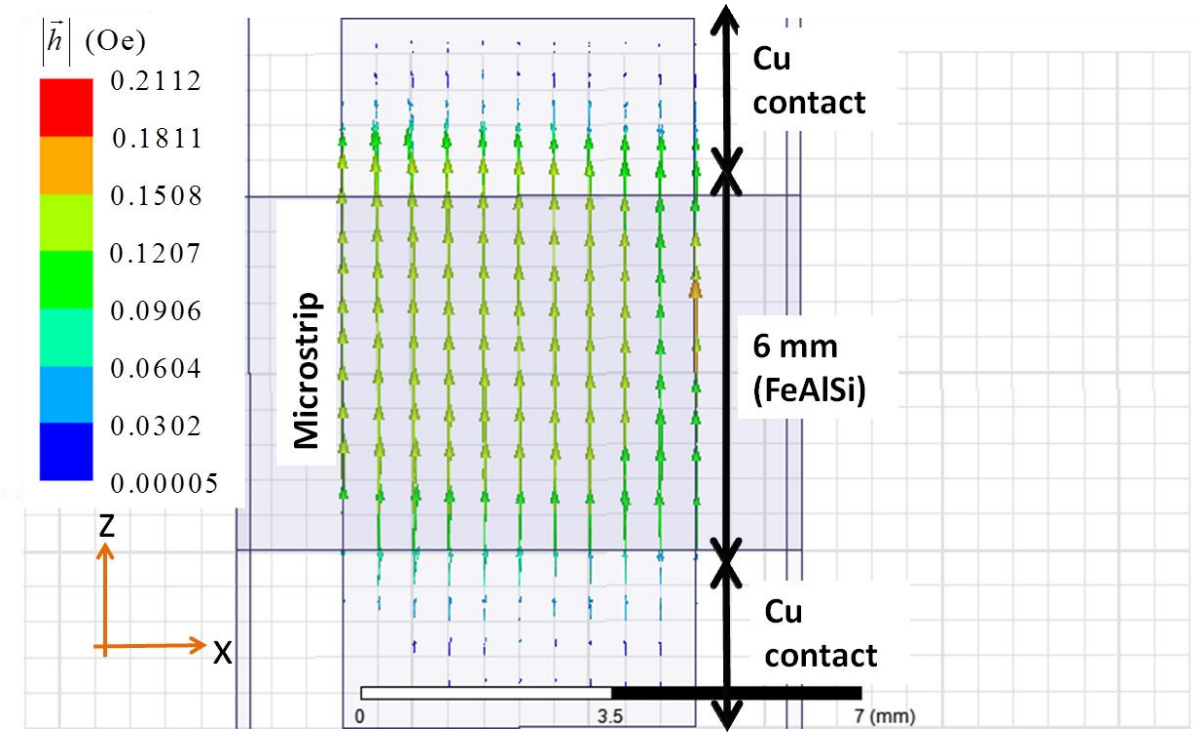

Figure 3.5 Direction (arrows) and magnitude (colour scale) of the microwave magnetic field distributions for 0 deg oblique FeAlSi film, as seen from top view.

3.5 Results and discussion

3.5.1 Dynamic magnetic properties of FeAlSi films

The measured raw V_{DC} spectra for FeAlSi films deposited at various oblique angles is presented in Figure 3.6 below, with microwave frequency fixed at 2.9 GHz and H along the uniaxial axis (easy axis) at $\phi_H = 90°$. We observe that the FMR resonance field, represented by the peak consisting of a superposition of L and D lineshapes, shifts progressively towards lower H as the oblique angle increases from 0° to 45°. This behaviour, as we shall quantify in a moment, is indicative of an increase in anisotropy with increasing oblique angle. Furthermore, the magnitude of V_{DC} at resonance is also clearly decreasing with increasing

oblique angle. We find, as will be discussed in the subsequent section, that this trend is the result of a dependence of AMR and AHE on oblique incidence.

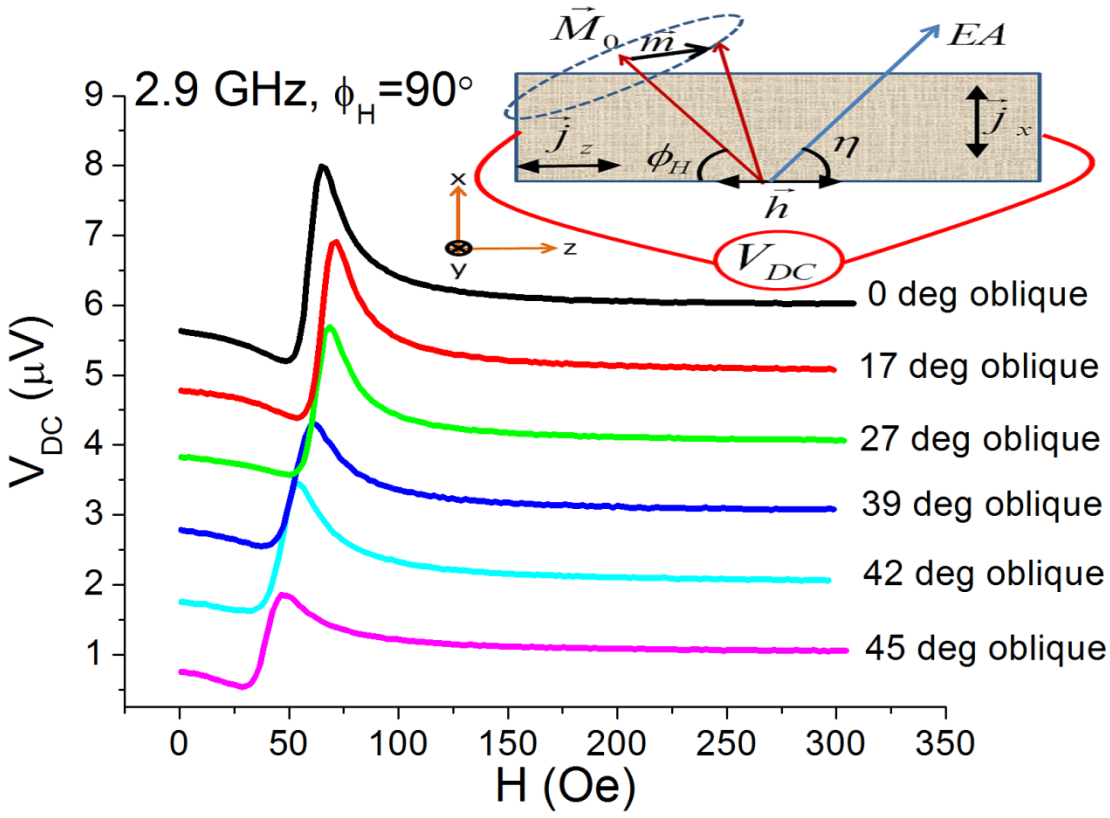

Figure 3.6 V_{DC} as a function of H applied along $\phi_H = 90°$ at 2.9 GHz, for various oblique angles. Plots have been offset for clarity. Inset shows the relative orientations of the field and measurement configurations. Adapted with permission from Ref. [26].

We are interested to characterise the dependence of the various magnetic anisotropies with oblique angles. The angular dependence of FMR field H_r, calculated using Smit and Beljers[27] formalism by minimising the Zeeman and various anisotropies, is given by

$$H_r = \sqrt{\left(\frac{\omega}{\gamma}\right)^2 - ab + \left(\frac{a+b}{2}\right)^2} - \frac{a+b}{2}, \qquad (3.3)$$

where $a = H_a \cos(2\phi_H - 2\eta) + H_{rot}$ and $b = 4\pi M_s - H_a \sin^2(\phi_H - \eta) + H_{rot}$, with H_a and H_{rot} respectively being the uniaxial and rotatable anisotropy. The rotatable anisotropy here, in contrast to the one discussed in the preceding chapter, stems from FM grains whose uniaxial axis rotate with H direction analogous to that in exchange-biased[28] systems. From equation (3.3), we see that the uniaxial anisotropy H_a gives a dominant two-fold symmetric $\cos(2\phi_H)$ contribution while H_{rot} is isotropic with respect to the in-plane orientation of H.

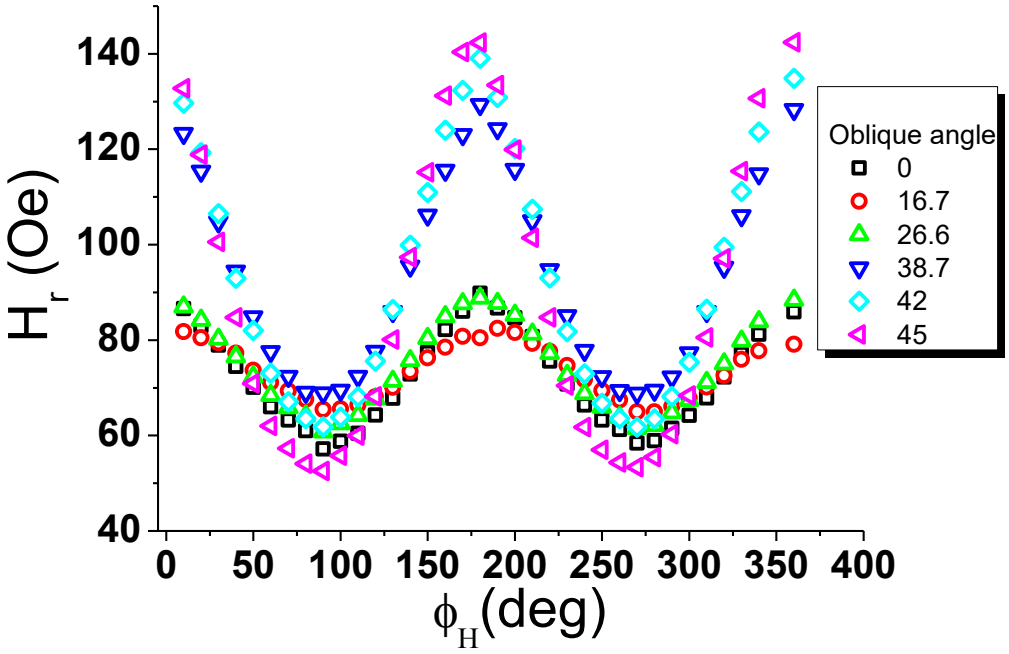

Figure 3.7 FMR field H_r, obtained from V_{DC} spectra at 2.9 GHz, against in-plane H angle ϕ_H for films with various oblique angles.

The FMR field H_r, linewidth ΔH, coefficients A_L and A_D are first obtained by fitting the V_{DC} spectra to equation (3.2). All measurements here are done with microwave frequency fixed at 2.9 GHz so that we may compare samples with different oblique angles on an equal footing. The angular ϕ_H dependence of H_r for various samples is plotted in Figure 3.7, where

it is clear that uniaxial anisotropy dominates due to the two-fold symmetry exhibited by the plots. Moreover, it is also apparent that significant rotatable anisotropy is present within the films due to the isotropic vertical shift of the plots across samples of different oblique angles.

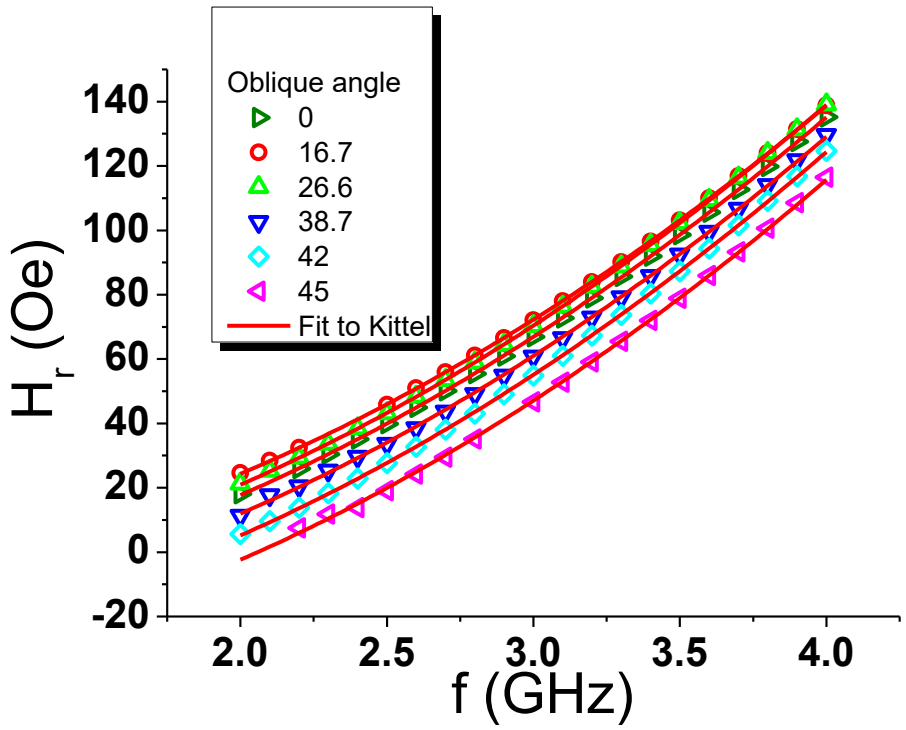

Figure 3.8 Frequency f variation of the FMR field H_r for various obliquely sputtered FeAlSi films and their fits to theory.

Before extracting the anisotropy fields from the plots in Figure 3.7, we first conduct a frequency sweep to obtain the V_{DC} spectra for a range of frequencies so that the variation of H_r with microwave frequency f can be determined, shown in Figure 3.8. Next, we fit them to equation (3.3) to obtain the saturation magnetisation M_s~13 kG. Thereafter, using this value of M_s and with $\gamma = 1.76 \times 10^7$ rad s^{-1} Oe^{-1}, the anisotropy fields are extracted by fitting the plots in Figure 3.7 to equation (3.3) and summarised in Figure 3.9. From Figure 3.9, we see

that the uniaxial anisotropy H_a appears to stay relatively constant between 10-15 Oe with increasing oblique angle until around 30° whereby it increases drastically to 40 Oe with increasing oblique angle. This increase in H_a can be explained by noting that oblique deposition at higher angles of incidence leads to the formation of magnetic grains elongated[17,19,23] in the direction normal to the oblique incidence, which for our experiments, had been chosen to be aligned along the uniaxial anisotropy induced by a magnetic field during deposition. This grain elongation (columnar tilt) leads to magnetic shape anisotropy along the same direction, and the sum of this shape anisotropy due to all the elongated grains contribute to an overall increase in uniaxial anisotropy. The rotatable anisotropy H_{rot} is seen to remain relatively unchanged compared to H_a with oblique incidence. However, a slight decrease in H_{rot} with increasing oblique angle can be seen, which may be attributed to a decrease in magnetic anisotropy dispersion as H_a increase due to stronger alignment of grains.

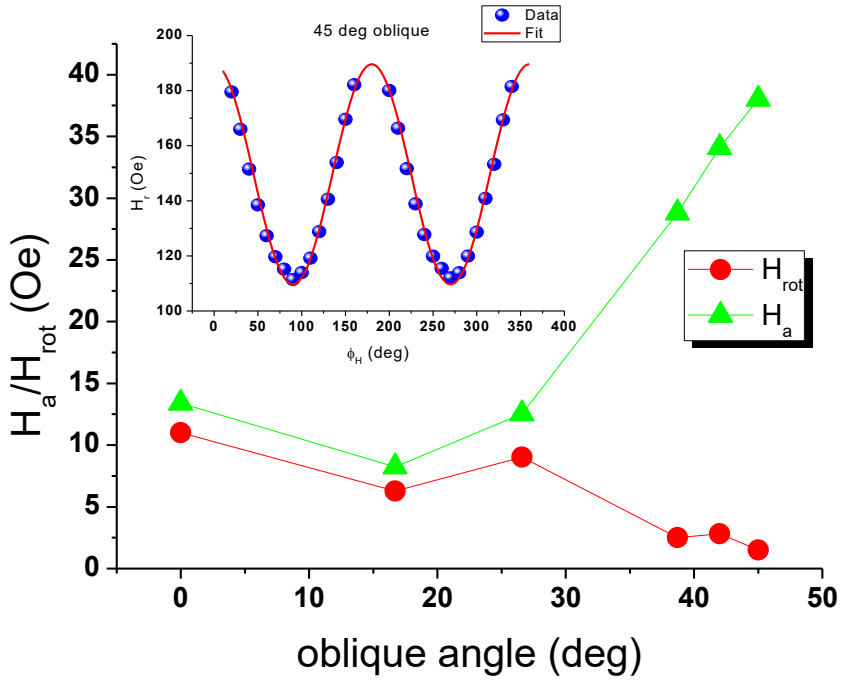

Figure 3.9 Dependence of the uniaxial anisotropy H_a and rotatable anisotropy H_{rot} with oblique angle. Inset shows the angular dependence of H_r for 45° oblique incidence with the corresponding fit (solid line) to theory. Adapted with permission from Ref. [26].

Next, we discuss the damping characteristics of these obliquely sputtered FeAlSi films. Along with H_r as discussed above, the angular dependence of the field linewidth ΔH had been obtained from fits to the V_{DC} spectra. Here, the field linewidth can be written as

$$\Delta H = \Delta H_{\text{int}} + \Delta H_{mos} + \Delta H_{2M}. \qquad (3.4)$$

The intrinsic Gilbert contribution is given by $\Delta H_{\text{int}} = 2\alpha\omega/\gamma$ which is linear in microwave frequency. $\Delta H_{mos} = \left|\partial H_r/\partial\left(4\pi M_s\right)\right|\Delta\left(4\pi M_s\right) + \left|\partial H_r/\partial\eta\right|\Delta\eta$ denotes the mosaicity[29] contribution which describes linewidth broadening due to dispersion in magnetisation $\Delta\left(4\pi M_s\right)$ and uniaxial anisotropy axis $\Delta\eta$. This effect typically dominates for films with

significant perpendicular anisotropy as the resulting in-plane magnetisation dispersion would be enhanced due dragging of magnetisation by the perpendicular anisotropy.

Another contribution to damping which is significant here is the two-magnon damping. It has been discussed by Arias and Mills[30] that in magnetic thin films, the spin wave dispersion relation supports the degenerate scattering from the FMR uniform mode ($\vec{k}=0$ magnon) to spin waves with finite in-plane wave vector $\vec{k}$, producing an additional damping channel for the FMR mode. In this case, for an applied field along the easy axis, the spin wave dispersion is given by

$$\begin{aligned}\omega^2\left(\vec{k}\right) &= \omega^2{}_{FMR} - 2\pi\gamma^2 M_s kd\left(H_0 - \left[H_0 + H_s + 4\pi M_s\right]\sin^2\vartheta_{\vec{k}}\right) \\ &\quad + \gamma^2\left(2H_0 + H_s + 4\pi M_s\right)Dk^2,\end{aligned} \tag{3.5}$$

where D is exchange stiffness, d is the film thickness, H_0 is the applied in-plane field (including uniaxial anisotropy), H_s is the surface anisotropy and ϑ_k is the in-plane angle between $\vec{k}$ and H_0. From equation (3.5), it is seen that the dipolar interaction leads to a term (2nd term) which is linear in wave vector k whose magnitude could be negative, while the exchange interaction results in a term (3rd term) quadratic in k. Because of a competition between these two terms, it is possible for $\omega^2\left(\vec{k}\right)$ to have a negative slope so that there exists spin wave modes degenerate with the FMR uniform precession. (Figure 3.10) This happens when

$$\sin^2\left(\vartheta_{\vec{k}}\right) < \frac{H_0}{2H_0 + H_s + 4\pi M_s}, \tag{3.6}$$

which is the condition for two-magnon scattering in films. Here, equation (3.6) ensures the conservation of energy while the presence of magnetic defects mediates the momentum mismatch between the degenerate FMR and spin waves modes. Thus, defects play an influential[31-33] role in the two-magnon scattering. Since oblique deposition introduces defects in a controlled manner in the films, it provides an ideal way to study and tune such damping. It is found[30,34] that for rectangular defects of dimensions *m* and *n*, where *m* is parallel to the uniaxial anisotropy, the two-magnon linewidth ΔH_{2M} is given by

$$\begin{aligned}\Delta H_{2\mathrm{M}} \quad = \quad & \frac{\Gamma_o}{\left(2H+a+b\right)^2}\Bigg[\left(H+a\right)^2+\left(\left\langle\frac{m}{n}\right\rangle-1\right)\times\Big(\left(H+a\right)\cos^2\left(\phi_H-\eta\right) \\ & +\left(H+b\right)\cos\left(2\phi_H-2\eta\right)\Big)^2-\left(\left\langle\frac{n}{m}\right\rangle-1\right)\times\Big(\left(H+b\right)\cos\left(2\phi_H-2\eta\right) \\ & -\left(H+a\right)\sin^2\left(\phi_H-\eta\right)\Big)^2\Bigg]\sin^{-1}\sqrt{\frac{H+a}{H+b}},\end{aligned} \tag{3.7}$$

where Γ_0 is a constant denoting the strength of two-magnon scattering and $\langle\ \rangle$ denotes an average over the defect sizes.

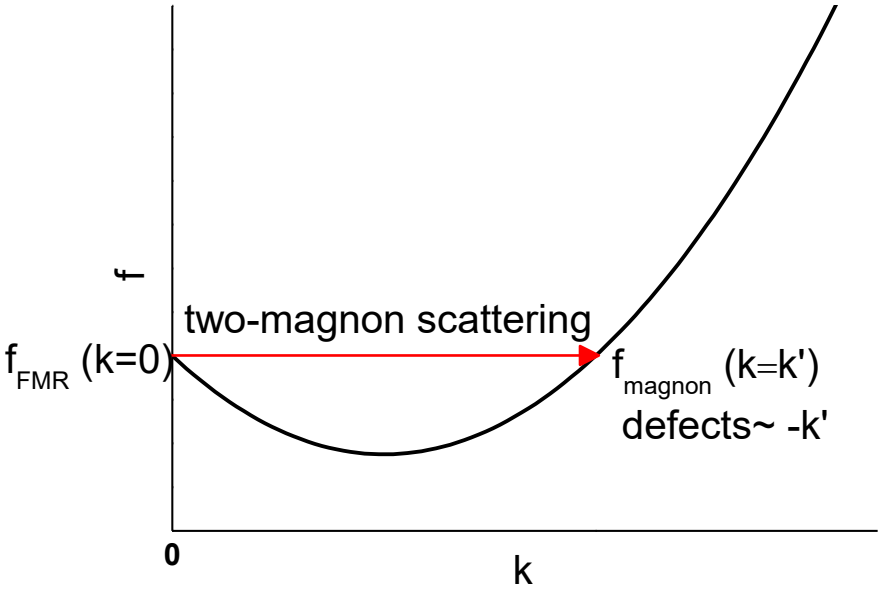

Figure 3.10 Frequency *f* versus in-plane wave vector *k* for a typical magnetic thin film, showing the low-lying acoustic spin wave branch where states with finite wave vectors degenerate with the FMR mode is available.

We present in Figure 3.11 the in-plane angular dependence of ΔH for films with various oblique angles at 2.9 GHz and their fits to equation (3.4). Across the samples, we see that intrinsic damping, obtained by a frequency sweep and fitting to $\Delta H_{\text{int}} = 2\alpha\omega/\gamma$, is relatively constant across various oblique angles at around 10 Oe. The damping constant α is extracted and plotted in Figure 3.13, which remains relatively constant with no clear trends across oblique angles. This somewhat expected, as intrinsic damping is only dependent on material composition and thus should not be drastically affected by oblique deposition. As the oblique angle increases, the two-magnon damping becomes more pronounced, especially for $42°$ and $45°$ in which the two-magnon damping shows a clear two-fold symmetric sinusoidal behaviour. This is consistent since oblique deposition is known to induce the formation of ordered defects in the form of inclined columnar structures[17-19] from which two-

magnon scattering can occur. As columnar structures are inclined normal to the incidence of deposition and thus has an in-plane two-fold symmetry, the two-magnon scattering strength[34,35] thus follows the same symmetry. These columnar structural defects induced by oblique sputtering could be adequately modelled as rectangular magnetic defects in equation (3.7), as evidenced by the good fits in Figure 3.11. We note that at lower oblique angles (17°, 27° and 39°), their angular linewidth spectra shows some deviation from isotropic behaviour towards two-magnon scattering, which is likely due to the result of the formation of less well-ordered defects that causes the two-magnon scattering mechanism to be less efficient at lower oblique angles.

We have measured the films via AFM and transmission electron microscopy (TEM) in an attempt to determine the presence and distribution of defects. Figure 3.12 shows the results for two representative films 0° and 45° oblique. The AFM results for both films indicate a surface roughness of <1 nm showing that the films are smooth and continuous with no large defects. The corresponding TEM images for both films shows nano-sized grains indicating good film quality. Notably, we observe that the grain sizes for 45° is much larger than that of 0°, an observation which is also reflected in Figure 3.17 later. No anisotropic (i.e rectangular) defects are observed for the 45° film, which is likely because the columar grains are tilted in oblique deposition and hence will only show up in a cross-section. However, our cross-sectional images done via scanning electron microscopy are inconclusive due to poor resolution and noise. Regardless, the rectangular defect model in equation (3.7) should still be valid here since the tilted columnar grains induced by oblique deposition introduce anisotropic magnon scattering with the same symmetry as that by rectangular defects.

Lastly, we also note that the mosaicity contribution associated with magnetic dispersion decreases with increasing oblique incidence (Figure 3.11), which we attribute to

the increased uniaxial anisotropy with increasing oblique incidence due to the formation of ordered, elongated grains with reduced dispersion.

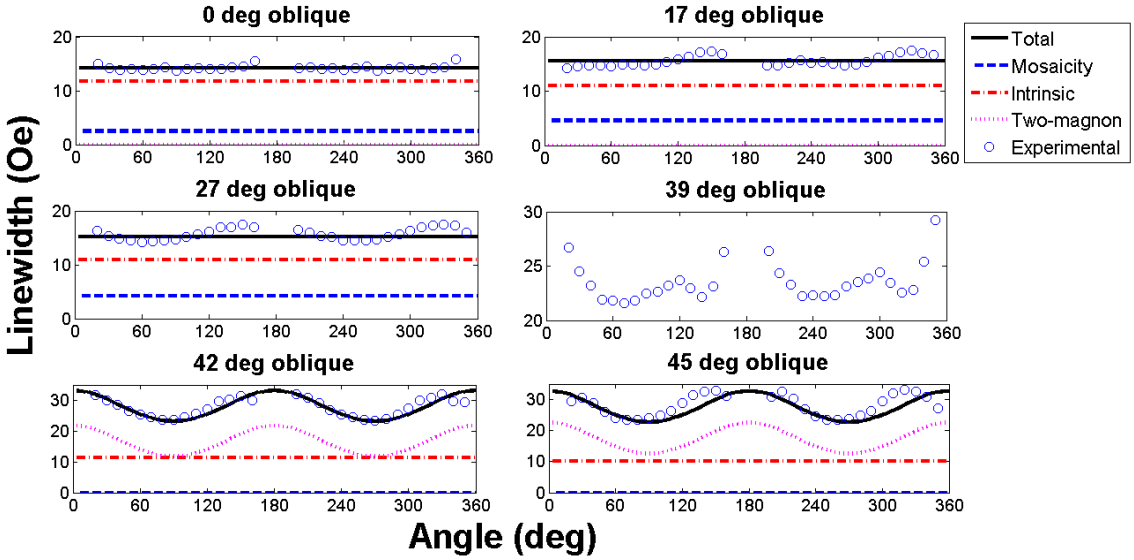

Figure 3.11 In-plane angular dependence of field linewidth ΔH for films with various oblique angles at 2.9 GHz. Lines represent fits to equation (3.3). Adapted with permission from Ref. [26].

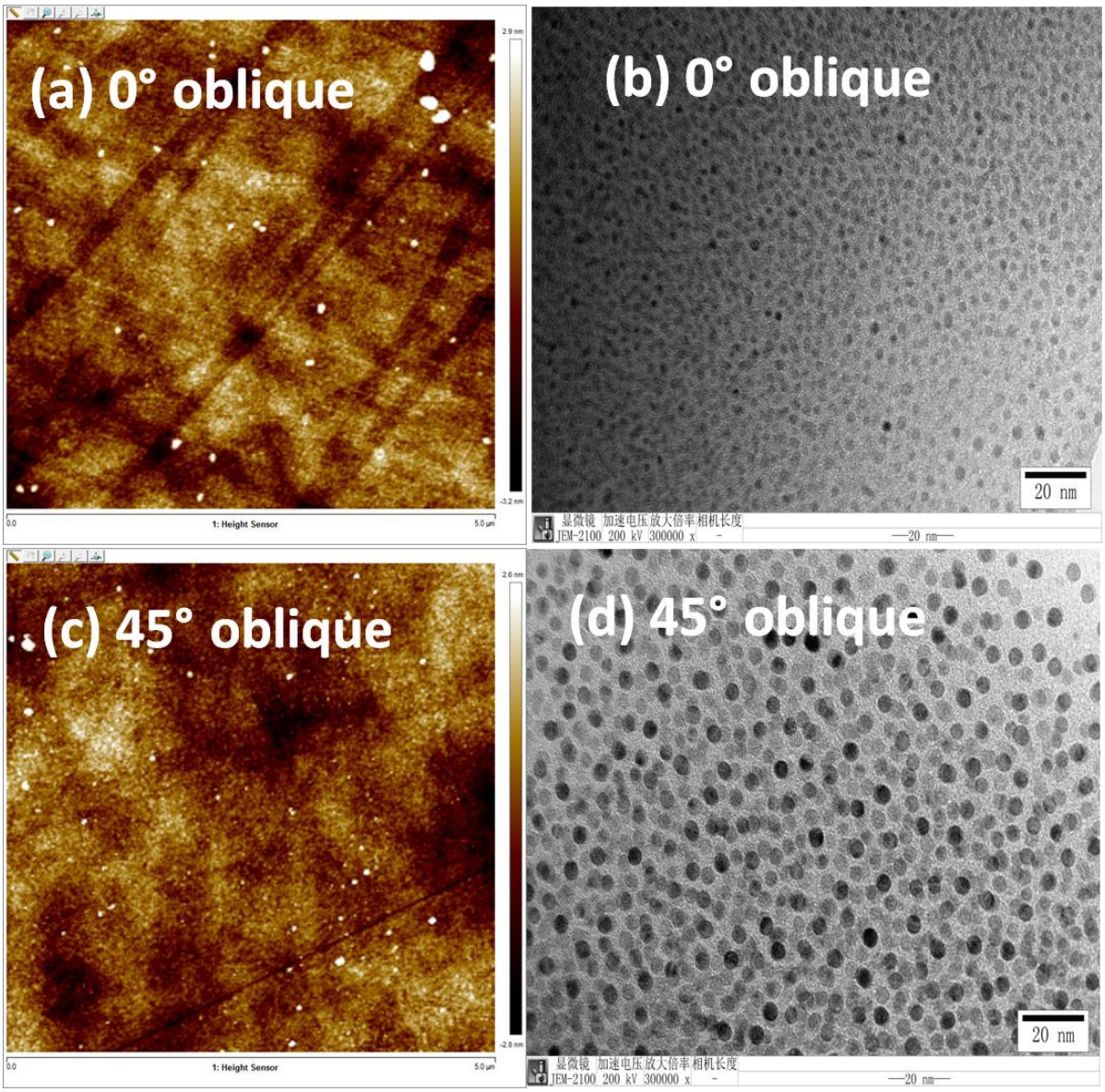

Figure 3.12 $5\mu m \times 5\mu m$ AFM image of (a) 0° oblique and (b) 45° oblique FeAlSi films and their corresponding transmission electron microscopy (TEM) images at (c) and (d) respectively.

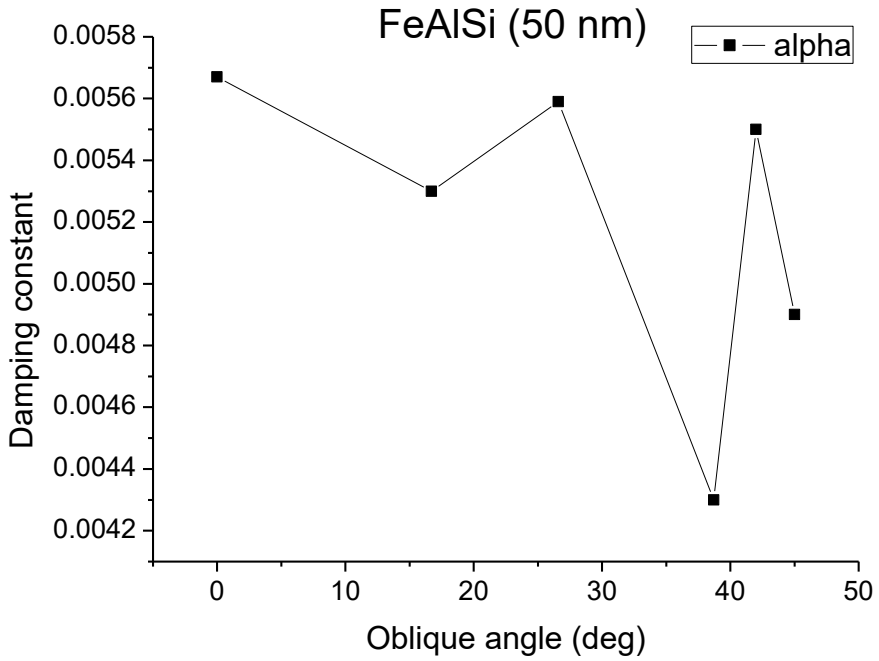

Figure 3.13 Damping constant as a function of oblique angle for FeAlSi films.

3.5.2 Magneto-transport properties: AMR and AHE

In this section, we discuss the magneto-transport properties associated with anisotropic magneto-resistance (AMR) and the anomalous Hall effect (AHE) of the obliquely sputtered FeAlSi films. From the V_{DC} spectra obtained previously, a fit to the Lorentzian and dispersive lineshapes in equation (3.2) also yield the coefficients A_L and A_D respectively that contains information about the magnitude of AMR and AHE whose contributions could be separated by an angular measurement and analysis. From equation (3.2), we see that AMR and AHE due to the dominant j_x component of the microwave current have orthogonal microwave phase Φ and in-plane H angular ϕ_H dependences of $\sin\Phi\sin\phi_H\cos(2\phi_H)$ and

$\cos\Phi\sin\phi_H$ respectively for A_L, and $\cos\Phi\sin\phi_H\cos(2\phi_H)$ and $\sin\Phi\sin\phi_H$ respectively for A_D. Therefore, an angular fitting to equation (3.2) can reliably separate these contributions.

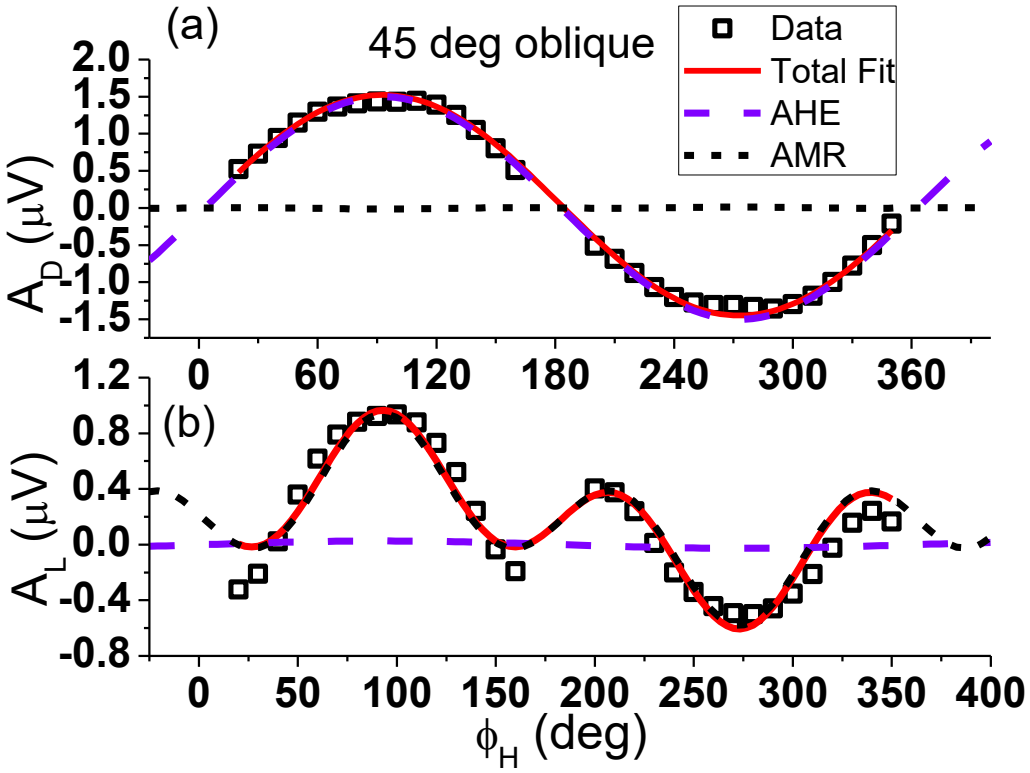

Figure 3.14 Angular ϕ_H dependence of (a) A_D and (b) A_L for the 45° obliquely-sputtered FeAiSi film, showing the respectively contributions of AHE and AMR to V_{DC}.

As an illustration, Figure 3.14 above presents the angular ϕ_H dependence of A_D and A_L obtained from the V_{DC} spectra 45° oblique angle, showing the individual contributions from AMR and AHE. The fitted parameters are V_{AMRx}=0.76 μV, V_{AHE}=-1.5 μV and F=89°. It can be seen that A_D mainly has a sinusoidal angular dependence, while A_L exhibits a four-fold angular symmetry. This is due to the fact that the dominant contribution to A_D comes from AHE, while the dominant contribution to A_L stems from AMR, as the microwave phase F here is close to 90°. The same trend is observed across the range of oblique angles investigated, as shown in Figure 3.15. From Figure 3.15, we also observe that the magnitude

of both A_L and A_D appears to decrease significantly with increasing oblique angle from 0° to 45°, suggesting that both AHE and AMR decreases with increasing oblique angle.

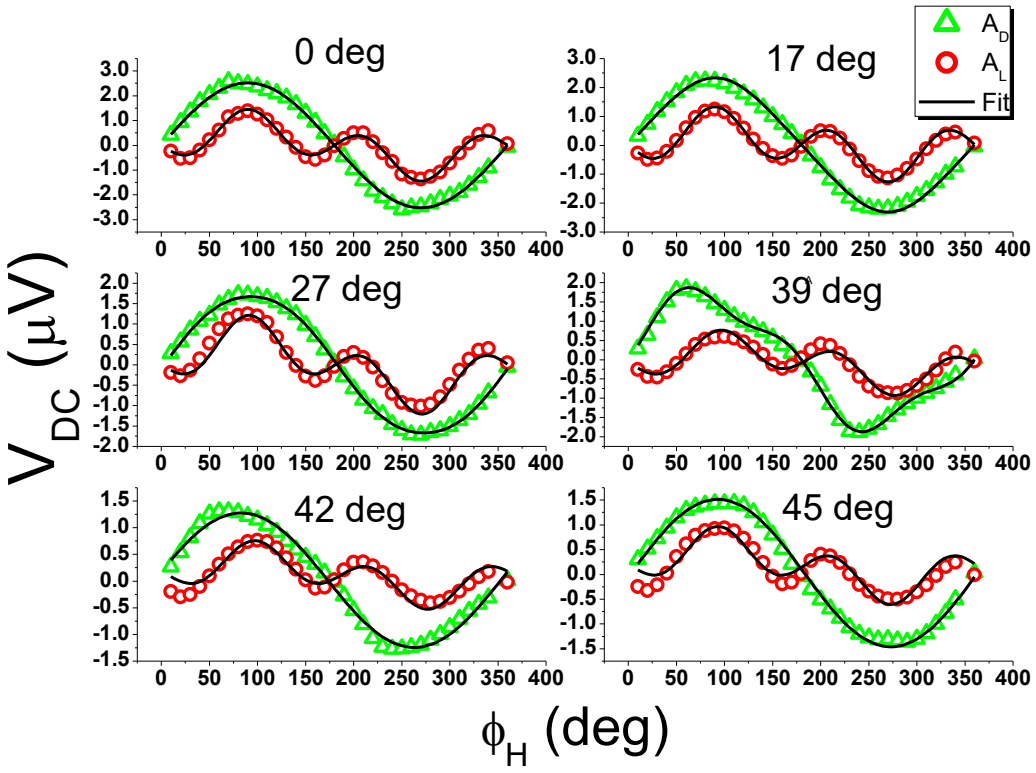

Figure 3.15 Angular ϕ_H dependence of V_{DC} and the fits to A_L and A_D, for various obliquely sputtered FeAlSi films.

To quantify this, we can extract the anomalous Hall coefficient R_{EH} and anisotropic magneto-resistance $\Delta\rho$ from measured values of V_{AMRx} and V_{AHE}. The required quantities A_{xx}, A_{xy} and M_s are easily determined as the magnetic properties have been characterised earlier. The quantities microwave field h and current j_x are more cumbersome to determine since they cannot be measured directly.

An FMR experiment with a vector network analyser (VNA) using our shorted microstrip fixture has been performed to determine h from the power absorbed P_{ab} by the sample at FMR, given by

$$P_{ab} = V \frac{4\pi M_0 \gamma}{4\alpha} h^2 \left[\frac{4\pi M_0 \gamma + \sqrt{\left(4\pi M_0 \gamma\right)^2 + 4\omega^2}}{\sqrt{\left(4\pi M_0 \gamma\right)^2 + 4\omega^2}} \right], \qquad (3.8)$$

where V is the volume of the film. P_{ab} is related to the measured reflection coefficient S_{11} by $P_{ab} = P_{in}\left(1 - |S_{11}|^2\right)$, where P_{in} is the input power and line losses have been taken into account through calibration. Since all other quantities on the RHS of equation (3.8) are known, h can be determined from S_{11} measurements with a VNA. Based on this method, we find that at 18 dBm power used in our experiment, $|\vec{h}| = 0.11 \pm 0.01$ Oe . This value is consistent with that obtained via finite-element simulations as discussed earlier in the preceding section. Since j_x could not be determined easily in a similar manner, we estimate it to be $\sim 1 \times 10^7$ A m^{-2} with finite-element simulations, whose value varies slightly due to the differing resistances of the samples which we take into account. With these determined values, we then calculate R_{EH} and $\Delta\rho$ for films with various oblique angles, summarizing them in Figure 3.16.

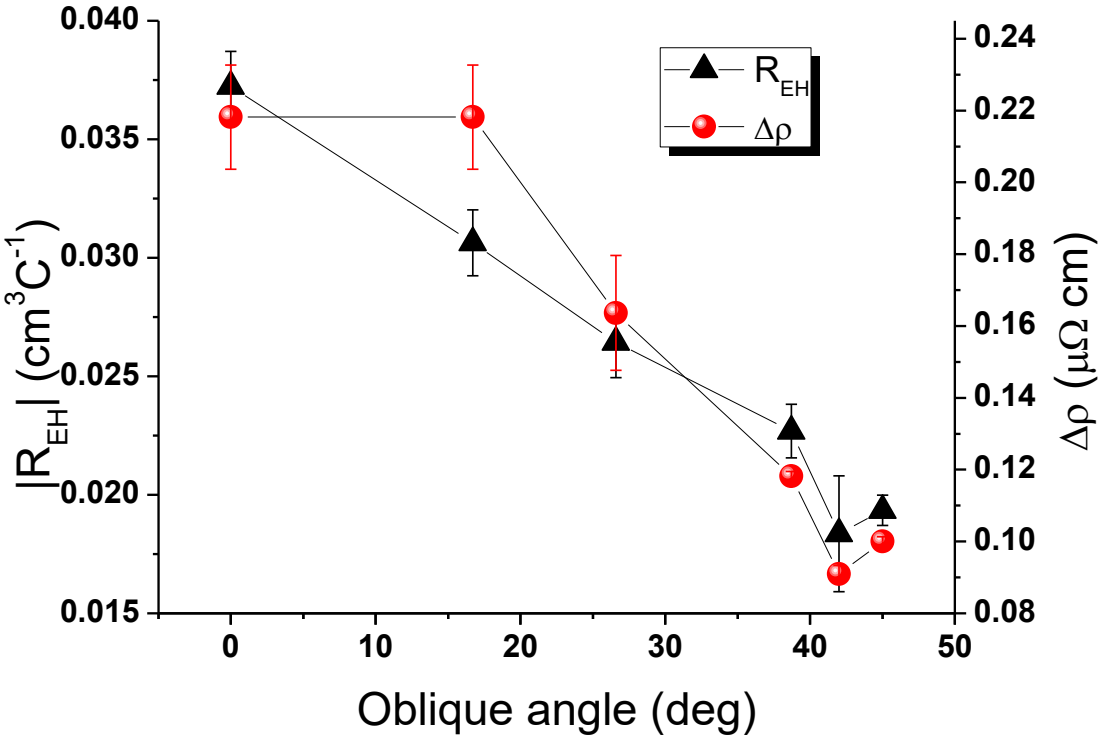

Figure 3.16 Oblique deposition angle dependence of the anomalous Hall coefficient R_{EH} and anisotropic magneto-resistance $\Delta\rho$. The error bars are due to A_L and A_D fitting errors (±1 standard deviation). Adapted with permission from Ref. [26].

From Figure 3.16, we can see that both R_{EH} and $\Delta\rho$ decreases quite significantly with increasing oblique angles. As oblique incidence increases from 0° to 45°, both R_{EH} and $\Delta\rho$ decreases by more than 50%. This trend suggests that the defects and structural changes induced by oblique deposition have a pronounced effect on both AHE and AMR, and thus can be reliably used to tune and study both quantities. X-ray diffraction (XRD) measurements on the FeAlSi films (Figure 3.17) confirm such structural changes in atomic arrangement, where the (200) peak is seen to increases from 2.0100 to 2.0177 Å as the oblique angle increases from 0° to 45°. Our results show that other than electrical[24] resistance and magnetic anisotropy and saturation magnetisation[22,23,36], oblique deposition can also be an effective way to tune magneto-transport such as AMR and AHE. However, the exact mechanism is

still unclear and further research is needed to elucidate the relation between the oblique-induced structural changes to both AMR and AHE. Lastly, we note that the magnitude of AHE for our FeAlSi films are comparable to Co/Mn doped FeSi alloy[15], which have been touted to be promising candidates for magnetic semiconductors.

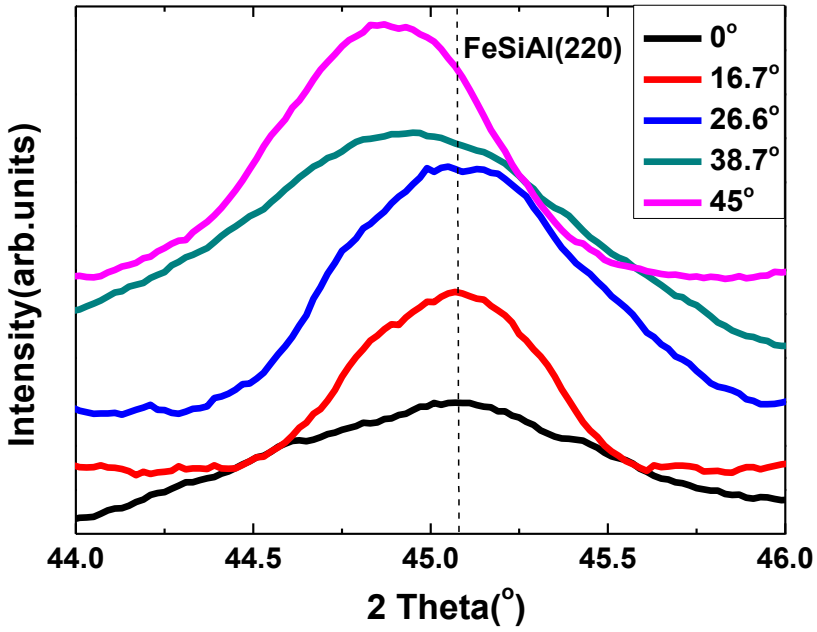

Figure 3.17 XRD spectra of FeAlSi films of various oblique deposition angles.

3.6 Conclusion

In this chapter, the feasibility and potential of SRE as a means for the electrical characterisation of FMR in magnetic films have been demonstrated. Unlike the more conventional inductive techniques via a network analyser, electrical detection of FMR via SRE is a powerful tool due to its great sensitivity to both the dynamic magnetic and magneto-transport properties. Using SRE, we have measured and characterised the dynamic magnetic properties as well as AMR and AHE in a series of obliquely-sputtered FeAlSi films.

The results show that FeAlSi films possess excellent magnetic properties such as high saturation magnetisation (13 kG), low intrinsic uniaxial anisotropy and low Gilbert damping (~0.005) as well as a high resistance for lower eddy losses, which can be comparable or even better than the more widely used soft magnetic films such as NiFe and FeCo. (Table 3.2) In addition, a high AHE and AMR are also found for FeAlSi films as compared to NiFe. We also demonstrate that oblique deposition can significantly tune the uniaxial anisotropy and induce two-magnon scattering in such films. The AHE and AMR can also be decreased by more than 50% with increasing oblique angles up to 45°.

Magnetic film	$M_s(G)$	Magneto-crystalline anisotropy (Oe)	α	$\Delta\rho$ ($\mu\Omega$ cm)	$\lvert R_{EH} \rvert$ $\left(\text{cm}^3\ \text{C}^{-1}\right)$
FeAlSi	~13000	~5	0.005	~0.15	~0.03
NiFe	~9000	~0	0.01	~0.01*	~0.00024*

Table 3.2. Comparison of the magnetic and electrical properties of FeAlSi and NiFe films. *Values are derived from experiments done in Chapter 4.

3.7 References

1 J. E. Snyder and J. W. Anderegg, Journal of Applied Physics **91,** 8459 (2002).

2 S. J. Lee, J. E. Snyder, C. C. H. Lo, K. M. Campos-Anderson, J. W. Anderegg, and D. C. Jiles, Journal of Applied Physics **94,** 2607 (2003).

3 E. Legarra, E. Apiñaniz, F. Plazaola, J. A. Jimenez, and A. R. Pierna, Journal of Magnetism and Magnetic Materials **320,** e688 (2008).

[4] X. Zhong, Y. Liu, J. Li, and Y. Wang, Journal of Magnetism and Magnetic Materials **324,** 2631 (2012).

[5] X. Zhong, N. N. Phuoc, G. Chai, Y. Liu, and C. K. Ong, Journal of Alloys and Compounds **610,** 126 (2014).

[6] E. Saitoh, M. Ueda, H. Miyajima, and G. Tatara, Applied Physics Letters **88,** 182509 (2006).

[7] K. Ando, S. Takahashi, K. Harii, K. Sasage, J. Ieda, S. Maekawa, and E. Saitoh, Physical Review Letters **101,** 036601 (2008).

[8] K. Ando, Y. Kajiwara, S. Takahashi, S. Maekawa, K. Takemoto, M. Takatsu, and E. Saitoh, Physical Review B **78,** 014413 (2008).

[9] O. Mosendz, V. Vlaminck, J. E. Pearson, F. Y. Fradin, G. E. W. Bauer, S. D. Bader, and A. Hoffmann, Physical Review B **82,** 214403 (2010).

[10] O. Mosendz, J. E. Pearson, F. Y. Fradin, G. E. W. Bauer, S. D. Bader, and A. Hoffmann, Physical Review Letters **104,** 046601 (2010).

[11] K. Ando, S. Takahashi, J. Ieda, Y. Kajiwara, H. Nakayama, T. Yoshino, K. Harii, Y. Fujikawa, M. Matsuo, S. Maekawa, and E. Saitoh, Journal of Applied Physics **109,** 103913 (2011).

[12] B. F. Miao, S. Y. Huang, D. Qu, and C. L. Chien, Physical Review Letters **111,** 066602 (2013).

[13] P. Hyde, L. Bai, D. M. J. Kumar, B. W. Southern, C. M. Hu, S. Y. Huang, B. F. Miao, and C. L. Chien, Physical Review B **89,** 180404(R) (2014).

[14] Y. Ando, K. Ichiba, S. Yamada, E. Shikoh, T. Shinjo, K. Hamaya, and M. Shiraishi, Physical Review B **88,** 140406(R) (2013).

[15] N. Manyala, Y. Sidis, J. F. DiTusa, G. Aeppli, D. P. Young, and Z. Fisk, Nat Mater **3,** 255 (2004).

[16] M. S. Cohen, E. E. Huber, G. P. Weiss, and D. O. Smith, Journal of Applied Physics **31,** S291 (1960).

[17] D. O. Smith, M. S. Cohen, and G. P. Weiss, Journal of Applied Physics **31,** 1755 (1960).

[18] S. L. Zeder, J. F. Silvain, M. E. Re, M. H. Kryder, and C. L. Bauer, Journal of Applied Physics **61,** 3804 (1987).

[19] Y. Hoshi, E. Suzuki, and M. Naoe, Journal of Applied Physics **79,** 4945 (1996).

[20] R. D. McMichael, C. G. Lee, J. E. Bonevich, P. J. Chen, W. Miller, and W. F. Egelhoff, Journal of Applied Physics **88,** 5296 (2000).

[21] N. N. Phuoc, G. Chai, and C. K. Ong, Journal of Applied Physics **112,** 083925 (2012).

[22] N. N. Phuoc, G. Chai, and C. K. Ong, Journal of Applied Physics **112,** 113908 (2012).

[23] N. N. Phuoc, W. Tee Soh, G. Chai, and C. K. Ong, Journal of Applied Physics **113,** 073902 (2013).

[24] W. Takakura, S. Ikeda, and Y. Ueda, Mater. Trans., JIM **42,** 881 (2001).

[25] W. T. Soh, B. Peng, and C. K. Ong, Journal of Physics D: Applied Physics **47,** 285001 (2014).

[26] W. T. Soh, X. Zhong, and C. K. Ong, Applied Physics Letters **105,** 112401 (2014).

[27] J. Smit and H.G. Beljers, Philips Research Reports **10**, 113-130 (1955).

[28] H. Xi and R. M. White, Physical Review B **61,** 80 (2000).

[29] J. Dubowik, K. Załęski, H. Głowiński, and I. Gościańska, Physical Review B **84,** 184438 (2011).

[30] R. Arias and D. L. Mills, Physical Review B **60,** 7395 (1999).

[31] R. D. McMichael, D. J. Twisselmann, J. E. Bonevich, A. P. Chen, W. F. Egelhoff, and S. E. Russek, Journal of Applied Physics **91,** 8647 (2002).

[32] R. McMichael, D. Twisselmann, and A. Kunz, Physical Review Letters **90,** 227601 (2003).

[33] R. D. McMichael and P. Krivosik, Magnetics, IEEE Transactions on **40,** 2 (2004).

[34] R. L. Rodríguez-Suárez, L. H. Vilela-Leão, T. Bueno, A. B. Oliveira, J. R. L. de Almeida, P. Landeros, S. M. Rezende, and A. Azevedo, Physical Review B **83,** 224418 (2011).

[35] I. Barsukov, P. Landeros, R. Meckenstock, J. Lindner, D. Spoddig, Z.-A. Li, B. Krumme, H. Wende, D. L. Mills, and M. Farle, Physical Review B **85,** 014420 (2012).

[36] M. T. Umlor, Applied Physics Letters **87,** 082505 (2005).

4 An angular analysis to separate spin pumping-induced inverse spin Hall effect from spin rectification in a NiFe/Pt bilayer

4.1 Introduction

In the preceding chapter, we have demonstrated how the spin rectification effect can be useful for the sensitive characterisation of metallic magnetic films. The present chapter deals with the role of SRE in the field of spintronics, where it can often be a hindrance due to its contamination with the electrical signal of interest.

The spin Hall effect (SHE) is a phenomenon first predicted in 1971 by Dyakonov and Perel[1], whose theory is further elaborated and generalized by Hirsch[2] (via defect scattering) in 1999 and by Sinova *et al*[3] (via Rashba spin-orbit coupling) in 2004. In SHE, a charge current comprising of unpolarised electrons is converted to a polarised spin current flowing in the transverse direction. Conversely, the conversion of polarised spin currents into transverse unpolarised charge currents is called the inverse spin Hall effect (ISHE). Such spin currents are instrumental in the field of spintronics[4], where the spin degree of freedom of electron is used to manipulate magnetic spins to yield novel and useful applications. As such, both SHE and ISHE have attracted immense research interest[5-21] in the recent decade, particular in its spin-to-charge (and vice versa) conversion efficiency, which is characterised by the spin Hall angle θ_{SHE}. Large θ_{SHE} values are desired to produce significant spin currents, which could even be sufficient to flip magnetic spins via spin torque[17]. Typical materials that have significant θ_{SHE} investigated thus far include heavy metals such as Pt[12,22,23] and Pd[10]. More

recently, SHE has also been explored in semiconductors such as germanium[21] and even in the ferromagnetic metal NiFe[20].

Experimental determination of the spin-to-charge current conversion efficiency θ_{SHE} generally makes use of a ferromagnetic metallic layer such as NiFe to pump a spin current at FMR into the spin Hall metal, from which the resulting ISHE charge current can be measured. However, such measurements involving spin pumping and ISHE can be complicated by SRE through which additional dc charge currents are also generated via AMR and AHE within the ferromagnetic metal as discussed in the previous chapter. If these two different sources of dc charge currents are not properly understood and separated, it may lead to large errors in estimating θ_{SHE} from the subsequent results. In particular, the relative phase Φ between the microwave current *j* and magnetic field *h* can vary widely across various experimental setups from microwave cavities to transmission lines, thus the resulting varying SRE lineshapes can drastically affect the results if not properly taken into account. This particular reason may explain the large discrepancies of θ_{SHE} measured for Pt in current literature, which can vary by one order of magnitude from 0.0067[11] to 0.08[24].

This cumbersome problem of separating SRE from the ISHE signal of interest has recently been addressed by various groups. Bai *et al*[25] has proposed an effective method to separate ISHE from SRE based on symmetry considerations with an out-of-plane static *H* field with in-plane microwave current and magnetic fields. A similar method has also been proposed by Feng *et al*[16] for an out-of-plane *h* relative to in-plane *H* and *j*. One crucial characteristic of both proposed methods is that they are independent of the relative phase Φ and thus, other than their respective *H*, *h* and *j* configurations, these methods do not depend on other experiment details such as transmission lines, substrates and connectors that Φ is

sensitive to. Nonetheless, as shall be discussed later, we find that an in-plane configuration for all *H*, *h* and *j* can be much more complicated and does not allow for SRE and ISHE separation based on simple symmetry considerations; hence a full angular analysis is required.

In this chapter, we detail a systematic procedure to accurately determine the spin Hall angle of the heavy metal Pt based on a NiFe(permalloy)/Pt bilayer structure. Due to spin pumping at the FMR of the NiFe layer, a spin current is injected into the adjacent Pt layer. In the Pt layer, this injected spin current then dissipates via ISHE into a charge current measureable as a dc voltage, from which we extract the ISHE efficiency θ_{SHE}. However, due to mixing of this dc voltage from ISHE with the self-generated SRE voltage in NiFe, further analysis have to be undertaken before θ_{SHE} can be determined accurately.

4.2 Experimental details

We prepare our single layer NiFe (also called Permalloy (Py)) and bilayer NiFe/Pt films via rf magnetron sputtering onto SiO_2 substrates. The target used is $Ni_{80}Fe_{20}$. For the bilayer NiFe/Pt films, the NiFe layer is deposited first onto the SiO_2 substrates. All prepared samples were from the same batch, with a base chamber pressure of $\sim 7\times10^{-7}$ Torr. The Ar sputtering pressure is kept at 2×10^{-3} Torr and a small magnetic field of ~200 Oe is applied during deposition to induce a small uniaxial anisotropy in the NiFe films. Masks are also placed onto the SiO_2 substrates to pattern some of the films into lateral dimensions of 10mm by 1mm. After the samples are prepared, they are then placed into the shorted microstrip where under microwave excitation at 18 dBm power, the generated dc voltages are

sensitively measured using a lock-in amplifier. For each microwave frequency, an external magnetic field *H* is applied and swept while the dc voltages are measured.

4.3 Theory

4.3.1 Contribution from SRE

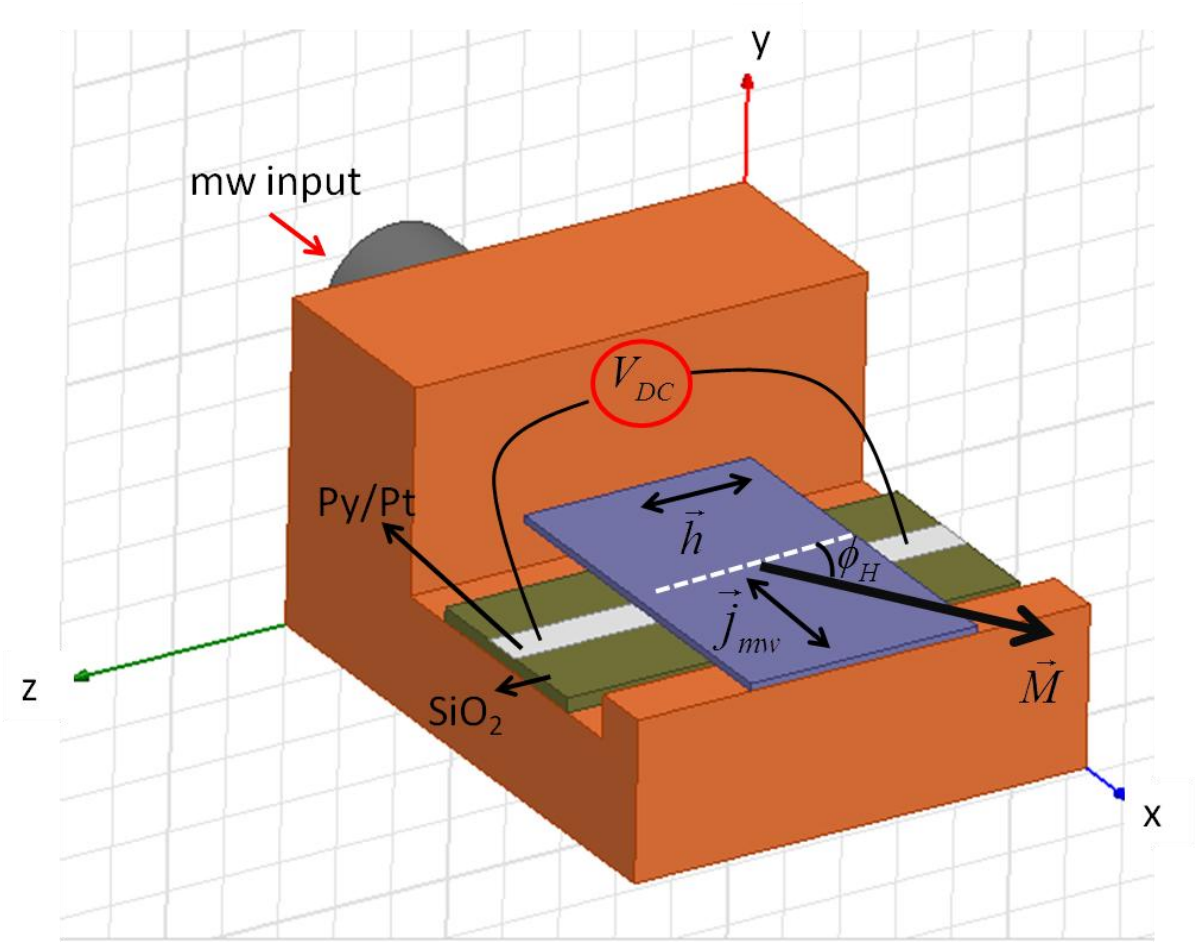

Figure 4.1 Illustration of the sample orientation within the shorted microstrip fixture during measurement. Adapted with permission from Ref. [26].

The relative fields and measurement configuration for SRE contribution is exactly the same as that discussed in chapter 3, from which we have already found the expression for the SRE voltage V_{DC} in the single layer film in equation (3.2). However in this case for a bilayer

NiFe/Pt film, we should also consider the shunting effect of the Pt layer on the SRE current $\vec{j}_{SRE}$ produced within the NiFe layer. The shunting effect of Pt on $\vec{j}_{SRE}$ simply reduces the measured SRE voltage V_{SRE} by a factor and thus does not affect the angular analysis later to separate SRE from ISHE.

4.3.2 Contribution from ISHE

At FMR, the precession of the spins within a ferromagnetic film such as NiFe can adiabatically inject a spin current into an adjacent conducting layer, in a phenomenon called spin pumping first discovered by Tserkovnyak *et al*[27,28] in 2002. Since the injected spin currents carry angular momentum, the net angular momentum of the remaining spins are lost and this manifests as an increase in effective Gilbert damping. This injected spin current $\vec{j}_s$ at the NiFe/Pt interface is given by[12,29]

$$\vec{j}_s = \left(\frac{\hbar}{2eM_s}\right)^2 G_{\uparrow\downarrow}\left[\vec{M}\times\frac{\partial\vec{M}}{\partial t}\right], \qquad (4.1)$$

where e is the electronic charge and $G_{\uparrow\downarrow}$ is the spin mixing conductance at the NiFe/Pt interface which can be estimated as $G_{\uparrow\downarrow} = 4\pi M_s t_{NiFe}\left(\alpha_{NiFe/Pt} - \alpha_{NiFe}\right)/\left(\gamma\hbar\right)$. As seen, $\vec{j}_s$ is proportional to the damping enhancement observed in NiFe/Pt films as compared to a single NiFe film of the same thickness. Once injected at the interface, $\vec{j}_s$ then starts to decay as it passes through the Pt layer due to spin relaxation, so that the effective spin current as it passes through a distance y within the film (where y=0 is the NiFe/Pt interface) is[12]

$$\vec{j}_{seff}(y) = \vec{j}_s \frac{\sinh\left[\left(t_{Py} - y\right)/\lambda_{Pt}\right]}{\sinh\left(t_{Py}/\lambda_{Pt}\right)} \vec{j}_s, \qquad (4.2)$$

where λ_{Pt} is the spin diffusion length of the Pt film and t_{Py} is the NiFe film thickness. This spin current is then converted into a charge current $\vec{j}_c$ via ISHE:

$\vec{j}_c = 2e\theta_{SHE} \int_0^{t_{Py}} \left[y \times \vec{j}_{seff}(y) \right] dy / \left(\hbar t_{Py}\right)$, where we have taken the average over the film thickness t_{Py}. Calculating the quantities with $\vec{m}$ given in (1.9) based on the configuration in Figure 4.1, we find that the resulting ISHE dc current is

$$\begin{aligned} \vec{j}_c(t) &= KA_{xy}h\omega \left[\begin{pmatrix} A_{xx}hL\cos\phi_H \sin^2\phi_H \cos^2\omega t \\ 0 \\ -A_{xx}hL\sin^3\phi_H \cos^2\omega t \end{pmatrix} + \begin{pmatrix} -4\pi M_s D\cos\omega t \sin^2\phi_H \\ 0 \\ -4\pi M_s D\cos\omega t \sin\phi_H \cos\phi_H \end{pmatrix} \right] \\ &= \vec{j}_c^{\,dc} + \vec{j}_c^{\,ac}, \end{aligned} \qquad (4.3)$$

where $K = e\theta_{SHE}\lambda_{Pt} g_{\uparrow\downarrow} \tanh\left(t_{Pt}/2\lambda_{Pt}\right)/32\pi^3 M_s{}^2 t_{Pt}$ and t_{Pt} is the thickness of the Pt film. From equation (4.3), we see that the first term $\vec{j}_c^{\,dc}$ generates a rectified dc voltage V_{ISHE} measurable by our setup. The second term $\vec{j}_c^{\,ac}$ however exhibits the same sinusoidal time-dependence as the microwave and will thus average to zero in our lock-in measurement. Hence, only $\vec{j}_c^{\,dc}$ would be detected as a dc voltage in our setup. As our measurement is along the *z*-axis, the detected V_{ISHE} is contributed by $\vec{j}_c^{\,dc} \bullet \hat{z} = -KA_{xy}A_{xx}h^2\omega L \sin^3\phi_H \cos^2\omega t$. The $\sin^3\phi_H$ angular dependence is distinct to the dc ISHE voltage for in-plane field configurations, which can be deduced by noting that $\vec{m} \sim \sin\phi_H$. Thus, the spin pumping term $\vec{m} \times d\vec{m}/dt$ gives a factor of $\sin^2\phi_H$ and the final $\sin\phi_H$ factor is due to the projection of $\vec{j}_c^{\,dc}$

along the measurement direction *z*. A noteworthy point here is that the resulting ISHE voltage due to $\vec{j}_c^{\,dc}$, unlike the SRE voltage, is independent of the microwave current $\vec{j}$.

It is interesting to note that the ac component of $\vec{j}_c$ is greater than its dc component by a factor of $4\pi M_s/(A_{xx}h)$ which is typically two orders of magnitude. The ac component is currently of great interest[29,30] in part due to its large magnitude. However, it is extremely difficult to measure directly due to mixing with significant eddy currents $\vec{j}$ present in the sample induced by the microwave. Since $\vec{j}_c^{\,ac}$ flows within the sample with the same frequency as the microwave current $\vec{j}$, the former can generate a rectified dc voltage via SRE in NiFe. This additional SRE voltage due to the ac component of ISHE current can be calculated as

$$V_{DC}^{\,SRE}\left(\vec{j}_c^{\,ac}\right) = -4\pi M_s \omega h^2 \sin^3\phi_H \left[A_{xy}^{\,2} R_{EH} KlDL/2 - A_{xx}A_{xy}A\Delta RKD^2/(8\pi M_s)\right]. \qquad (4.4)$$

From (4.4), we see that both terms have the same angular dependence as V_{ISHE} and are thus inseparable from it via an angular measurement. However, within our experimental settings, we find that $\left|\vec{j}_c^{\,ac}\right| \sim 10^4$ Am^{-2}, which is about three orders smaller than the microwave current $\vec{j}$, where we have estimated that $\vec{j} \sim 10^7$ Am^{-2} based on finite element simulations earlier in the previous chapter. Thus, $\vec{j}_c^{\,ac}$ can be ignored since it only generates SRE voltages at the sub-nV level, which is too low to be detected in our setup. Although SRE due to $\vec{j}_c^{\,ac}$ generated from spin pumping and ISHE can be ignored here, it remains to be an interesting prospect to consider as it provides a method to detect the ac component of the spin pumped current. However in this case, the microwave current still needs to be suppressed to avoid spurious signals, which could possibly be achieved by placing the sample in the region of a

microwave cavity with zero electric field. The angular symmetry between the $V_{DC}{}^{SRE}\left(\vec{j}_c{}^{ac}\right)$ and $V_{DC}{}^{ISHE}$ terms still needs to be broken, which can be achieved by modifying any one of the field components to lie out-of-plane.

4.3.3 Separating the ISHE voltage from SRE

Within our NiFe/Pt samples, dc voltage as measured by the lock-in amplifier under microwave excitation consists of a sum of both SRE and ISHE contributions. Our present aim is to separate isolate the ISHE contribution from SRE in the measured dc voltages so that the spin Hall angle θ_{SHE} of Pt can be determined. The total dc voltage is given by

$$V_{DC}{}^{total} = A_L{}'L + A_D{}'D, \qquad (4.5)$$

where

$$A_L{}' = -\sin\Phi\left[V_{AMR}{}^{x}\sin\phi_H\cos 2\phi_H - V_{AMR}{}^{z}\sin\phi_H\sin 2\phi_H\right] - V_{AHE}\cos\Phi\sin\phi_H + V_{DC}{}^{ISHE}\sin^3\phi_H,$$
$$A_D{}' = \cos\Phi\left[V_{AMR}{}^{x}\sin\phi_H\cos 2\phi_H - V_{AMR}{}^{z}\sin\phi_H\sin 2\phi_H\right] - V_{AHE}\sin\Phi\sin\phi_H.$$

Here, $V_{AMR}{}^{x(z)}$ represents the AMR voltages induced by the *x(z)*-component of the microwave current, V_{AHE} and Φ are the AHE voltage and phase difference between $\vec{j}$ and $\vec{h}$ respectively. We see that only $V_{AMR}{}^{z}$ is an even function of ϕ_H while the rest are all odd, therefore it is not possible to separate ISHE from SRE based on simple symmetry considerations alone (i.e. subtracting voltages measured along $-H_0$ and $+H_0$ directions) such as that done in Ref. [25] and [16]. However, note that a full angular measurement and analysis would be able to separate these contributions since they have mutually orthogonal angular ϕ_H dependences.

4.4 Results and Discussion

4.4.1 Separating the ISHE dc voltage from SRE

We have measured the induced dc voltages V_{DC}^{total} as a function of applied field H_0 along ϕ_H at various microwave frequencies for a series of NiFe/Pt and NiFe films. Figure 4.2 (a) shows, for the patterned 1mm by 10mm Py(20nm)/Pt(10nm) film, the V_{DC}^{total} spectra at various frequencies. As expected, the voltage peaks in the spectra, which consist of a combination of lorentzian (L) and dispersive (D) lineshapes, is seen to increase with increasing frequency in accordance with the Kittel formula for FMR in thin films. The angular variation of V_{DC}^{total} at 2 GHz is also shown in Figure 4.2(b), where one observes that the lineshapes vary with ϕ_H, which can be fitted to equation (4.5) to separate the ISHE and SRE contributions.

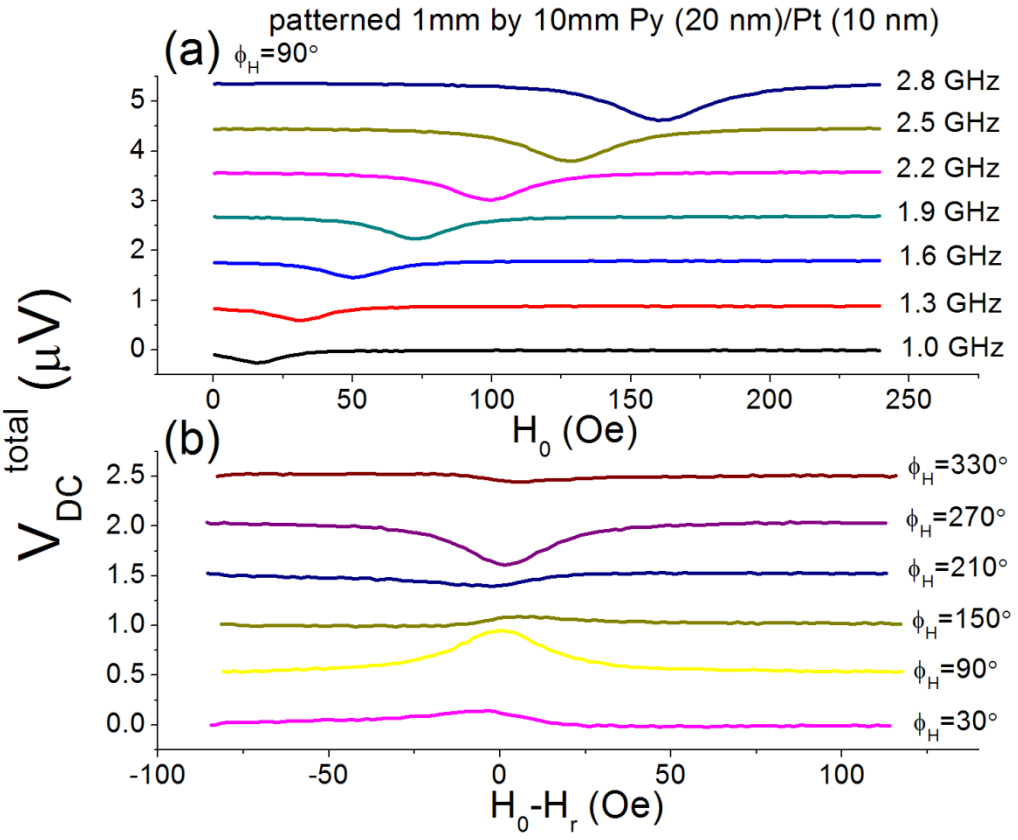

Figure 4.2 (a) Measured dc voltage $V_{DC}^{\ total}$ versus applied field H_0 along $\phi_H = 90°$ at various frequencies *f*, for patterned 1mm by 10mm Py(20nm)/Pt(10nm). (b) Measured voltages as a function of (H_0-H_r) for various ϕ_H, at a fixed frequency of 2 GHz. All plots are offset for clarity. Adapted with permission from Ref. [26].

From the voltage spectra measured in Figure 4.2, we can extract the *L* and *D* components via fitting and plot them in Figure 4.3. We fit, with equation (4.5), the angular dependences of the dispersive amplitude A_D and lorentzian amplitude A_L that has been extracted from the raw voltage spectra and show them in Figure 4.3. The corresponding fitted parameters are summarised in Table 4.1. For the patterned Py/Pt film, we surprisingly find that $V_{AMR}^{\ z} = 0.156\ \mu V$ is much higher than $V_{AMR}^{\ x} = 0.049\ \mu V$, implying that the microwave current predominantly flows in the $\vec{j}_z$ direction rather than $\vec{j}_x$. We can see this even without

detailed fitting by noting that the results show $A_D \approx 0$ for $\phi_H = 90°, 270°$, which cannot be fitted to equation (4.5) if $V_{AMR}{}^z = 0$ as the remaining AMR and AHE terms are never zero independently for $\phi_H = 90°, 270°$ unless in the unlikely situation that their combination cancel exactly at these points. In the latter case however, the data cannot be consistently fitted at other points. We find the best fit for $V_{AHE} \sim 0.01\ \mu$V, noting that a reasonable and consistent fit can still be obtained even if V_{AHE} is set to zero. This is expected since AHE is known to be significantly smaller than AMR in Py. From the A_L' spectra, we extract the ISHE voltage $V_{DC}{}^{ISHE} = 0.5 \pm 0.04\ \mu$V. The best fit for Φ is around 18°.

For the unpatterned Py/Pt film, we have $V_{AMR}{}^z = 0$, $V_{AMR}{}^x = 0.19\ \mu$V, $V_{AHE} \sim 0.03\ \mu$V, $V_{DC}{}^{ISHE} = 0.46 \pm 0.03\ \mu$V and $\Phi = 83°$. Here, we see negligible contribution to AMR from $\vec{j}_z$, consistent with that observed for our (also unpatterned) FeAlSi films in the previous chapter. The values of $V_{DC}{}^{ISHE}$ for both patterned and unpatterned bilayer Py/Pt films are similar, consistent with the fact that the ISHE voltage is independent of the dimensions of the sample in the *x*-direction, since it is orthogonal to the dc measurement direction. Comparing all three samples, we also see that A_L' primarily exhibits a $\sin^3\phi_H$ dependence and is significantly larger than A_D only for the Py/Pt samples (Figures 4.3a, b), evidencing that ISHE (which contributes a symmetric lineshape with a $\sin^3\phi_H$ dependence) is dominant for these samples. In contrast for the single layer Py film (Figure 4.3c), A_L' clearly do not show the $\sin^3\phi_H$ dependence associated with ISHE and is largely similar in magnitude with A_D, showing the fourfold angular symmetry synonymous with SRE due to AMR, as expected.

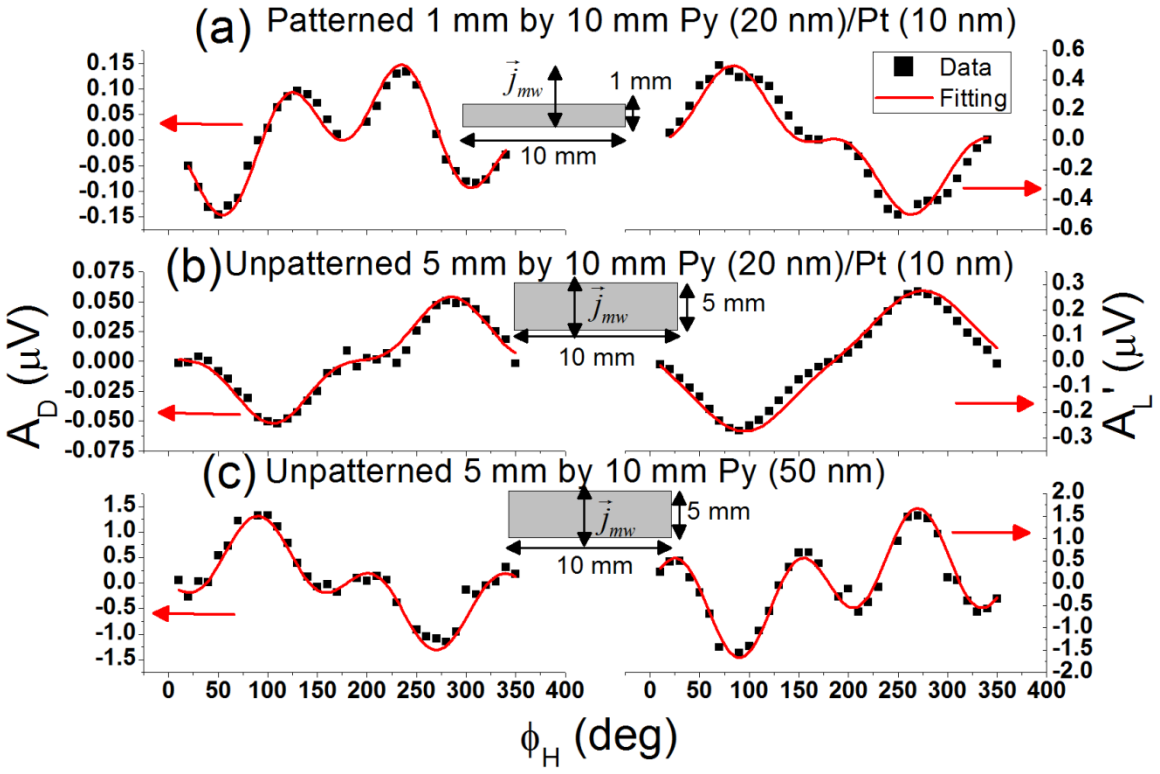

Figure 4.3 The dispersive amplitude A_D (left) and lorentzian amplitude A_L (right) versus in-plane angle ϕ_H for (a) patterned (w=1mm by l=10mm) Py(20nm)/Pt(10nm) film, (b) unpatterned (w=5mm by l=10mm) Py(20nm)/Pt(10nm) film and (c) unpatterned (w=5mm by l=10mm) single layer Py(50nm). Adapted with permission from Ref. [26].

Sample	V_{AMR}^{x}	V_{AMR}^{z}	V_{AHE}	$\left\|V_{DC}^{ISHE}\right\|$	Φ
10 mm by 1 mm Py (20 nm)/Pt (10 nm)	0.049±0.002	0.156±0.005	0.01±0.01	0.5±0.04	18°
10 mm by 5 mm Py (20 nm)/Pt (10 nm)	0.19±0.01	0	0.03±0.01	0.46±0.03	83°
10 mm by 5 mm Py (50 nm)	2.1±0.04	0	0.3±0.05	0	240°

Table 4.1 The voltage contributions based on an angular fit of measured data in Figure 4.3 for three different sample geometries. Error bars reflect fitting errors (±1 standard deviation) All units for *V* are in μV.

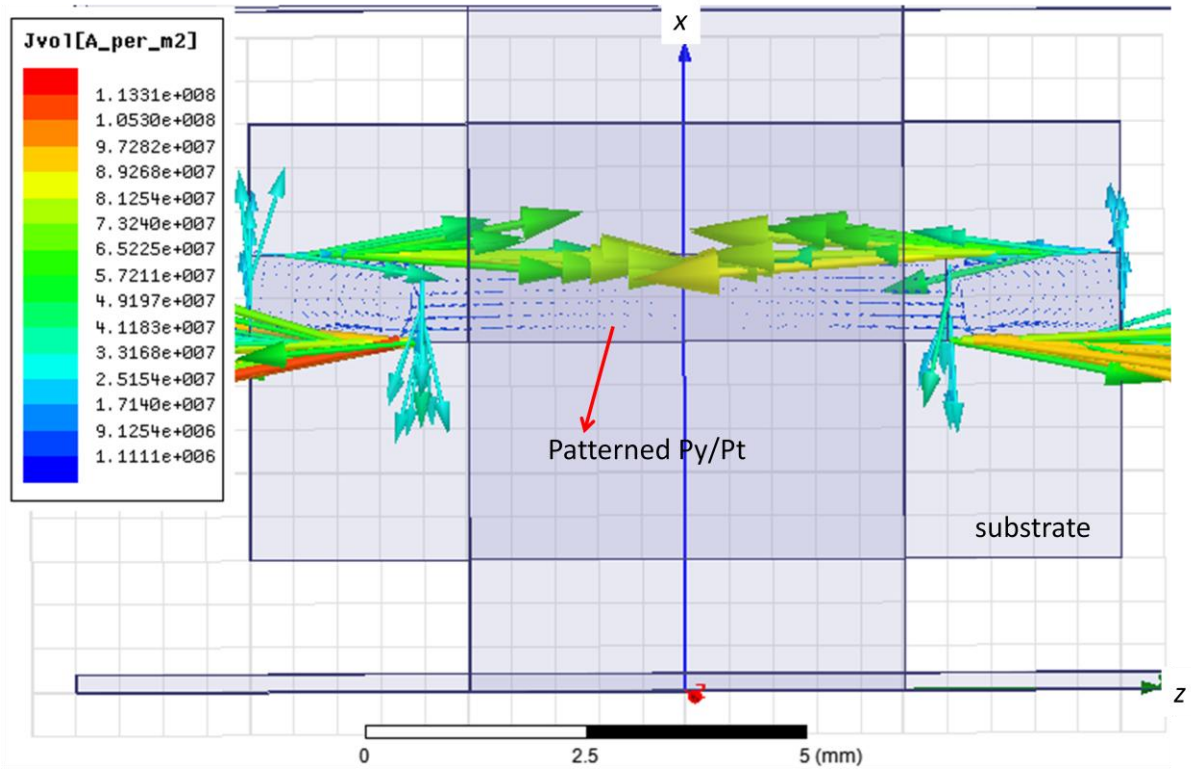

Figure 4.4 Top view of the current density $\vec{j}_{vol}$, in units of Am^{-2}, within the Py/Pt film as obtained from finite element simulations.

To understand the difference in measured AMR voltages as a result of the difference in $\vec{j}_x$ and $\vec{j}_z$ between the patterned and unpatterned films, we conduct a finite element simulation via Ansoft HFSS based on these two configurations. While we would expect $\left|\vec{j}_x\right| \gg \left|\vec{j}_z\right|$ based on the sample-microstrip line coupling (Figure 4.1), this may not true when the sample length w is much shorter than the microstrip line. This is because the microwave current must flow along $\vec{j}_z$ near the sample edges parallel to l due to the boundary condition $\vec{j}_x = 0$, thus this edge effect could be enhanced when w is significantly shorter than the microstrip line. This is indeed confirmed by our simulation results. As shown in Figure 4.4, it is apparent that $\vec{j}_z$ is indeed much higher in magnitude than the $\vec{j}_x$ component, which seems to support our experimental result above that the contribution to AMR from $\vec{j}_z$ for the patterned sample is significantly higher than that of $\vec{j}_x$. However, we point out that symmetric about the centre line of the microstrip line, the directions of $\vec{j}_z$ are always opposite to each other (and therefore, cancels) on each side of the line. This cancellation does not occur for the $\vec{j}_x$ component. Thus, it should be expected that the net effect of $\vec{j}_z$ on AMR should be zero, and so $V_{AMR}{}^{z}$ should be zero for the patterned samples. The fact that this was not the case in our setup is likely due to that the sample is not exactly placed at the centre, so that $\vec{j}_z$ does not cancel totally. For the unpatterned sample, the magnitude of $\vec{j}_z$ is smaller compared to $\vec{j}_x$ and thus, this effect is not as pronounced. However, despite the presence of both components of microwave current in the sample complicating the angular analysis, the results are still unambiguous since both components are orthogonal and thus are still separable.

4.4.2 Determining the spin Hall angle of Pt film

In the earlier section, we have successfully separated the ISHE voltage from SRE based on angular considerations. Following, we shall focus our discussion on the patterned Py/Pt sample and determine the spin Hall angle θ_{SHE} and spin diffusion length of the Pt layer. The results for the unpatterned Py/Pt sample are similar.

From section 4.3.2, we have determined the dc ISHE current $\vec{j}_c^{\,dc}$ for our measurement configuration. This produces a dc ISHE voltage given as

$$V_{DC}^{\ ISHE} = \frac{\theta_{SHE}\lambda_{Pt} l}{\sigma_{Pt} t_{Pt} + \sigma_{Py} t_{Py}} \left\{ \left(\frac{2e}{\hbar} \right) \tanh\left(\frac{t_{Pt}}{2\lambda_{Pt}} \right) \frac{g_{\uparrow\downarrow}\gamma^2 h^2 \hbar \left[4\pi M_0 \gamma + \sqrt{\left(4\pi M_0 \gamma\right)^2 + 4\omega^2} \right]}{8\pi \alpha_{Py/Pt}{}^2 \left[\left(4\pi M_0 \gamma\right)^2 + 4\omega^2 \right]} \right\}, \qquad (4.6)$$

where σ_{Pt} and σ_{Py} are the conductivities of Pt and Py respectively. Here, the current shunting effect[12], where $\vec{j}_c^{\,dc}$ can flow into the Py layer, has been taken into account by the factor on the left side of the curly brackets. We determine the saturation magnetisation $4\pi M_0 = 6101$ G by performing a frequency sweep of our voltage spectra at $\phi_H = 90°$ (Figure 4.5) and fitting H_r to the Kittel equation $f_{FMR} = (\gamma / 2\pi)\sqrt{H_r\left(H_r + 4\pi M_0\right)}$. Using four-point probe method, the conductivities σ_{Py} and σ_{Pt} are measured as 2×10^6 $(\Omega\text{m})^{-1}$ and 3.2×10^6 $(\Omega\text{m})^{-1}$ respectively. To calculate $g_{\uparrow\downarrow}$, the damping constants for Py(20nm)/Pt(10nm) and Py(20nm) are determined to be $\alpha_{Py/Pt} = 0.0145$ and $\alpha_{Py} = 0.011$ respectively, based on a fit of the linewidth spectra to the equation $\Delta H = \Delta H_0 + 2\alpha\omega/\gamma$, where ΔH_0 is the zero-frequency linewidth. Lastly, the microwave magnetic field strength *h*

has been determined in the previous chapter, as $|\vec{h}| = 0.11 \pm 0.01$ Oe. We plot in Figure 4.5 inset the derived h^2 against input microwave power obtained from VNA measurement, showing a consistent linear relationship.

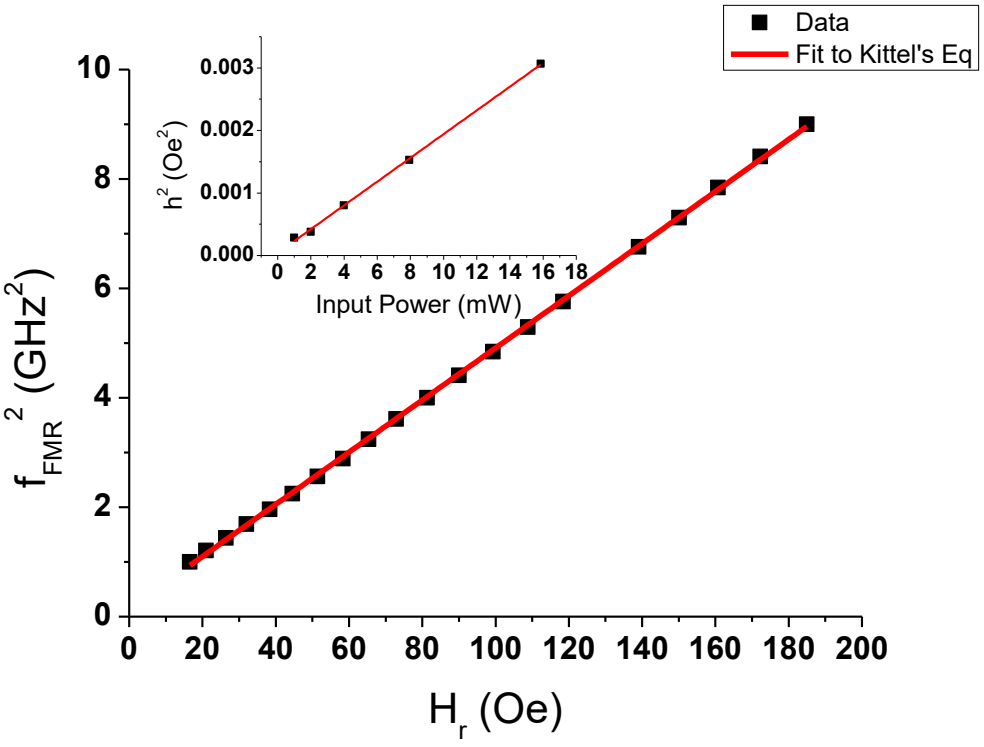

Figure 4.5 $f_{FMR}{}^2$ against H_r obtained from the measured voltage spectra, along with fitting to Kittel's formula. Inset shows the squared of the microwave field strength h^2 as a function of applied microwave power as determined by a VNA. Adapted with permission from Ref. [26].

With all known parameters as determined above and with $l = 7$mm and $\lambda_{Pt} = 10$nm [11,12], we calculate that $\theta_{SHE} = 0.007 \pm 0.002$ for the Pt film. This is close to the value of 0.0067 reported by Ref. [11], but much smaller than the value of 0.08 given by Ref. [24]. There are also some differences in the assumptions and parameters given in both studies: Ref. [11] considered only a dispersive lineshape for SRE, while Ref. [24] considered the mixing of both dispersive and lorentzian components; in Ref. [11], $\lambda_{Pt} = 3.7$nm but $\lambda_{Pt} = 10$nm in Ref.

[24]. Furthermore, the shunting effect of the bilayers was also not considered in both of the above studies. Since the current shunting effect is unlikely to result in such a large difference in θ_{SHE} between Ref. [24] and that found in our experiment, we suppose that other extrinsic factors may have contributed to the difference, caused by differing film quality and deposition conditions.

Recently, it has been found by Sanchez *et al*[31] that the spin galvanic effect (SGE)/inverse Rashba-Edelstein effect (IREE)[32], in which a charge current results from a spin current flowing across a 2-D interface with inversion asymmetry, can produce appreciable spin-to-charge conversion that has the same angular symmetry as ISHE. While no work has thus far been done in literature to investigate SGE/IREE at NiFe/Pt interfaces, the possibility of significant SGE/IREE in our NiFe/Pt system cannot be ruled out since Pt, being a heavy metal with strong spin-orbit coupling, satisfies the criteria for SGE/IREE. This may account for the relatively low θ_{SHE} found, as a negative SGE/IREE current may cancel the ISHE charge current produced leading to an underestimate of θ_{SHE}. However, due to the relatively thick Pt layer used (10 nm), we think that SGE/IREE should not be significant here.

4.5 Conclusion

In this chapter, we have presented a systematic and detailed method and analysis to address the issue of the separation of ISHE signals of interest from unwanted SRE voltages. Our analysis is based on in-plane configurations of applied static field, microwave field and current, which results in angular-separable voltages from SRE and ISHE. We also note the possibility of ac spin current detection via the rectification of the ac spin current pumped

from the Py layer. With a spin diffusion length of 10nm, the spin Hall angle for our Pt film is estimated to be $\theta_{SHE} = 0.007 \pm 0.002$.

4.6 References

1 M. I. Dyakonov and V. I. Perel, Physics Letters A **35,** 459 (1971).

2 J. E. Hirsch, Physical Review Letters **83,** 1834 (1999).

3 J. Sinova, D. Culcer, Q. Niu, N. Sinitsyn, T. Jungwirth, and A. MacDonald, Physical Review Letters **92**, 126603 (2004).

4 A. Fert, Reviews of Modern Physics **80,** 1517 (2008).

5 J. Wunderlich, B. Kaestner, J. Sinova, and T. Jungwirth, Physical Review Letters **94,** 047204 (2005).

6 E. Saitoh, M. Ueda, H. Miyajima, and G. Tatara, Applied Physics Letters **88,** 182509 (2006).

7 K. Ando, S. Takahashi, K. Harii, K. Sasage, J. Ieda, S. Maekawa, and E. Saitoh, Physical Review Letters **101,** 036601 (2008).

8 K. Ando, Y. Kajiwara, S. Takahashi, S. Maekawa, K. Takemoto, M. Takatsu, and E. Saitoh, Physical Review B **78,** 014413 (2008).

9 O. Mosendz, V. Vlaminck, J. E. Pearson, F. Y. Fradin, G. E. W. Bauer, S. D. Bader, and A. Hoffmann, Physical Review B **82,** 214403 (2010).

10 K. Ando and E. Saitoh, Journal of Applied Physics **108,** 113925 (2010).

11 O. Mosendz, J. E. Pearson, F. Y. Fradin, G. E. Bauer, S. D. Bader, and A. Hoffmann, Phys Rev Lett **104,** 046601 (2010).

[12] K. Ando, S. Takahashi, J. Ieda, Y. Kajiwara, H. Nakayama, T. Yoshino, K. Harii, Y. Fujikawa, M. Matsuo, S. Maekawa, and E. Saitoh, Journal of Applied Physics **109,** 103913 (2011).

[13] A. Fert and P. M. Levy, Physical Review Letters **106,** 157208 (2011).

[14] L. Liu, T. Moriyama, D. C. Ralph, and R. A. Buhrman, Physical Review Letters **106,** 036601 (2011).

[15] Y. Niimi, M. Morota, D. H. Wei, C. Deranlot, M. Basletic, A. Hamzic, A. Fert, and Y. Otani, Physical Review Letters **106,** 126601 (2011).

[16] Z. Feng, J. Hu, L. Sun, B. You, D. Wu, J. Du, W. Zhang, A. Hu, Y. Yang, D. M. Tang, B. S. Zhang, and H. F. Ding, Physical Review B **85,** 214423 (2012).

[17] L. Liu, C. F. Pai, Y. Li, H. W. Tseng, D. C. Ralph, and R. A. Buhrman, Science **336,** 555 (2012).

[18] L. Liu, O. J. Lee, T. J. Gudmundsen, D. C. Ralph, and R. A. Buhrman, Physical Review Letters **109,** 096602 (2012).

[19] H. Jiao and G. E. W. Bauer, Physical Review Letters **110,** 217602 (2013).

[20] B. F. Miao, S. Y. Huang, D. Qu, and C. L. Chien, Physical Review Letters **111,** 066602 (2013).

[21] J. C. Rojas-Sánchez, M. Cubukcu, A. Jain, C. Vergnaud, C. Portemont, C. Ducruet, A. Barski, A. Marty, L. Vila, J. P. Attané, E. Augendre, G. Desfonds, S. Gambarelli, H. Jaffrès, J. M. George, and M. Jamet, Physical Review B **88,** 064403 (2013).

[22] T. Tanaka, H. Kontani, M. Naito, T. Naito, D. S. Hirashima, K. Yamada, and J. Inoue, Physical Review B **77,** 165117 (2008).

[23] H. Nakayama, K. Ando, K. Harii, T. Yoshino, R. Takahashi, Y. Kajiwara, K. Uchida, Y. Fujikawa, and E. Saitoh, Physical Review B **85,** 144408 (2012).

[24] A. Azevedo, L. H. Vilela-Leão, R. L. Rodríguez-Suárez, A. F. Lacerda Santos, and S. M. Rezende, Physical Review B **83,** 144402 (2011).

[25] L. Bai, P. Hyde, Y. S. Gui, C. M. Hu, V. Vlaminck, J. E. Pearson, S. D. Bader, and A. Hoffmann, Physical Review Letters **111,** 217602 (2013).

[26] W. T. Soh, B. Peng, and C. K. Ong, Journal of Physics D: Applied Physics **47,** 285001 (2014).

[27] Y. Tserkovnyak, A. Brataas, and G. Bauer, Physical Review B **66,** 224403 (2002).

[28] Y. Tserkovnyak, A. Brataas, and G. Bauer, Physical Review Letters **88,** 117601 (2002).

[29] C. Hahn, G. de Loubens, M. Viret, O. Klein, V. V. Naletov, and J. Ben Youssef, Physical Review Letters **111,** 217204 (2013).

[30] D. Wei, M. Obstbaum, M. Ribow, C. H. Back, and G. Woltersdorf, Nat Commun **5,** 3768 (2014).

[31] J.C. Rojas Sanchez, L. Vila, G. Desfonds, S. Gambarelli, J.P. Attane, J.M. De Teresa, C. Magen and A. Fert, Nat Commun **4,** 2944 (2014).

[32] Jairo Sinova, Sergio O. Valenzuela, J. Wunderlich, C. H. Back, and T. Jungwirth, Rev. Mod. Phys. 87, 1213 (2015).

5 Localized excitation of magnetostatic surface spin waves in yttrium iron garnet via spin pumping and rectification effect

5.1 Introduction

Spin waves (or magnons)[1], whether dominated by magnetostatic dipolar or exchange interactions, play an important role in the field of spintronics since its propagation carries spin angular momentum without necessarily being accompanied by a charge current, thus equivalent to a pure spin current[2,3]. While conventional spin currents carried by mobile, spin-polarised charge carriers are susceptible to rapid dissipation through scattering via spin-orbit interactions leading to typical length scales of only hundreds of nanometres[4] in metals and semiconductors, spin wave propagation via magnetostatic and exchange interactions between localized spins are immune to these scattering processes and is mainly dependent on spin wave damping, which for a low loss magnetic insulator such as YIG, the propagation length scales can be up to few centimetres[5]. This means that spin wave spin currents can propagate over macroscopic distances and is therefore ideally suited as long-range carriers in spin circuits.

In context to generation of spin currents via spin pumping at FM/NM interfaces, it has been found that the nature of spin precession can significantly influence the spin pumping efficiency. Because spin pumping is mediated by interfacial exchange interaction, the localization of surface spin waves at the FM interface can lead to much enhanced spin pumping efficiencies[6,7] as compared to other volume precession modes. Thus the combination of spin pumping and inverse spin Hall effect (ISHE), as mentioned in the previous chapter, can be an efficient way to selectively study magnetostatic surface spin

waves (MSSWs). Such experiments have been reported[8,9] recently, where the direct observation of non-reciprocity in spin wave propagation was demonstrated. Conversely, these MSSWs can also be manipulated[10-13] by a reverse mechanism to inject a spin current into the magnetic layer to produce a magnetic spin transfer torque (STT) on the MSSW. In addition to magnetostatic spin waves, spin pumping by short-wavelength exchange magnons[14,15] have also been found to be significant. These developments clearly highlight the potential of spin waves in producing novel magnon-based spintronic circuits.

In most experiments, the microwave fields permeating the sample is approximately uniform as the sample size relative to the cavity or waveguide where is its placed within is usually small. In such cases, the FMR uniform mode is preferentially excited. In order to excite spin waves efficiently, non-uniformity in the microwave magnetic field is required, which is usually achieved by increasing the sample size relative to the waveguide/cavity geometry. An alternative, and more attractive method, is to make use of a near-field rf probe[16] whose end is placed near the surface of the sample where the rf fields terminate. Depending on the geometry of the excitation field produced by the probe's end, various magnetostatic spin wave modes can be locally excited and subsequently detected via a network analyzer. Since the rf fields at the probe's end are non-propagating, both near-field and far-field components exist, in which the amplitude of the former typically decays exponentially with distance. This results in an exponentially varying rf field whose geometry would be ideal for exciting surface spin waves. In contrast, this near-field component is absent for samples placed with waveguides/cavities where fields are propagating. Another important characteristic of such local probes lies in its compatibility with scanning techniques, thus allowing microwave imaging.

To be compatible with spintronics where electrical detection is required, we extend this technique by designing and fabricating a near-field shorted coaxial probe with spring-loaded dc electrical probes at its measuring end to allow the simultaneous localized microwave excitation and electrical detection. In this chapter, we shall detail how such a shorted coaxial probe is made and demonstrate its use to locally excite and electrically detect the FMR and spin wave modes of bulk YIG substrate patterned with Pt and Py films. A similar probe for near-field FMR detection of magnetic films has also been previously developed[17] in our lab.

5.2 Fabrication and simulation of the shorted coaxial probe

In this section, we detail our considerations for the design and fabrication of our shorted coaxial probe for the electrical detection of spin modes, with the help of finite-element simulations to optimise our design. The coaxial transmission line is chosen for our purpose as its cylindrical structure is ideal for compact scanning probes. At one end of the coaxial line, we short the centre conductor with the outer conductor (ground), which can be done using a gold wire bond, with the purpose to direct the microwave magnetic fields to curl around the wire bond. Thus, the directed microwave fields can be used to controllably excite spin precession.

Since the microwave reflected at the shorted end of the coaxial line can interfere with the incoming waves to form standing waves, the shorted coaxial probe can also act as a resonator under non-ideal conditions. Thus, as an initial consideration, the intrinsic resonance frequencies of the probe must not fall within the frequency range of interest so as not to complicate the measured signals. To this end, the length of the probe L becomes important

since it directly affects its resonance frequencies. The probe is modelled as a transmission line (Figure 5.1) with impedance Z_0, connected to a microwave source of impedance $Z_2 = 50\ \Omega$ and a short of impedance $Z_1 = 0$ at their respective ends. Ideally, the impedance of the probe Z_0 would be 50 Ω, in which case no reflection of waves will occur at the Z_0 / Z_2 boundary so that no standing waves can be formed within the probe and therefore resonances do not occur. This situation does not occur in reality due to connector influences, among other factors such as line imperfections. As such, practically, Z_0 always differ slightly from 50 Ω such that the Z_1 / Z_0 and Z_0 / Z_2 boundaries differ and allow standing waves to form within the probe.

If $Z_0 > Z_2$, then half-wavelength resonances will occur at $f_n^{1/2}$, where

$$f_n^{1/2} = \frac{nc}{2L\sqrt{\varepsilon}}, n = 1, 2, 3... \qquad (5.1)$$

Here, *c* is the speed of light in vacuum, *L* is the line length and ε is the dielectric constant of the filling material. If $Z_0 < Z_2$, then quarter-wavelength resonances will occur at $f_n^{1/4}$, where

$$f_n^{1/4} = \frac{nc}{4L\sqrt{\varepsilon}}, n = 1, 2, 3... \qquad (5.2)$$

Figure 5.1 Schematic diagram of the shorted coaxial transmission line (cross-section) of characteristic impedance Z_0, with one end shorted $Z_1=0\,\Omega$ and the other end terminated with a microwave source $Z_2=50\,\Omega$.

In our case, we require that the working frequency of the probe to be at least up to 10 GHz. This means that the first order resonances (n=1) must ideally fall above 10 GHz, i.e. $\min\left[f_1^{1/2}, f_1^{1/4} \right] = f_1^{1/4} > 10$ GHz. Using $\varepsilon = 2.1$ (Teflon) as the filling material, we can calculate that L should be at most 5.1 mm. We choose the length of our fabricated probe as 3 mm, thus fulfilling this criterion.

In order to simulate the microwave field distribution produced by the probe, we use finite-element method via HFSS to model our probe. The frequency characteristics of the reflection S-parameter S_{11} is shown in Figure 5.2, where we see that the microwave is mostly reflected with slightly increased losses as the frequency increases to 10 GHz. No obvious resonance peaks are seen, thus indicating good impedance matching. Figure 5.3 below shows the microwave magnetic field distribution produced by the probe at the shorted end. As expected, a microwave current flowing along the short produces a magnetic field that predominantly curls around the short, with amplitudes ranging from 0-0.119 Oe at 18 dBm (0.063W) applied power.

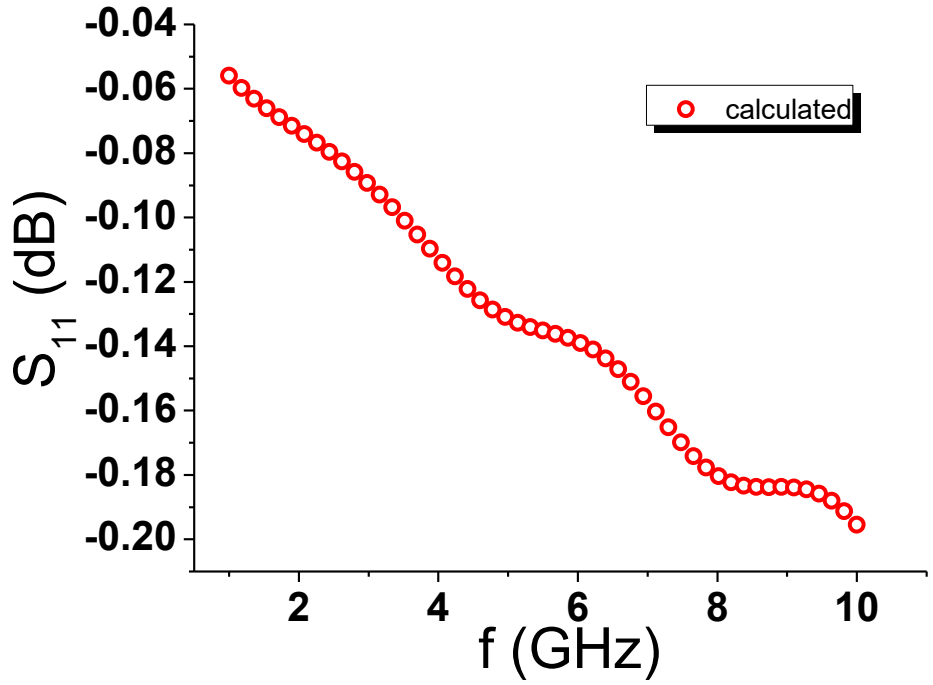

Figure 5.2 Reflection coefficient $S_{11}(\mathrm{dB})$ as a function of frequency as obtained from simulation results for the shorted coaxial probe.

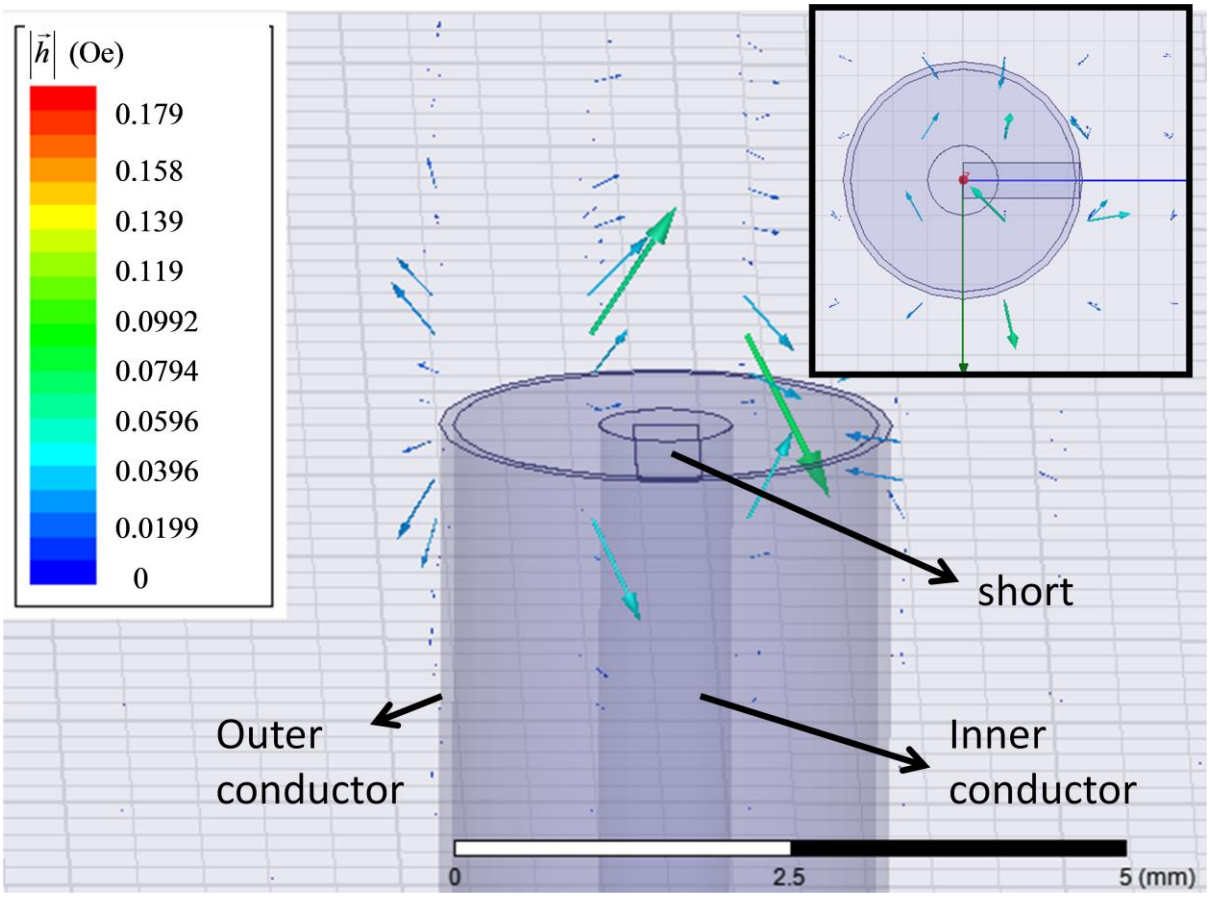

Figure 5.3 Model of shorted coaxial probe at the shorted end, showing the microwave magnetic field strength and direction near the short.

The microwave magnetic field can be used as the excitation field onto a magnetic conducting sample, inducing both spin dynamics as well as a microwave current within the sample. This microwave current then rectifies with the oscillating magneto-resistance to produce a dc signal which can be measured in the vicinity of the probe. Spring-loaded needle probes are attached to the sides of the probe to facilitate this dc measurement. In Figure 5.4, we plot, at 3 GHz, the distribution of the microwave magnetic field *h* generated by the probe within a Pt film strip, showing that the field is quite inhomogeneous along the strip and that the dominant net non-zero contribution lies along the strip direction. We also show in Figure 5.5 the corresponding current density $\vec{j}$ within the Pt film. We see that while the net non-

zero contribution of $\vec{j}$ lies along the wire bond direction (perpendicular to the Pt strip direction), a significant component of $\vec{j}$ lies along the strip direction, though the magnitude of the latter will largely cancel out due to their opposing directions of flow.

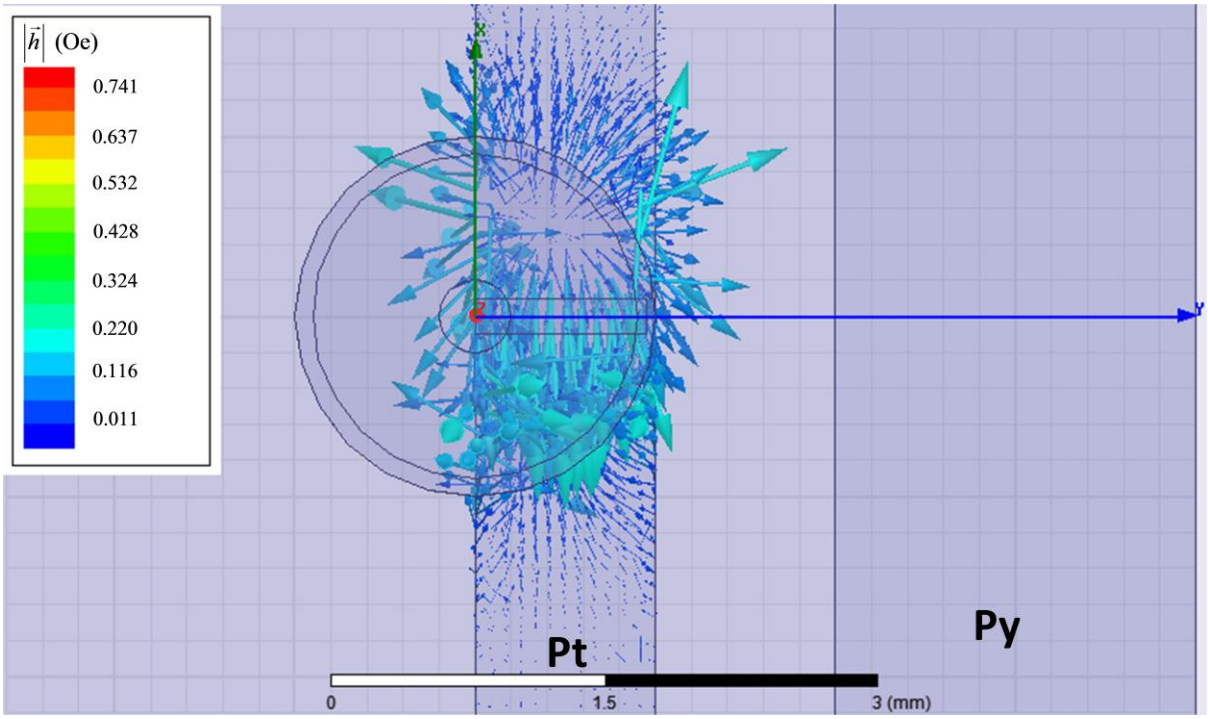

Figure 5.4 The distribution of the microwave magnetic field at 3GHz incident onto the Pt film placed 0.7mm away from the shorted end of the probe.

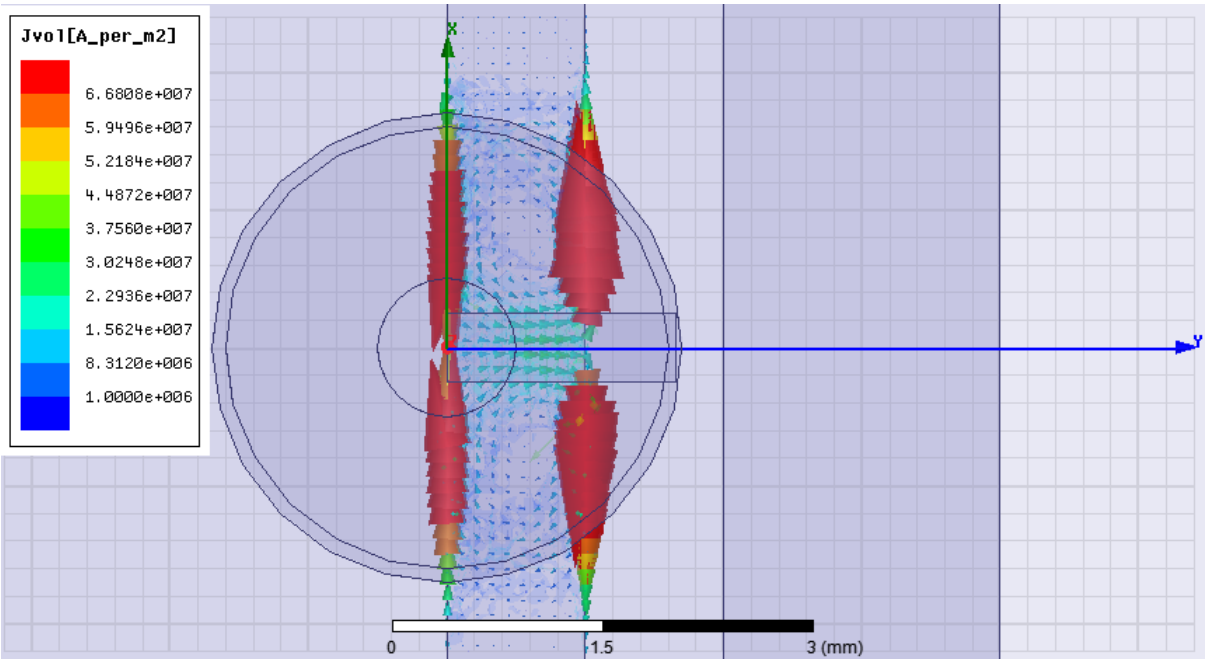

Figure 5.5 The current density distribution within the Pt film volume at 3GHz, where the film is placed 0.7mm away from the shorted end of the probe.

The shorted coaxial probe is finally fabricated by modifying a non-magnetic coaxial line of 50 Ω impedance (outer and inner conductors of diameter 3.5 mm and 1 mm respectively). One end of the coaxial line is welded to a SMA connector which is meant to be connected to a microwave source port, while the other end is polished and subsequently shorted with a gold wire bond connecting the inner and outer conductors. (Figure 5.6) While the microwave field produced by this probe at the shorted end is expected to be highly inhomogeneous, a dominant contribution will exist near the shorted silver bond due to its geometry that will be used to excite magnetisation dynamics. DC spring-loaded needle probes are attached to (but electrically shielded from) the outer conductor to simultaneously detect electrical signals.

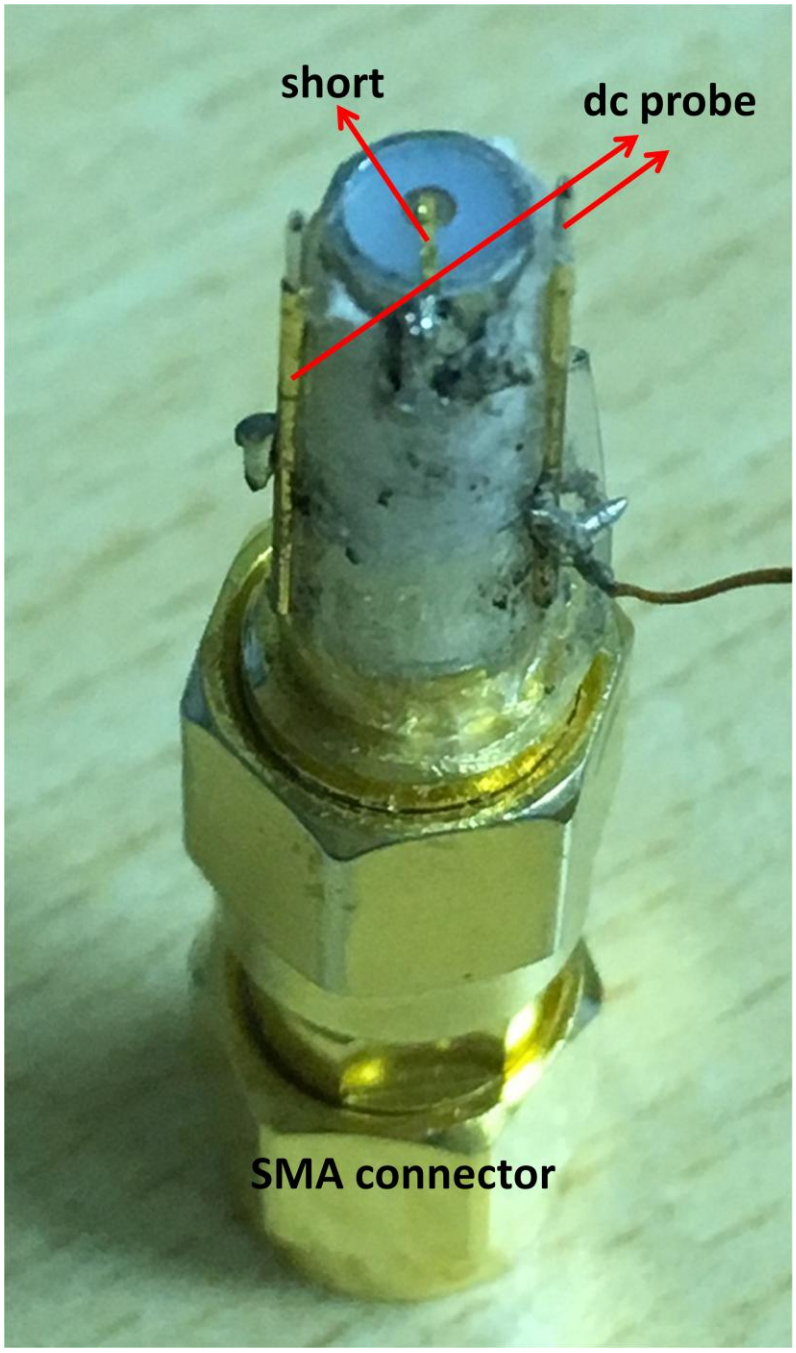

Figure 5.6 Picture of the shorted coaxial probe used in our experiment.

5.3 Experimental Setup

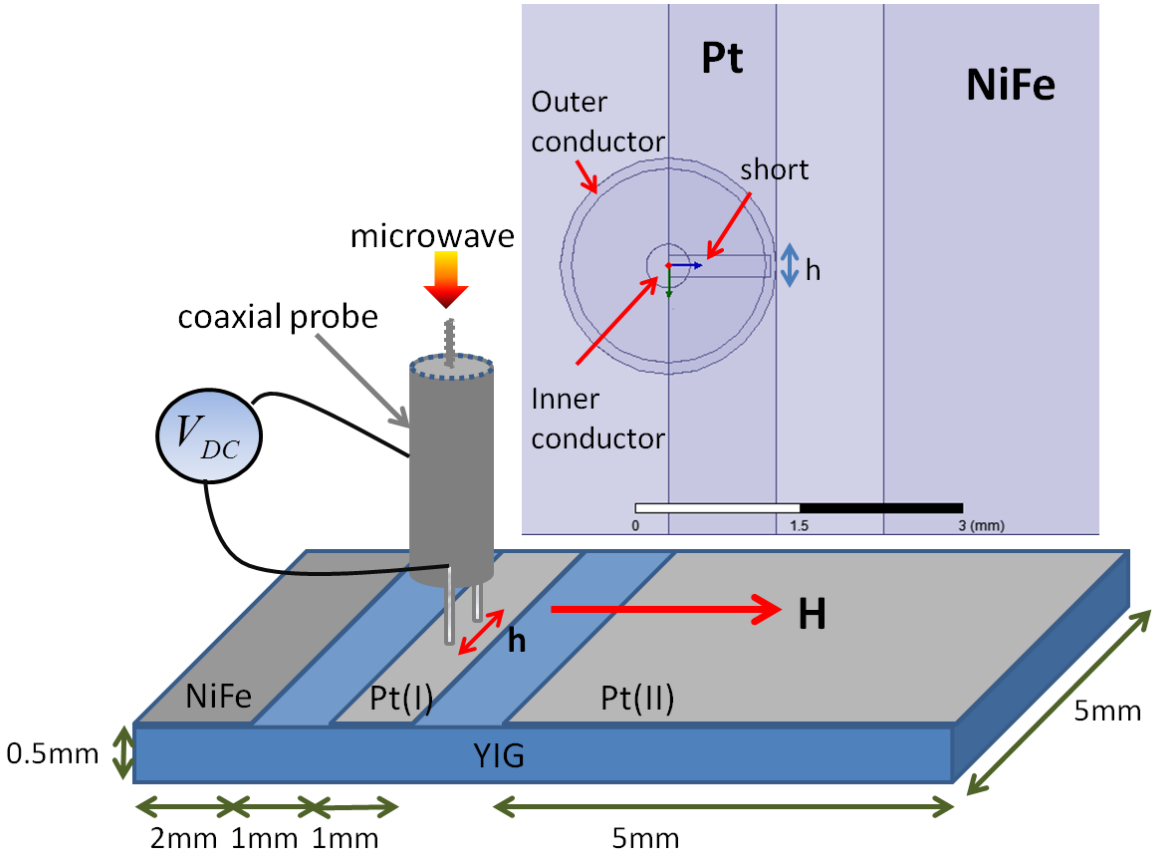

Figure 5.7 Schematic diagram for the sample and measurement configurations, whereby the probe is directly exciting and measuring the Pt(I) region. The inset shows the top view of the setup. *h* is the dominant microwave magnetic field produced by the probe. Adapted with permission from Ref. [18].

Via rf magnetron sputtering at room temperature and $< 6\times10^{-7}$ Torr base chamber pressure, we fabricated patterned Py (20 nm thick) and Pt (10 nm thick) films onto a common bulk yttrium iron garnet (YIG) substrate of dimensions 10 mm (length) by 5 mm (width) by 0.5 mm (thickness). (Figure 5.7) The shorted coaxial probe, whose dimensions are comparable to the patterned film, is then placed above the region of interest (eg. Pt (I) region in Figure 5.7) such that the distance between the film and the short is about 0.5 mm. This probe-to-sample distance can be reliably controlled so that the derived signal level can be varied accordingly. The spring-loaded probes are then in direct electrical contact with the

conducting film surface. The probe is connected to a microwave signal generator and the dc voltages under microwave excitation at 18 dBm power are then measured via a lock-in amplifier at 10 kHz amplitude modulation. An in-plane magnetic field is also applied by an electromagnet.

The spatial scanning resolution of our probe is of the order of millimetres, limited by its coaxial diameter and wire bond dimensions. This can be scaled down by decreasing the probe diameter, while still ensuring impedance matching, as well as by reducing the wire bond's width. For instance, the latter can be achieved[19] via lithographic techniques to pattern the wire bond after deposition.

5.4 Theory

Driven by the microwave field produced by the coaxial probe at the shorted end, and aided by the low magnetic damping in YIG (only of order of 0.001, compared to 0.01 for most metallic FM films), spin waves are easily excited locally and propagates throughout the sample dimensions and forming standing waves upon reflections at boundaries. We only consider long-wavelength dipolar spin waves here, since their wavelengths are comparable to our probe dimensions and hence are readily excited, compared to short-wavelength exchange dominated spin waves. The exchange spin waves are usually excited indirectly via nonlinear magnetisation dynamics such as parametric excitation.[14,15,20]

Two types of long-wavelength dipolar spin waves can be excited in our setup: magnetostatic backward volume spin waves (MSBVSW) and magnetostatic surface spin waves (MSSW). MSBVSW are volume spin waves whose in-plane wave vector k is parallel to the magnetisation M and hence, the applied field H since M is saturated along H. On the

other hand, MSSW are surface spin waves whose precession amplitude decays exponentially with depth, with an in-plane wave vector that is perpendicular to *H*. Due to its surface character, the localization of MSSWs at the spin pumping interface of a FM/NM can lead to an enhanced ISHE signal due to spin pumping, which offers a unique way to selectively characterise them.

At spin resonance, the precession of the dynamic magnetisation $\vec{m}$ injects a spin current $\vec{j}_s \propto \vec{m} \times d\vec{m}/dt$ from YIG into Pt via spin pumping, where the ISHE converts the spin current into a rectified dc charge current $\vec{j}_c \propto \theta_{SHE} \hat{n} \times \vec{j}_s$. θ_{SHE} is the spin Hall angle quantifying the efficiency and $\hat{n}$ is the out-of-plane unit vector. In our measurement configuration, the in-plane static applied field H is perpendicular to both the microwave magnetic field $\vec{h}$ and dc measurement direction. The subsequently detected dc ISHE voltage is thus a maximum under such a configuration. Any detected MSSWs would have a wave vector parallel to the dc measurement direction along the shorter length (5 mm) of the sample. Standing MSSWs along this length with wave vector $k = n\pi/(5\text{ mm})$ can be formed, whereby n is an integer. The spin wave resonance field H_r for MSSWs at each microwave frequency *f* can be described by[1,21]

$$H_r = \sqrt{\left(\frac{2\pi f}{\gamma}\right)^2 - (2\pi M)^2\left(1 - e^{-2kd}\right) - 4\pi M H_k + \left(\frac{4\pi M + H_k}{2}\right)^2} - \frac{4\pi M + H_k}{2}, \qquad (5.3)$$

where γ is the gyromagnetic ratio, M is the saturation magnetisation, $H_k \approx 0$ is the anisotropy and d is the effective YIG thickness transversed by MSSWs.

For MSBVSW s, the wave vector *k* is parallel to *M*, hence standing MSBVSW s can be formed along the longer end of the sample. However, it is unlikely that the propagation

length can extend throughout the 10mm length of the sample due to spin wave decay. The actual propagation length is likely to be much shorter ~5mm, as comparable to the diameter of the probe excitation region. The dispersion relation for MSBVSW s is described by

$$H_r = \sqrt{\left(\frac{2\pi f}{\gamma}\right)^2 - 4\pi M H_k\left(\frac{1-e^{-2kd}}{kd}\right) + \left(\frac{4\pi M\left(1-e^{-2kd}\right)/kd + H_k}{2}\right)^2} - \frac{4\pi M\left(1-e^{-2kd}\right)/kd + H_k}{2}. \quad (5.4)$$

For the YIG/NiFe region, the microwave excitation can also lead to SRE signals in addition to spin pumping induced ISHE voltages within the NiFe layer. As we know from previous chapters, this SRE dc voltage comes from AMR and AHE within the NiFe layer only. Since SRE only occurs near NiFe resonance and ISHE occurs at YIG resonance, they can be reliably separated from each other by identifying the nature of the resonance peaks in the voltage spectra via a frequency sweep analysis to extract the value of saturation magnetisation.

5.5 Results and discussions

5.5.1 Local measurements on Pt(I)/YIG

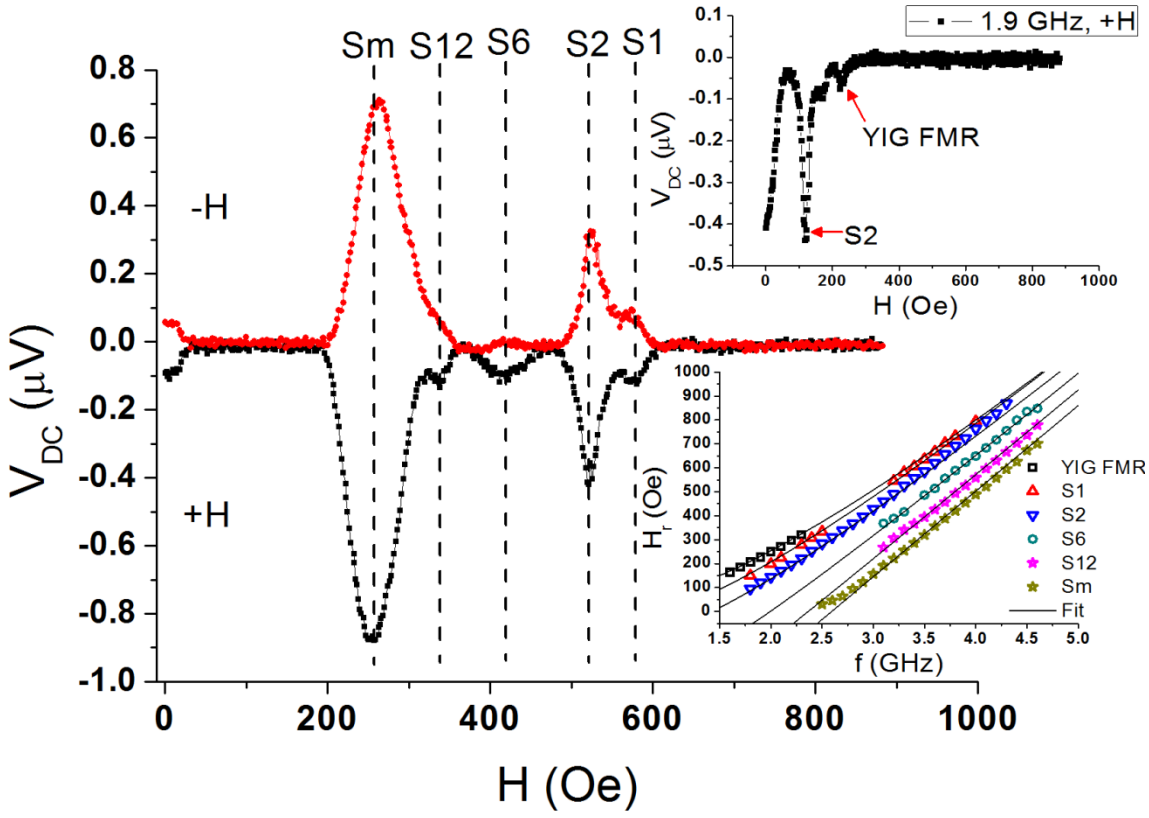

Figure 5.8 At 3.3 GHz, the measured V_{DC} spectra when the Pt(I) region is locally excited by the probe, along opposing $+H$ and $-H$ directions. Top inset: V_{DC} spectra at 1.9 GHz to highlight peak due to the YIG FMR uniform mode. Bottom inset: The corresponding frequency variation of the H_r of various modes along $+H$. Adapted with permission from Ref. [18].

With the shorted coaxial probe directly above the Pt(I) region and centralized, we measure the dc voltages V_{DC} generated under local microwave excitation. We show in Figure 5.8 the V_{DC} spectra at 3.3 GHz measured along both the $+H$ and $-H$ directions. In the inset, the voltage peaks that appear to the left of the FMR mode at lower field are MSSWs, since its H_r decreases with increasing k as can be seen from equation (5.3). We can clearly see five voltage peaks (labelled S1, S2, S6, S12 and Sm) at 3.3 GHz. The number in the labels represents the fitted MSSW mode number n in equation (5.3). Interestingly, d is fitted to be

~0.02cm rather than 0.05cm, the latter being the thickness of the YIG slab. We attribute this to the significant depth variation of the microwave field strength *h*. (Figure 5.9) We find that the YIG FMR uniform mode is much weaker than the other modes and cannot be clearly distinguished at 3.3 GHz. In fact, across the measured frequency range from 1-5 GHz, the FMR mode is observed to be consistently weaker than the MSSW modes. This highlights the enhanced spin pumping contribution from MSSWs relative to the other modes.

The mode Sm, which appears to be much stronger than the other modes, can be seen across a large frequency range. We found that this mode corresponds to a wave number k>100 cm^{-1}, above which the MSSW frequency saturates for higher k. Thus, the Sm mode results from the superposition of various $k > 100$ cm^{-1} MSSW modes, explaining its enhanced ISHE signal and much larger linewidth. Increasing the sweeping microwave frequency up to 5 GHz do not result in any more peaks appearing to the left of the Sm mode in the voltage spectra, which is consistent with this explanation. Finally, the non-zero dc voltage near H=0 is due to the magnetisation rotation in unsaturated YIG with changing field.

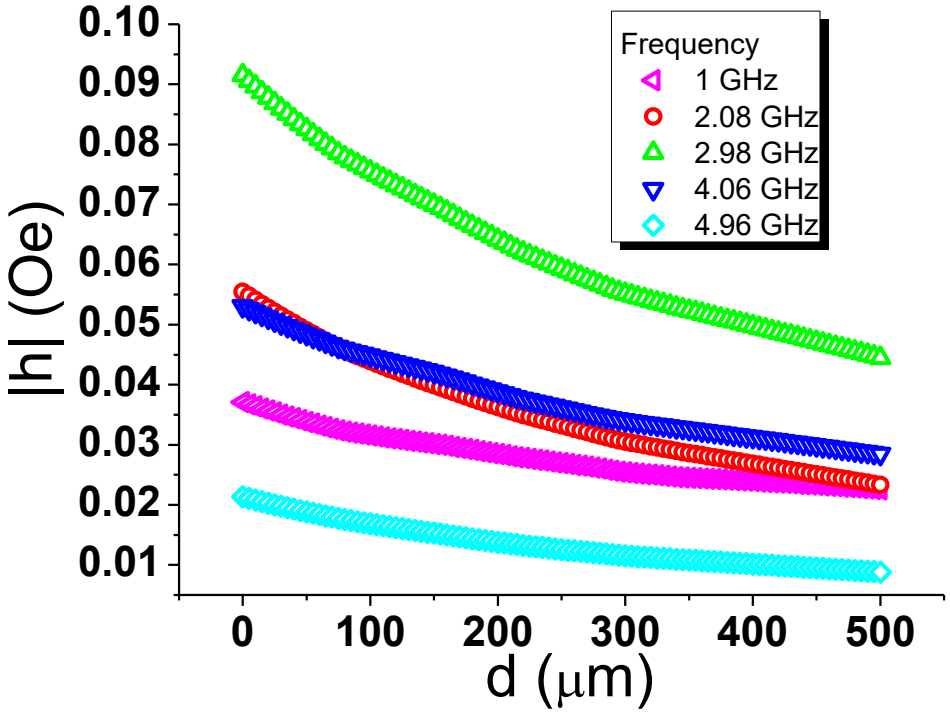

Figure 5.9 The microwave field *h* strength at various frequencies at the centre of the Pt(I) region as a function of YIG substrate depth *d*, obtained via simulation.

5.5.2 Local measurements on Pt(II)/YIG

Next, the shorted coaxial probe is placed above the Pt(II) region to locally excite spin precession. While the Pt thickness is the same, the Pt(II) region measures 5mm by 5mm and has a much larger area than the Pt(I) region measured earlier. Figure 5.10 shows the V_{DC} spectra measured at 3 GHz for this region along $+H$ and $-H$. Like the Pt(I) region, the FMR uniform mode observed for the Pt(II) region is also consistently weaker than the MSSW modes (P3 and Pm). Also, the Pm mode which consists of the sum of saturated-frequency $k > 100$ cm^{-1} MSSW modes is much larger than the other modes. Overall, the magnitude of V_{DC} for all the observed modes is significantly lower than that from the Pt(I) region. We attribute this to the shunting of part of the signal by the surrounding conducting Pt film below which MSSWs were not present. The absence of certain modes from the Pt(I) region is also

evident here, which is likely due to the differing excitation conditions as a result of differing placement of the probe and geometries of the regions. These results demonstrate that a continuous conducting film can also be measured via this technique, which is potentially useful for electrical dc microwave imaging.

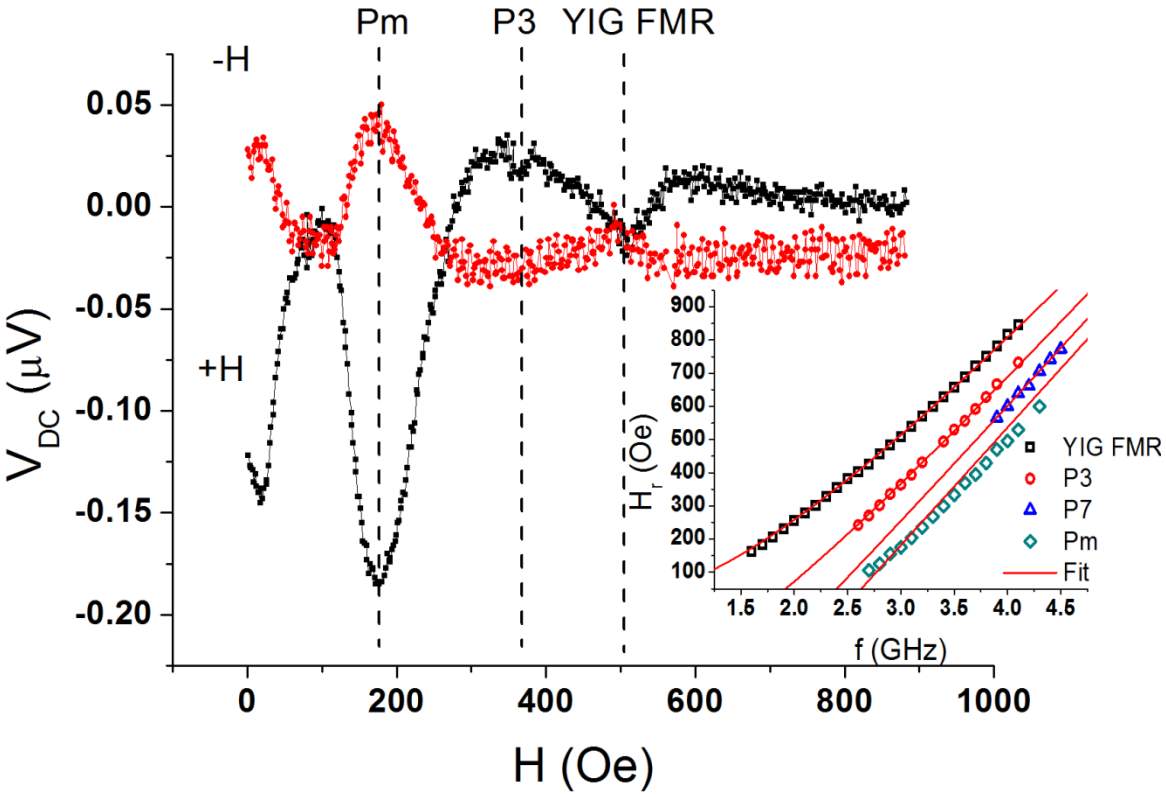

Figure 5.10 The measured V_{DC} spectra in the Pt(II) region under local microwave excitation at 3 GHz, along $+H$ and $-H$ directions. The inset shows the corresponding frequency variation of H_r for the various fitted modes. Adapted with permission from Ref. [18].

5.5.3 Local measurements on Py/YIG

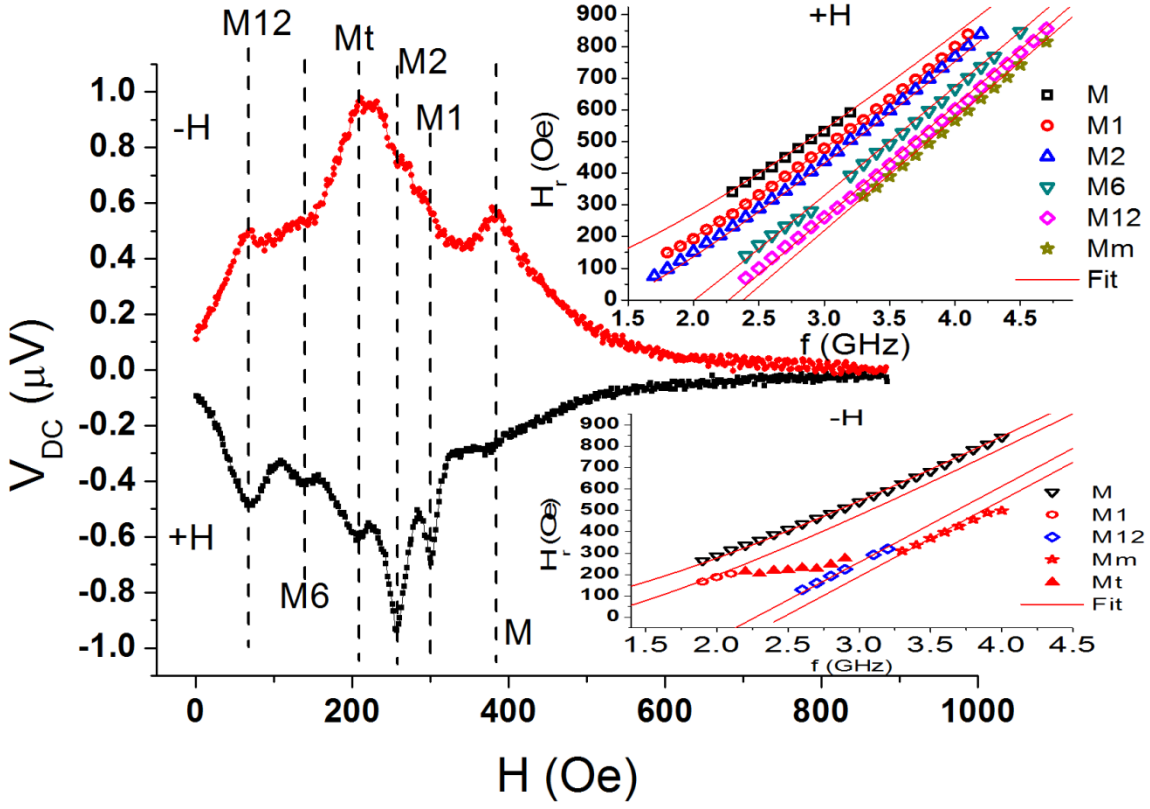

Figure 5.11 The measured V_{DC} spectra under local excitation of the NiFe region at 2.4 GHz along $+H$ and $-H$ directions. The inset shows the corresponding frequency variation of H_r for the various fitted modes. Adapted with permission from Ref. [18].

Following, the same measurement is performed with the probe exciting the NiFe region, with the resulting V_{DC} spectra shown in Figure 5.11. A large number of modes can be observed across the frequency range from 1.5-4.5 GHz. Mode M, identified as the YIG FMR uniform mode, can be fitted to the Kittel's equation $f = (\gamma / 2\pi)\sqrt{H(H + 4\pi M)}$ with $4\pi M \approx 1600$ G, close to the saturation magnetisation 1750 G of bulk YIG. The slight discrepancy may be due to the FMR field shift resulting from the exchange coupling of YIG/NiFe. The observation of this mode, as well as the subsequent YIG MSSWs, indicates the detection of ISHE in NiFe via spin pumping from YIG. The modes M1, M2, M6 and M12 are fitted to be the corresponding MSSW modes of YIG with $d \cong 0.02$ cm and

$4\pi M \approx 1650$ G, while the Mm mode contributes a large voltage signal and corresponds to the saturation wave vector $k > 90$ cm^{-1}. The mode Mt cannot be clearly identified and is likely to be a 'false peak' due to the overlapping of finite-linewidth MSSW modes between M1 and M12, as its dispersion curve appears to cut across M1 to M12. The SRE voltage from the NiFe layer could also have resulted in the appearance of mode Mt, although this could not be clearly resolved and fitted from the spectra due to mixing with other modes. Furthermore, we know that SRE contributes both dispersive and lorentzian lineshapes in the spectra, while ISHE is only lorentzian. As the observed modes are mainly lorentzian with a dispersion associated with M~1650 G which is nowhere near the saturation magnetisation of NiFe (~10kOe), it is likely that the SRE contribution is small or overshadowed by the various observed MSSW modes.

Across all regions, the observed MSSW modes (both in terms of signal magnitude and number) at fixed excitation frequency are not symmetric with respect to H reversal. This is likely the result of the non-reciprocity[8,9] of MSSW whereby the wave vector changes direction upon H reversal. Since the electrical probes are not exactly centralized with respect to the sample short length during measurement, the opposing propagation of MSSWs upon H reversal are hence not exactly symmetric, which could result in the altered voltage spectra upon H reversal.

5.6 Conclusion

The discussion and results in this chapter demonstrates that our shorted coaxial probe technique can be used to locally excite and electrically detect spin dynamics reliably, which is potentially of interest for microwave imaging via electrical methods. In particular, we

detect the dc electrical signals stemming from FMR and MSSW modes mainly via spin pumping and rectification from patterned/continuous NiFe and Pt films onto common YIG substrates. The dc signal levels from MSSW modes is significantly higher than that from FMR uniform mode, which we attribute to be the result of enhanced spin pumping from these surface modes. Such MSSW modes are also likely to be strongly excited by the probe due to the depth variation of the excitation microwave field. Furthermore, we also observe ISHE within the NiFe layer due to the presence of modes in the measured voltage spectra which were of YIG character.

5.7 References

[1] A. A. Serga, A. V. Chumak, and B. Hillebrands, Journal of Physics D: Applied Physics **43,** 264002 (2010).

[2] H. Kurebayashi, O. Dzyapko, V. E. Demidov, D. Fang, A. J. Ferguson, and S. O. Demokritov, Nat Mater **10,** 660 (2011).

[3] S. M. Rezende, R. L. Rodríguez-Suárez, R. O. Cunha, A. R. Rodrigues, F. L. A. Machado, G. A. Fonseca Guerra, J. C. Lopez Ortiz, and A. Azevedo, Physical Review B **89,** 014416 (2014).

[4] J. Bass and W. P. Pratt, Journal of Physics: Condensed Matter **19,** 183201 (2007).

[5] Y. Kajiwara, K. Harii, S. Takahashi, J. Ohe, K. Uchida, M. Mizuguchi, H. Umezawa, H. Kawai, K. Ando, K. Takanashi, S. Maekawa, and E. Saitoh, Nature **464,** 262 (2010).

[6] C. W. Sandweg, Y. Kajiwara, K. Ando, E. Saitoh, and B. Hillebrands, Applied Physics Letters **97,** 252504 (2010).

[7] S. S. Mukherjee, P. Deorani, J. H. Kwon, and H. Yang, Physical Review B **85,** 094416 (2012).

[8] R. Iguchi, K. Ando, Z. Qiu, T. An, E. Saitoh, and T. Sato, Applied Physics Letters **102,** 022406 (2013).

[9] L. H. Vilela-Leão, C. Salvador, A. Azevedo, and S. M. Rezende, Applied Physics Letters **99,** 102505 (2011).

[10] E. Padrón-Hernández, A. Azevedo, and S. M. Rezende, Applied Physics Letters **99,** 192511 (2011).

[11] J. Xiao and G. E. Bauer, Physical Review Letters **108,** 217204 (2012).

[12] Y. Zhou, H. Jiao, Y.-t. Chen, G. E. W. Bauer, and J. Xiao, Physical Review B **88,** 184403 (2013).

[13] G. L. da Silva, L. H. Vilela-Leão, S. M. Rezende, and A. Azevedo, Applied Physics Letters **102,** 012401 (2013).

[14] C. W. Sandweg, Y. Kajiwara, A. V. Chumak, A. A. Serga, V. I. Vasyuchka, M. B. Jungfleisch, E. Saitoh, and B. Hillebrands, Physical Review Letters **106,** 216601 (2011).

[15] H. Kurebayashi, O. Dzyapko, V. E. Demidov, D. Fang, A. J. Ferguson, and S. O. Demokritov, Applied Physics Letters **99,** 162502 (2011).

[16] E. Papa, S. E. Barnes, and J. P. Ansermet, Magnetics, IEEE Transactions on **49,** 1055 (2013).

[17] T. Hung le, N. N. Phuoc, X. C. Wang, and C. K. Ong, Review of Scientific Instruments **82,** 084701 (2011).

[18] W. T. Soh, B. Peng, and C. K. Ong, Journal of Applied Physics **117,** 153903 (2015).

[19] D. I. Mircea and T. W. Clinton, Applied Physics Letters **90,** 142504 (2007).

[20] K. Ando and E. Saitoh, Physical Review Letters **109,** 026602 (2012).

[21] R. W. Damon and J. R. Eshbach, Journal of Physics and Chemistry of Solids **19,** 308 (1961).

6 Long-range electrical detection of magnetisation dynamics via dipolar fields in YIG/SiO_2/NiFe trilayers

6.1 Introduction

The magnetic dipolar interaction is a fairly long-range (but weak) interaction that is responsible for demagnetizing fields and domains in ferromagnets. Between two neighboring magnetic moments μ_1 and μ_2, the magnetic dipolar interaction has a characteristic energy $E_{dip} \sim \frac{\mu_1 \mu_2}{4\pi r^3}$, where r is the distance between moments. For typical atomic length scales $r \sim 10^{-10}$ m and $\mu_1 \approx \mu_2 = \mu_B$, where μ_B is the Bohr magneton, $E_{dip} \sim 10^{-23}$ J is only of the order of a few Kelvins. Thus, almost all room-temperature magnetic phenomena resulting from interacting magnetic moments, ferromagnetism included, are dominated by the exchange interaction. In particular, the magnetic interaction between each layer in a FM/FM film bilayer system is usually modeled by considering only exchange interaction. In spintronics, spin current phenomena such as spin pumping and spin torque transfer is similarly mediated by the exchange interaction only.

Studies of such FM/FM bilayers are of importance particularly in data storage applications where they are extensively used as multilayers of alternating hard and soft ferromagnets. In similar context, nano-patterned multilayered magnetic structures have also generated great interest, notably in novel spin-torque oscillators[1,2] (STOs). In these structures, magnetic dipolar interaction can play a significantly role in addition to exchange interaction between layers to generate rich magnetisation dynamics. The static dipolar field produced by such nanostructures are often used as a convenient way to shift working frequencies[3] of modes in magnonics devices, or in general to systematically shift the static magnetic state,

much to the same effect as applying an external static magnetic field. The dynamic dipolar field usually serves to hybridise the magnetic modes in the uncoupled system, and thus defines the wave propagation characteristics[4] of nanostructures such as magnonic crystals.

However, such dynamic dipolar fields have yet been well-characterised in part due to difficulty in distinguishing signals from each coupled layer in the nanostructure. In addition, the static dipolar field produced by nanostructures scales as $1/r^3$, and hence is only perceivable at scales comparable to these structures, while conventional time-averaged measurements cannot detect dynamic dipolar fields, the latter usually being even smaller in magnitude as compared to its static counterpart. Recently, it has been demonstrated[5] that phase-sensitive Kerr microscopy can be employed to isolate the dynamic from the static dipolar interactions for a pair of nano-disks. Ferromagnetic resonance force microscopy techniques have also been used[6] to measure the dynamic dipolar coupling for a nano-disk pair. Alternatively, as we shall show in this chapter, electrical detection of FMR can also prove to be quite useful in resolving magnetisation dynamics within each layer in a system of interacting FM layers, owing to the possibility of isolating current flow within each layer.

This chapter focuses on the magnetisation dynamics in insulator FM/metallic FM systems (ie. YIG/NiFe) as detected by current-based microwave techniques via spin rectification effect and spin pumping. Since the current flows within the metallic NiFe layer only, it allows for the selective characterisation of NiFe dynamics, with or without magnetic coupling to the adjacent insulating YIG layer depending on whether a spacer layer is present. By suppressing all exchange interactions through introducing a SiO_2 spacer layer, we find that the dipolar interaction can be quite significant in influencing magnetisation dynamics in the YIG/NiFe bilayer, particularly when one FM layer is much thicker than the other. (ie. YIG (substrate)/NiFe (film)) Due to the nature of the electrical measurement, the static and

dynamic dipolar interaction due to the YIG layer on NiFe can be quite clearly separated. In particular, we find that the dynamic dipolar interaction is directly responsible for the non-zero rectified voltages while the static dipolar interaction manifests itself as an anisotropy field along the applied field direction. Based the results, the strength of the static and dynamic dipolar field produced by the YIG substrate that acts onto the NiFe layer can also be estimated.

6.2 Experimental Procedures

The YIG substrates used in our experiments are polycrystalline of dimensions 10 mm × 5 mm × 0.5 mm thick. Films of SiO_2, NiFe, Pt and Cu are deposited onto the YIG substrates by rf magnetron sputtering at room temperature and base chamber pressure of $\sim 7\times10^{-7}$ Torr using SiO_2, $Ni_{80}Fe_{20}$, Pt and Cu targets. The deposited films are patterned into 2 mm × 5 mm strips of the following layered structures: YIG/NiFe (20/200 nm), YIG/Cu(10 nm)/NiFe (20/200 nm), YIG/SiO_2(10/50 nm)/NiFe (20/200 nm) and YIG/SiO_2 (10/50 nm)/Pt (20 nm), where the film thicknesses are controlled by the sputtering rate and verified by a depth profile meter. The continuity of the SiO_2 layers are verified by atomic force microscopy (AFM), in which the surface roughness is determined to be much smaller than the film thickness. The samples are measured locally and electrically via lock-in techniques at 11 kHz amplitude modulation frequency, where dc voltages are generated in the presence of microwave excitation produced from a shorted coaxial probe. (Figure 6.1) Magneto-optical Kerr effect microscope is used to determine the magnetisation characteristics of the thin film NiFe layer deposited on YIG.

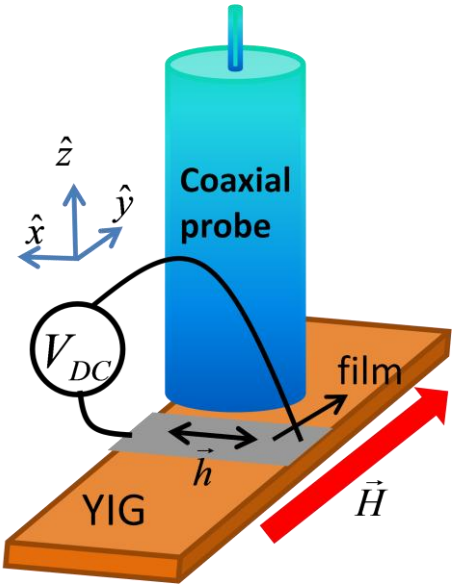

Figure 6.1 Schematic diagram of the measurement setup and sample configuration.

6.3 Results and discussions

6.3.1 Microwave induced dc voltages in YIG/NiFe bilayers

The magnetic system of interest here consists of the ferrimagnetic YIG (bulk)/NiFe (film) bilayer. Under microwave excitation by our shorted coaxial probe described in the previous chapter, the spins from both FM layers are excited into precession. Thus, at resonance, spin pumping occurs in both layers so that the spins from each FM layer are pumped into the other layer.

Within the conducting NiFe layer, this pumped spin current $\vec{j}_s \propto \vec{m} \times d\vec{m}/dt$ from YIG can dissipate via ISHE into a transverse charge current $\vec{j}_c \propto \vec{j}_s \times \hat{n}L$, where $\hat{n}$ is an out-of-plane unit vector and $L = \Delta H^2 / \left[4\left(H - H_r\right)^2 + \Delta H^2 \right]$ is the Lorentzian lineshape with resonance field H_r and linewidth ΔH under an applied field H. This ISHE charge current

$\vec{j}_c$ adds to the charge current already produced via SRE within NiFe whose resulting SRE dc voltage, primarily due to the rectification of the oscillating anisotropic magnetoresistance (AMR) with the microwave current, can be approximated (neglecting AHE) as

$$V_{SRE} \propto \Delta R \,|\, \vec{j} \,||\, \vec{h} \,|\left(D^{\mathrm{NiFe}} \cos\Phi - L^{\mathrm{NiFe}} \sin\Phi\right), \qquad (6.1)$$

where ΔR is the change in resistance due to AMR, $\vec{j}$ and $\vec{h}$ are respectively the microwave current and magnetic field, D^{NiFE} and L^{NiFe} are the dispersive and lorentzian lineshape functions centered about the NiFe FMR field H_r^{NiFe} respectively, and Φ is the microwave phase between $\vec{j}$ and $\vec{h}$. However, the other pumped spin current from the NiFe layer cannot lead to ISHE within the YIG layer since the latter layer is insulating.

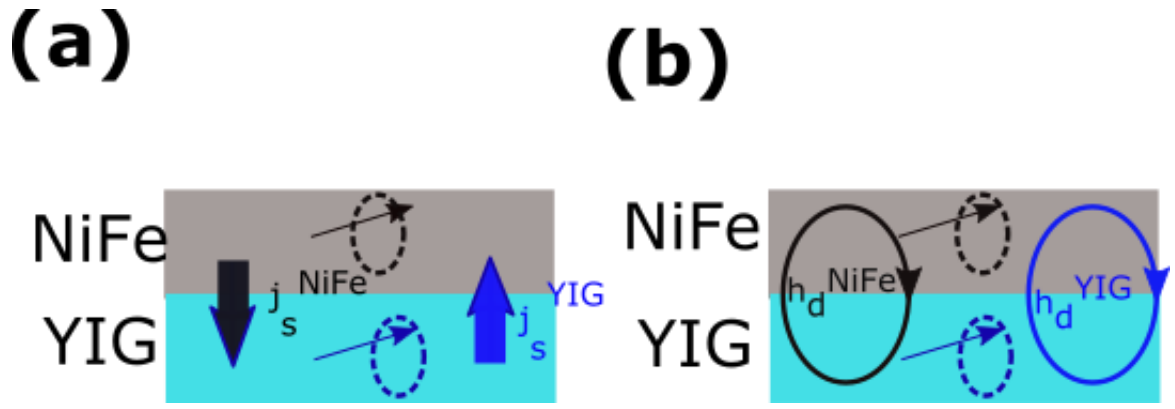

Figure 6.2(a) Spin-pumped currents j_s^{NiFe} and j_s^{YIG} from NiFe and YIG respectively produced at their simultaneous ferromagnetic resonance, whose ac components enhances the spin precessions of the other adjacent layer via spin torque. (b) Long range dynamic fields h_d^{NiFe} and h_d^{YIG} due to NiFe and YIG spin precessions respectively at simultaneous resonance, which enhances the spin precessions of the other adjacent layer. (Not drawn to relative scale) Adapted with permission from Ref. [7].

It has been recently found[8] that interestingly, at the simultaneous magnetic resonance of both FM layers (ie. YIG and NiFe), both the SRE and ISHE voltages may be significantly enhanced. This has been suggested to be due to two possible mechanisms: (i) the ac component of the spin-pumped current from the metallic FM enhances the FMR of the adjacent insulating FM via spin torque transfer, and vice versa (Figure 6.2(a)), and (ii) the dynamic magnetic fields from insulating FM spin precession enhances the FMR of the metallic FM layer via field torque, and vice versa (Figure 6.2(b)). However, while Ref. [8] showed that both SRE and ISHE signals can be enhanced near the simultaneous resonances of both layers, the quantitative contributions from each possible mechanism (i) and (ii) are still unclear since SRE and ISHE signals could not be clearly separated in that case. We attempt to address this issue here.

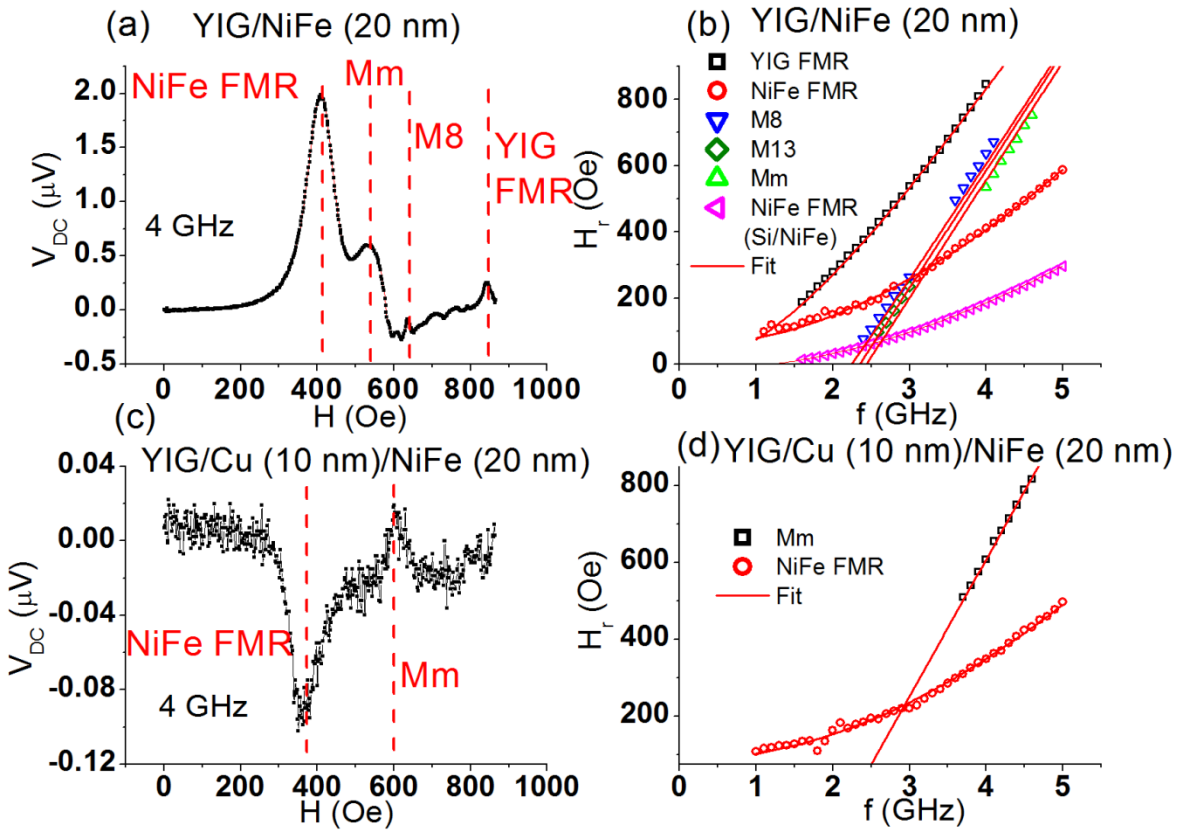

Figure 6.3 The measured voltage spectra V_{DC} at 4 GHz for (a) YIG/NiFe (20 nm) and (c) YIG/Cu (10 nm)/NiFe (20 nm) samples. The corresponding extracted frequency dependence of the resonance field H_r of various precession modes for (b) YIG/NiFe (20 nm) and (d) YIG/Cu (10 nm)/NiFe (20 nm) samples. The frequency dependence of resonance field for the Si/NiFe (20 nm) sample is also plotted in (b). Adapted with permission from Ref. [7].

YIG/NiFe (20 nm)

For the YIG/NiFe (20 nm) sample, the measured voltage spectra is obtained (Figure 6.3(a)), and the corresponding dispersion relations of the various modes are extracted and plotted in Figure 6.3(b). Remarkably, we observe clear peaks originating from the resonances of both YIG and NiFe modes. In particular, the mode corresponding to NiFe FMR, which stems from its own SRE, can be identified via a fit of its dispersion relation to the Kittel equation $f = (\gamma / 2\pi)\sqrt{(H + H_k)(H + H_k + 4\pi M_{eff})}$, with effective magnetisation

$4\pi M_{eff} \approx 5400$ G (for bulk NiFe, saturation magnetisation $4\pi M \approx 10$ kG), and effective anisotropy field $H_k \approx -55$ Oe. For subsequent fits to NiFe FMR for the other films on YIG substrate presented here, the extracted $4\pi M_{eff}$ ranges from 5400-9800 G, with H_k from -38 Oe to -88 Oe. This discrepancy of $4\pi M_{eff}$ from the bulk saturation value is likely the result of surface anisotropy as well as YIG/NiFe interfacial exchange coupling. However, we find that the presence of a negative in-plane effective anisotropy H_k is quite peculiar. This will be elucidated in greater detail later. The YIG FMR mode is also identified with $4\pi M_{eff} \approx 1620$ G and $H_k \approx 0$ consistent with the bulk values for polycrystalline YIG substrates.

In addition, as also seen in the previous chapter, peaks due to magnetostatic surface spin waves (MSSWs) in YIG with wave vector $k = n\pi/(5\text{ mm})$ can be identified (M8 and M13, where the number denotes the mode number n). The Mm mode corresponds to a superposition of YIG MSSWs with wave vectors $k > 100$ cm^{-1}, since such modes occur at the same resonance field position in the spectra. The presence of modes due to YIG FMR, M8, M13 and Mm suggests that spin pumping has occurred from YIG into NiFe where the pumped spin current dissipates via ISHE into a measurable voltage. However, it is important to note that, as evidenced in Figure 6.3(b), the finite-linewidth resonances of NiFe and YIG modes can overlap and cross one another, resulting in simultaneous resonances that may enhance both SRE and ISHE voltages based on mechanism (i) and/or (ii) described above. Therefore the origin of the peaks may not be as clear-cut.

YIG/Cu(10 nm)/NiFe (20 nm)

To investigate further, we insert a Cu spacer between the FM layers and repeated the measurements, with results shown in Figure 6.3(c) for the YIG/Cu (10 nm)/NiFe (20 nm) trilayer. We observe two clear modes: one due to SRE at NiFe FMR and the other can be identified as the Mm mode of YIG MSSWs. (Figure 6.3(d)) Since Cu is essentially transparent to spin currents due to its long spin diffusion length, the occurrence of the Mm mode is not unexpected, though other MSSW modes appear to be absent. This is most likely due to the decrease in voltage signal from the shunting effect of Cu layer that cause other MSSW modes (which is much weaker than the Mm mode) to be less resolvable in the spectra. The effect of the Cu spacer does not distinguish between mechanisms (i) or (ii) at near simultaneous FMR since neither one nor the other is suppressed, but simply confirms our results for the YIG/NiFe (20 nm) sample, and acts as a control for our subsequent experiments.

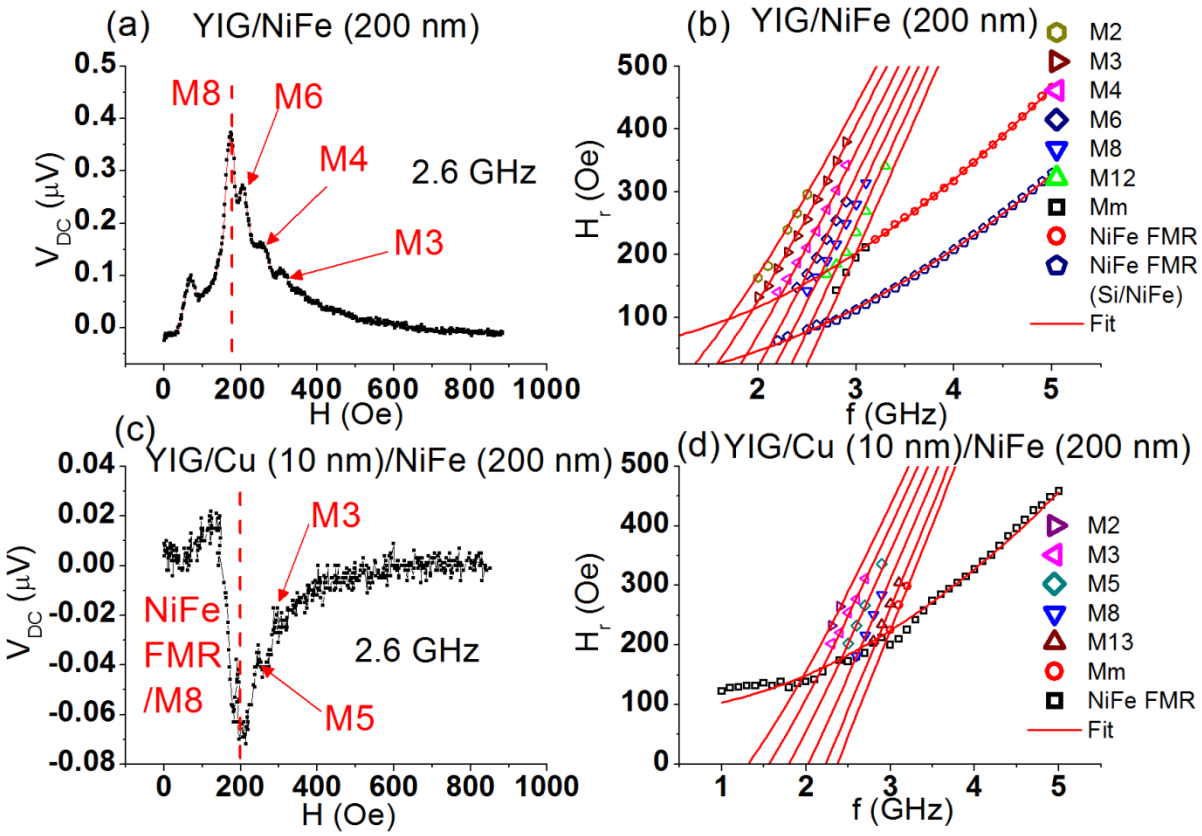

Figure 6.4 The measured voltage spectra at 2.6 GHz for (a) YIG/NiFe (200 nm) and (c) YIG/Cu (10 nm)/NiFe (200 nm) samples, and the corresponding frequency dependence of the resonance field H_r of various modes for (b) YIG/NiFe (200 nm) and (d) YIG/Cu (10 nm)/NiFe (200 nm) samples. The resonance field for the Si/NiFe (200 nm) sample is also shown in (b). Adapted with permission from Ref. [7].

YIG/NiFe (200 nm) & YIG/Cu (10 nm)/NiFe (200nm)

Next, we find it instructive to use a thicker NiFe film. As such FM materials are known to have a rather short spin diffusion length λ_d (~2 nm)[9,10], we expect that a NiFe film that is much thicker (d=200 nm) than λ_d will exhibit a much diminished ISHE voltage since $V_{ISHE} \propto (1/d)\tanh(d/2\lambda_d)$. The SRE contribution, on the other hand, should remain approximately independent on film thickness as long as it is thinner than the microwave skin depth (~ 0.1 μm at 2.5 GHz).

However surprisingly, this is not the case, as the voltage signals from YIG MSSW modes remain as strong as that of the YIG/NiFe (20nm) sample even when the NiFe film is 200 nm thick (Figure 6.4(a)). Note, that conventional ISHE theory would have predicted a decrease in V_{ISHE} by at least an order of magnitude. (Also, the decreased film resistance with increasing d would also have further led to a decrease in V_{ISHE}.) Therefore, due to these factors, signals from YIG MSSWs should not have been observable here.

These results are confirmed with measurements from a YIG/Cu (10 nm)/NiFe (200 nm) sample (Figure 6.4(c), (d)), where a Cu spacer is added, that shows these YIG MSSW modes remain. The results so far cannot be adequately explained by invoking the conventional spin pumping and ISHE mechanism for the bilayers, and an alternative explanation is needed.

6.3.2 Microwave induced dc voltages in YIG/SiO_2/NiFe trilayers

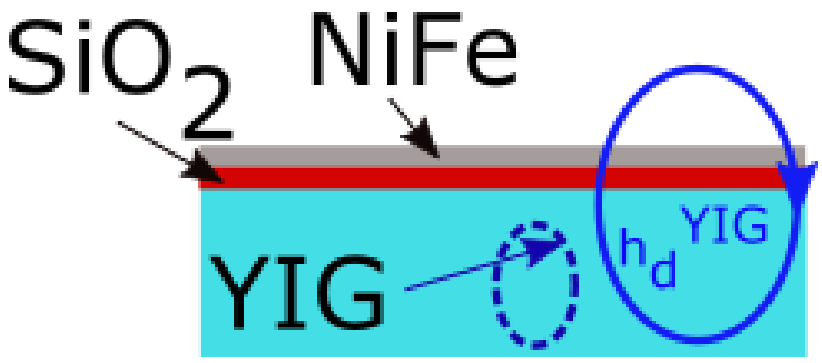

Figure 6.5 Schematic diagram of the YIG (bulk)/SiO_2 (film)/NiFe (film) trilayer. The dipolar fields h_d^{YIG} from YIG extend into the NiFe layer to influence the latter's dynamics.

The presence of YIG MSSW voltages that persist even for thick NiFe films suggests that the long-range dynamic dipolar interaction between YIG MSSWs and the adjacent NiFe layer might be responsible. To test this theory, we make use of SiO_2, a non-magnetic insulator, as a spacer between the YIG and NiFe layer, to suppress all short-range exchange interactions and thus spin pumping between YIG and NiFe. (Figure 6.5) We surprisingly find that the voltage signals from YIG MSSW modes persist for the YIG/SiO_2 (10 nm)/NiFe (20 nm) sample (Figure 6.6(a), (b)), while YIG MSSW modes can be clearly seen even for the YIG/SiO_2 (50 nm)/NiFe (200 nm) sample (Figure 6.6(c)). However, a more detailed angular measurement to distinguish whether these signals are due to spin pumping or SRE could not be done here when MSSWs are involved since their wave vectors (and thus resonance field and amplitude) also changes with angular orientation of applied field, which complicates the issue. Nonetheless, the presence of a 50 nm thick SiO_2 spacer would definitively suppress spin pumping, as it is well-established that a SiO_2 layer ~5 nm[10,11] is already sufficiently thick to definitively suppress spin pumping across layers. As a control, we present the measured voltage spectra for YIG/SiO_2 (10, 50 nm)/Pt (20 nm) films, showing that indeed no spin pumping related ISHE signals remain. (Figure 6.6(d))

A closer inspection of the spectra for both samples (Figure 6.6(a) and (c)) shows that these YIG modes appear to be enhanced near the self-SRE of NiFe FMR, and that the modes are clearly not necessarily Lorentzian. The non-Lorentzian nature of these ISHE modes were previously observed[12] in YIG/NiFe bilayers and had been attributed to a competition between the spin pumping from YIG and NiFe. However, this effect does not apply here due to the presence of a SiO_2 spacer that prevents spin pumping in the first place. The presence of the YIG MSSW voltages even without spin pumping is likely due to the influence of the long-range YIG dynamic dipolar fields $\vec{h}_d^{\,YIG}$.

Under excitation by a microwave field $\vec{h}$, the spins of the YIG magnetisation $\vec{m}$ precess and produce a dipolar field $\vec{h}_d^{\,YIG}$ at a distance r given by $h_d^{\,YIG} = -\nabla\phi(r)$, where the scalar potential $\phi(r)$ is given by

$$\phi(r) = -\frac{1}{4\pi}\nabla_r \cdot \int \frac{\vec{m}(r_i)}{|r - r_i|} d^3 r_i. \qquad (6.2)$$

Here, r_i is the distance of the i^{th} spin from the origin which is taken to be at the centre of the sample and $\vec{m} = \chi\vec{h}$, where χ is the dynamic YIG susceptibility defined in equation (1.9). Note that the quantity $\nabla \cdot \vec{m}$ in equation (6.2), analogous to that in the electric potential, can be interpreted as a 'magnetic charge' that produces dipolar fields whenever it is non-zero. Thus, within the NiFe layer, both the microwave field $\vec{h}$ and the dynamic dipolar field from YIG $\vec{h}_d^{\,YIG}$ can excite the NiFe spins and produce a dc voltage via SRE upon rectification with the rf current $\vec{j}$. From equation (6.1), with $\vec{h} \to \vec{h} + \vec{h}_d^{\,YIG}$ we obtain the resulting dc voltage as

$$\begin{aligned} V_{SRE} &\propto \Delta R \,|\, \vec{j} \,||\, \vec{h} + \vec{h}_{dip}^{\,YIG} \,|\left(D^{\mathrm{NiFe}} \cos\Phi - L^{\mathrm{NiFe}} \sin\Phi\right), \\ &= V_{SRE}^{\,NiFe} + V_{SRE}^{\,dip} \end{aligned} \qquad (6.3)$$

where the contribution from microwave field $\vec{h}$ produces the usual self-SRE of NiFe $V_{SRE}^{\,NiFe}$ and the dipolar field $\vec{h}_{dip}^{\,YIG}$ generates a non-local YIG voltage $V_{SRE}^{\,dip}$ in the NiFe layer. As D^{NiFe} and L^{NiFe} are both non-zero only near NiFe FMR and $\vec{h}_{dip}^{\,YIG}$ peaks at YIG spin resonance, $V_{SRE}^{\,dip}$ only appears near the simultaneous resonance of both the YIG and NiFe layers. This can be observed in Figure 6.6, where we see YIG modes being superimposed

within the finite linewidth spectra of the NiFe SRE signal. This also accounts for the observed non-Lorentzian nature of the YIG peaks since V_{SRE}^{dip} also depends on the microwave phase Φ, which is non-zero in general.

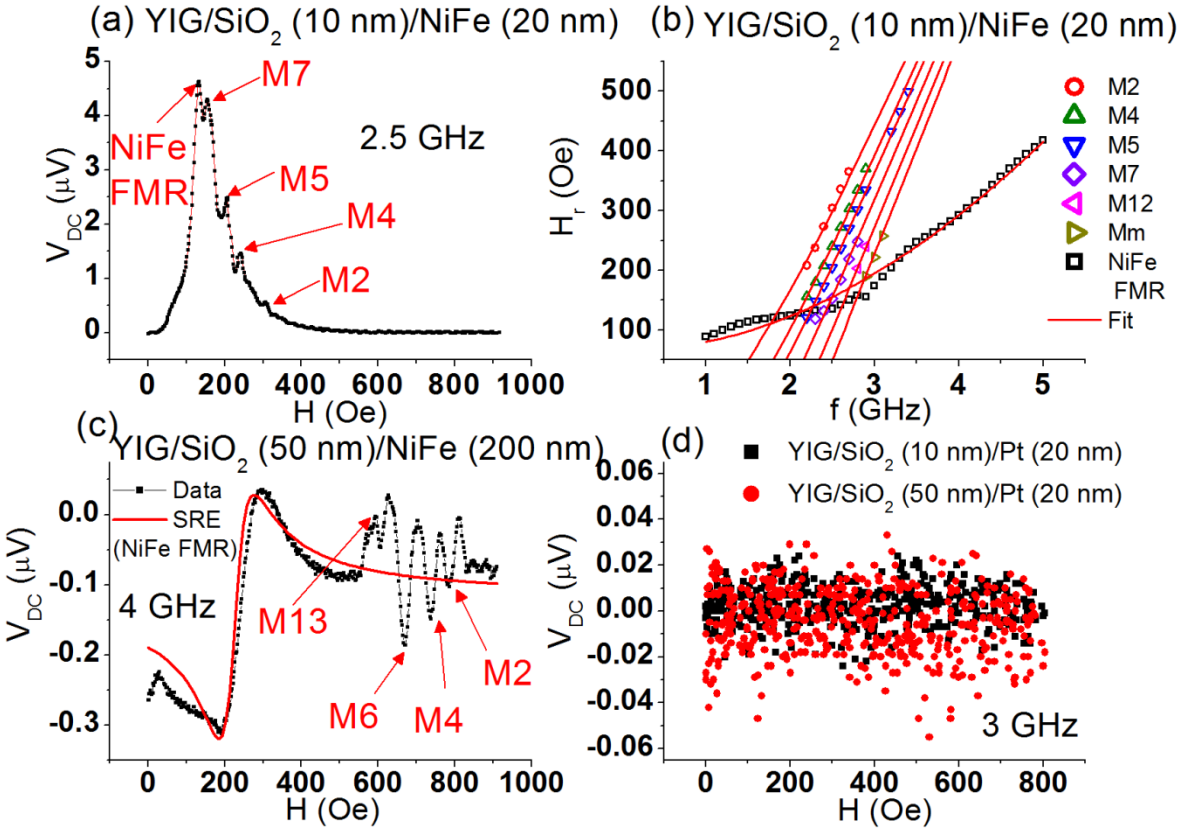

Figure 6.6 The measured voltage spectra for YIG/SiO_2 (10 nm)/NiFe (20 nm) at 2.5 GHz, and the (b) corresponding frequency dependence of the resonance field H_r of various modes for YIG/SiO_2 (10 nm)/NiFe (20 nm). (c) The measured voltage spectra for YIG/SiO_2 (50 nm)/NiFe (200 nm) sample at 4 GHz and for the (d) YIG/SiO_2 (10 nm)/Pt (20 nm) and YIG/SiO_2 (50 nm)/Pt (20 nm) samples at 3 GHz. Adapted with permission from Ref. [7].

6.4 Quantifying the static and dynamic YIG dipolar fields

Thus far, the results point towards the important role played by dipolar fields in influencing the dynamics of YIG/NiFe and YIG/SiO_2/NiFe systems. Due to the clear SRE signals observed, we demonstrate here that it is possible to make use of the YIG/SiO_2/NiFe trilayer to separate and quantify both the static and dynamic dipolar fields produced by YIG, using the NiFe layer as a detector. This is possible due to the following reasons:

1) The use of YIG in bulk form increases the strength of its dipolar field in its vicinity.

2) The adjacent NiFe layer can detect the YIG dipolar fields via SRE.

3) The use of a SiO_2 spacer that suppresses exchange interactions between YIG and NiFe so as not to contaminate the signals via spin pumping.

6.4.1 Calculating the dipolar fields produced by a rectangular YIG substrate

In this part, we first calculate the dipolar fields emanating from our rectangular YIG substrate that are influencing the dynamics of the adjacent NiFe layer in order to elucidate its relative strength and distribution. The dipolar fields H^{dip} can be calculated in an efficient manner with $H^{dip} = -\nabla\phi$ and the scalar potential defined in equation (6.2). Ref. [13] details such a procedure. Assuming that the magnetisation is saturated along the *y*-axis ($\vec{M} = M_0\hat{y}$), the static dipolar field $H^{dip} = \left(H_x^{dip}, H_y^{dip}, H_z^{dip}\right)$ for a YIG slab centered at (0,0,0) with dimensions of $2x_b$, $2y_b$ and $2z_b$ along the *x*, *y*, and *z* axes respectively, can be calculated to be[13]

$$H_x^{dip} = \frac{M_0}{4\pi}\sum_{k,l,m=1}^{2}(-1)^{k+l+m}\ln\left\{z+(-1)^m z_b+\sqrt{\left[x+(-1)^k x_b\right]^2+\left[y+(-1)^l y_b\right]^2+\left[z+(-1)^m z_b\right]^2}\right\}, \quad (6.4)$$

$$H_y^{dip} = -\frac{M_0}{4\pi}\sum_{k,l,m=1}^{2}(-1)^{k+l+m}\frac{\left[y+(-1)^l y_b\right]\left[x+(-1)^k x_b\right]}{\left|y+(-1)^l y_b\right|\left|x+(-1)^k x_b\right|}\times \arctan\left\{\frac{\left|x+(-1)^k x_b\right|\left[z+(-1)^m z_b\right]}{\left|y+(-1)^l y_b\right|\sqrt{\left[x+(-1)^k x_b\right]^2+\left[y+(-1)^l y_b\right]^2+\left[z+(-1)^m z_b\right]^2}}\right\}, \quad (6.5)$$

$$H_z^{dip} = \frac{M_0}{4\pi}\sum_{k,l,m=1}^{2}(-1)^{k+l+m}\ln\left\{x+(-1)^k x_b+\sqrt{\left[x+(-1)^k x_b\right]^2+\left[y+(-1)^l y_b\right]^2+\left[z+(-1)^m z_b\right]^2}\right\}. \quad (6.6)$$

Using the above equations, we can plot in Figure 6.7 below the 3-D vector distribution of the YIG static dipolar field in the NiFe film region (100 nm above the YIG surface). We see that the *z*-component is dominant here, as expected since the film lies directly above the YIG in the *z*-direction. The contributions near the poles at the $y = \pm 5\text{mm}$ are also clearly stronger than at the centre where *y*=0. These dipolar fields can influence the NiFe layer. However, due to the large demagnetizing field in the *z*-direction for the NiFe film, the relatively weak dipolar fields produced by the YIG slab will not be able to significantly affect the *z*-component of NiFe magnetisation. Hence, the out-of-plane component of the static dipolar field can be neglected. This leaves us only with the in-plane component of the static dipolar field which can influence the NiFe magnetisation, whose distribution is shown in Figure 6.8. From Figure 6.8, we can again see that the *y*-component is stronger near the poles, and that the dipolar field direction is opposite to the YIG magnetisation. Two main regions can thus be identified: Mid region, where the static dipolar fields are weak; and side region, where the dipolar field is much stronger.

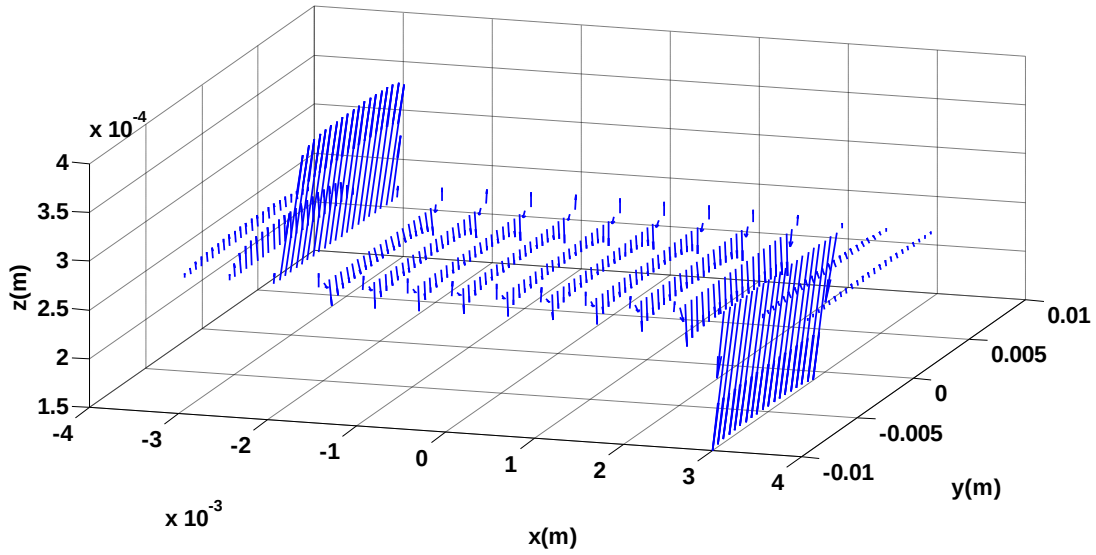

Figure 6.7 Vector 3-D plot of the static YIG dipolar field on the *x*-*y* plane 100 nm above from the YIG surface, where the 200 nm thick NiFe film resides.

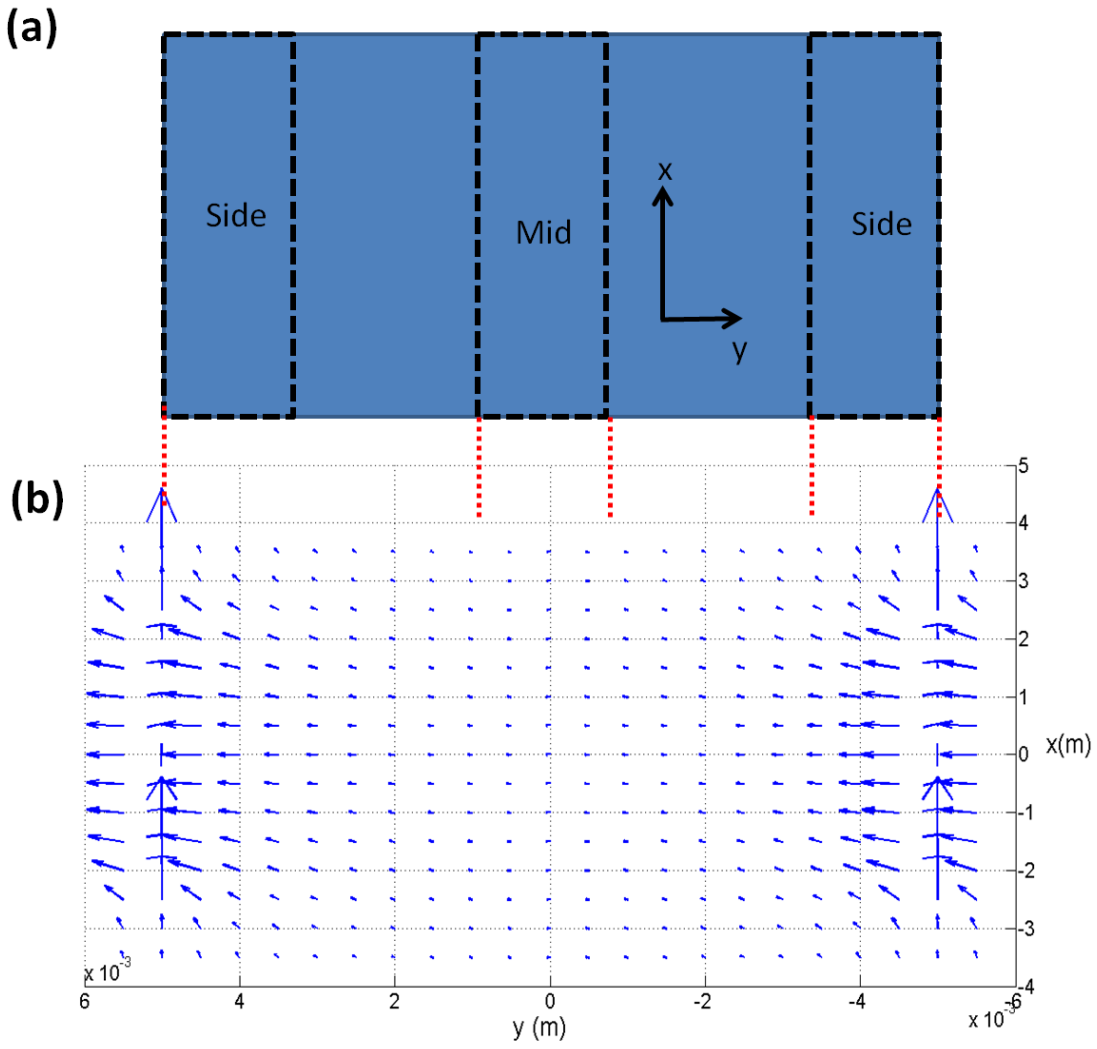

Figure 6.8(a) The YIG substrate (*x*-*y* plane) being split into three regions labelled 'mid' and 'side. (b) The distribution of the *y*-component of the static YIG dipolar field in the corresponding regions in (a). Note that the YIG magnetisation lies in the –*y* direction, opposite to the dipolar field direction shown.

Next, we attempt to estimate the dynamic components of the YIG dipolar fields produced by its own precession from equations (6.4), (6.5) and (6.6). First, note that these equations give us the components of the dipolar field produced by the *y*-component of the YIG magnetisation (i.e M_y). We would like to know the dynamic YIG dipolar fields produced by the m_x and m_z components as well due to spin precession about the *y*-axis. This can be

done by transforming the coordinate systems of equations (6.4), (6.5) and (6.6). For instance, to find the dynamic dipolar fields $\vec{h}' = (h_x', h_y', h_z')$ produced when *M* is along *x* (i.e m_x), we can simply make use of the above equations with the following coordinate transformations and substitution:

$$\begin{aligned} h_x' &= H_y(y \leftrightarrow x, z \to z, M_0 \to m_x), \\ h_y' &= H_x(y \leftrightarrow x, z \to z, M_0 \to m_x), \\ h_z' &= H_z(y \leftrightarrow x, z \to z, M_0 \to m_x). \end{aligned} \qquad (6.7)$$

Here, $\leftrightarrow$ denotes that the coordinates are interchanged. Similarly, the dynamic dipolar fields $\vec{h}'' = (h_x'', h_y'', h_z'')$ due to m_z is given by the following:

$$\begin{aligned} h_x'' &= H_x(y \leftrightarrow z, x \to x, M_0 \to m_z), \\ h_y'' &= H_z(y \leftrightarrow z, x \to x, M_0 \to m_z), \\ h_z'' &= H_y(y \leftrightarrow z, x \to x, M_0 \to m_z). \end{aligned} \qquad (6.8)$$

With equations (6.7) and (6.8), and with $m_x = -\gamma M_0 h_x / \alpha\omega$ and $m_z = -h_x / \alpha$ in the measurement configuration, we plot the distribution of the YIG dynamic dipolar fields in the NiFe film region in Figure 6.9. Note that this result is an estimation of the magnitude of the dynamic dipolar fields produced, assuming that the precession is uniform, which may not reflect that of the MSSW modes. Nonetheless, it is still an adequate estimation of their relative strengths and distributions.

From Figure 6.9(a), we see that the dominant contribution of the YIG dynamic dipolar field points in the out-of-plane direction, as expected since the precession of the spin has an out-of-plane component that induces magnetic charges on the surface of YIG substrate (where NiFe film resides). We plot the calculated magnitude of the *z* component of the dynamic dipolar fields relative to the position of our NiFe film in Figure 6.9(b), showing

clearly that the regions with the strongest field lies towards the sides of our measured regions, which is expected since the *x* component of the spin precession produces magnetic charges on the side faces of the YIG substrate. In the central region (centered at *x*=0), $\vec{h}_{dip}^{\,YIG}$ has a magnitude of around 10 Oe. Since the central region about x=0 is where the bulk of the NiFe film resides (regardless of whether being in the side or mid configuration), we should expect that the total effective $\vec{h}_{dip}^{\,YIG}$ experienced by the NiFe film to be closer to 10 Oe. Also, as these components of the dynamic YIG dipolar fields can be perpendicular to the NiFe static magnetisation (which is along *y*), they can hence influence the spin dynamics of the NiFe layer.

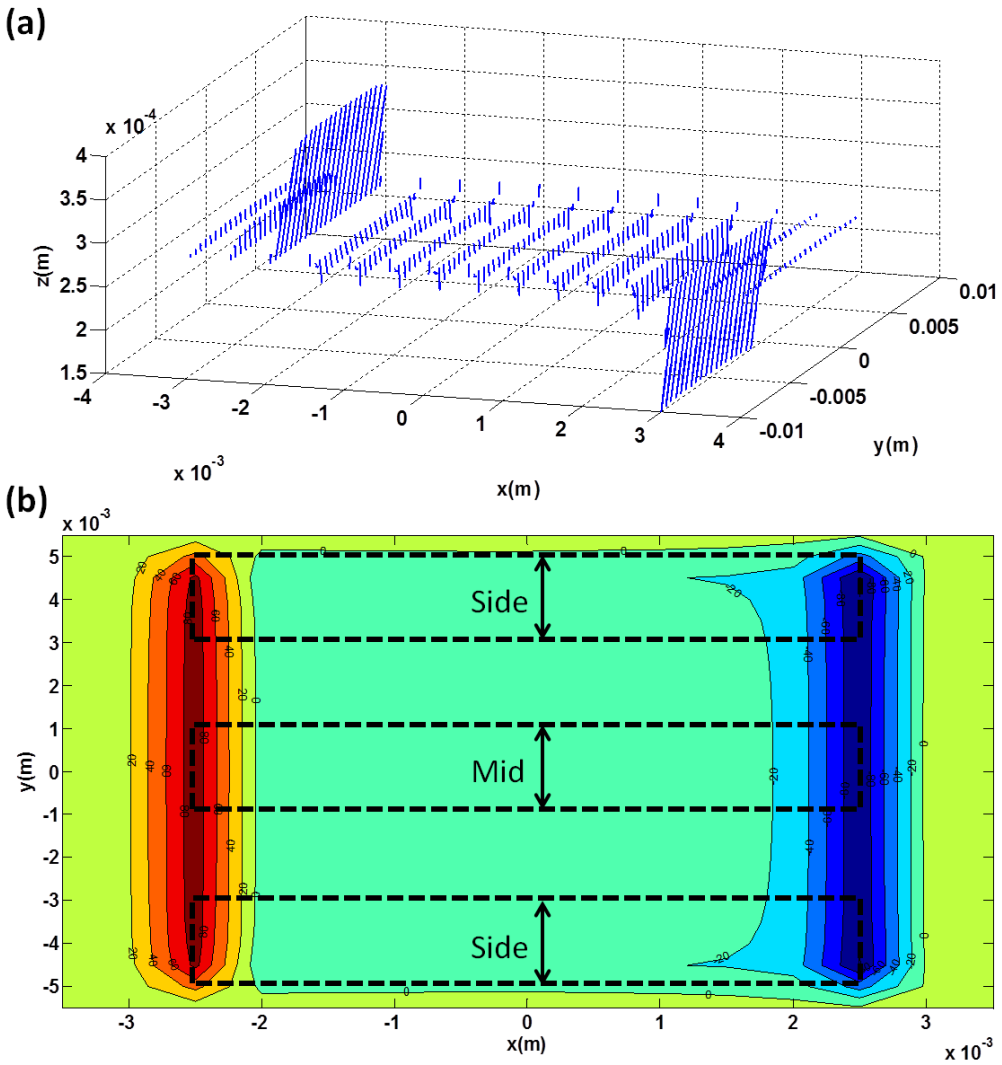

Figure 6.9 (a) Vector 3-D plot of the dynamic YIG dipolar field at 4.4 GHz, produced by the m_x and m_z components of the YIG dynamic magnetisation, on the *x*-*y* plane 100 nm above from the YIG surface, where the 200 nm thick NiFe film resides. (b) Contour plot of the z-component of the dynamic YIG dipolar field. Red: 120 Oe with contours decreasing in steps of 20 Oe.

6.4.2 Static YIG dipolar field

From the above considerations summarised in Figure 6.8, we see that the distribution of the static dipolar field due to the YIG magnetisation over the NiFe film can be roughly split into two regions: the mid region where the field is the weakest, and the side region

where the field is strongest. This suggests that the NiFe film experiences differing dipolar fields depending on its location on the YIG substrate. Therefore, we patterned our NiFe films onto the side and mid regions of the YIG substrate (Figure 6.10(a)) and repeated the above voltage measurements for comparison. The influence of static YIG dipolar fields on the NiFe layer should manifest in its own FMR spectra, hence we are particularly interested in the voltage peaks corresponding to NiFe FMR.

We show in Figure 6.10(b) the variation of the mode resonance field with microwave frequency obtained from a frequency sweep of the voltage spectra, for samples patterned in the mid and side configurations. The NiFe curves have been fitted to the following Kittel equation for thin film FMR,

$$H_r = \sqrt{\left(\frac{\omega}{\gamma}\right)^2 - 4\pi M_s H_k + \left(\frac{4\pi M_s + H_k}{2}\right)^2} - \frac{4\pi M_s + H_k}{2}, \qquad (6.9)$$

where γ is the gyromagnetic ratio, $4\pi M_s \approx 10$ kG is the saturation magnetisation and H_k is the effective in-plane uniaxial anisotropy field. Sample 1 consists of YIG/SiO_2(50nm)/NiFe(200nm), where only dipolar interactions are present between the FM layers, whereas for sample 2, the absence of the SiO_2 spacer allows exchange coupling between the layers as well.

Consistently, we observe that for both samples measured in the side configuration, the plot in Figure 6.10(b) is always shifted upwards by δH as compared to the mid configuration. The relatively negligible difference between samples 1 and 2 for the same measurement configuration (whether side or mid) indicates that exchange interaction is likely insignificant, even in sample 2 where the spacer layer is absent. This can be understood in the context that the typical exchange length (~1-10nm) is much smaller than the NiFe film

thickness of 200 nm. This observed trend in Figure 6.10(b) manifests itself in the H_k term in equation (6.9), which causes the curve to displace vertically. In fact, a *negative* value for H_k is obtained for both mid and side configurations, being around -15 Oe and -100 Oe respectively. The only scenarios whereby H_k could be negative are the presence of large perpendicular anisotropy, or that the sample is being measured along the hard axis. Our MOKE analysis, however, rules out both of these possibilities. (see Appendix) The samples are found to have negligible anisotropy, thus the large negative H_k values are largely due to the effect of the static YIG dipolar field $\vec{H}_{sta}^{\,YIG}$ acting opposite in direction to the applied field H, resulting in a pseudo negative anisotropy in NiFe layer. The magnitudes of the extracted H_k values are also consistent with the calculated $\vec{H}_{sta}^{\,YIG}$ values presented in Figure 6.10(b) for their respective side and mid configurations. (Note that only the *y*-component of $\vec{H}_{sta}^{\,YIG}$ manifests itself in the measured H_k) Lastly, as a control, we also present in Figure 6.10(b) the data for Si/NiFe (200nm) film where external dipolar fields are absent, showing that its curves roughly coincides with YIG samples with NiFe patterned in the mid configuration where dipolar fields are weak.

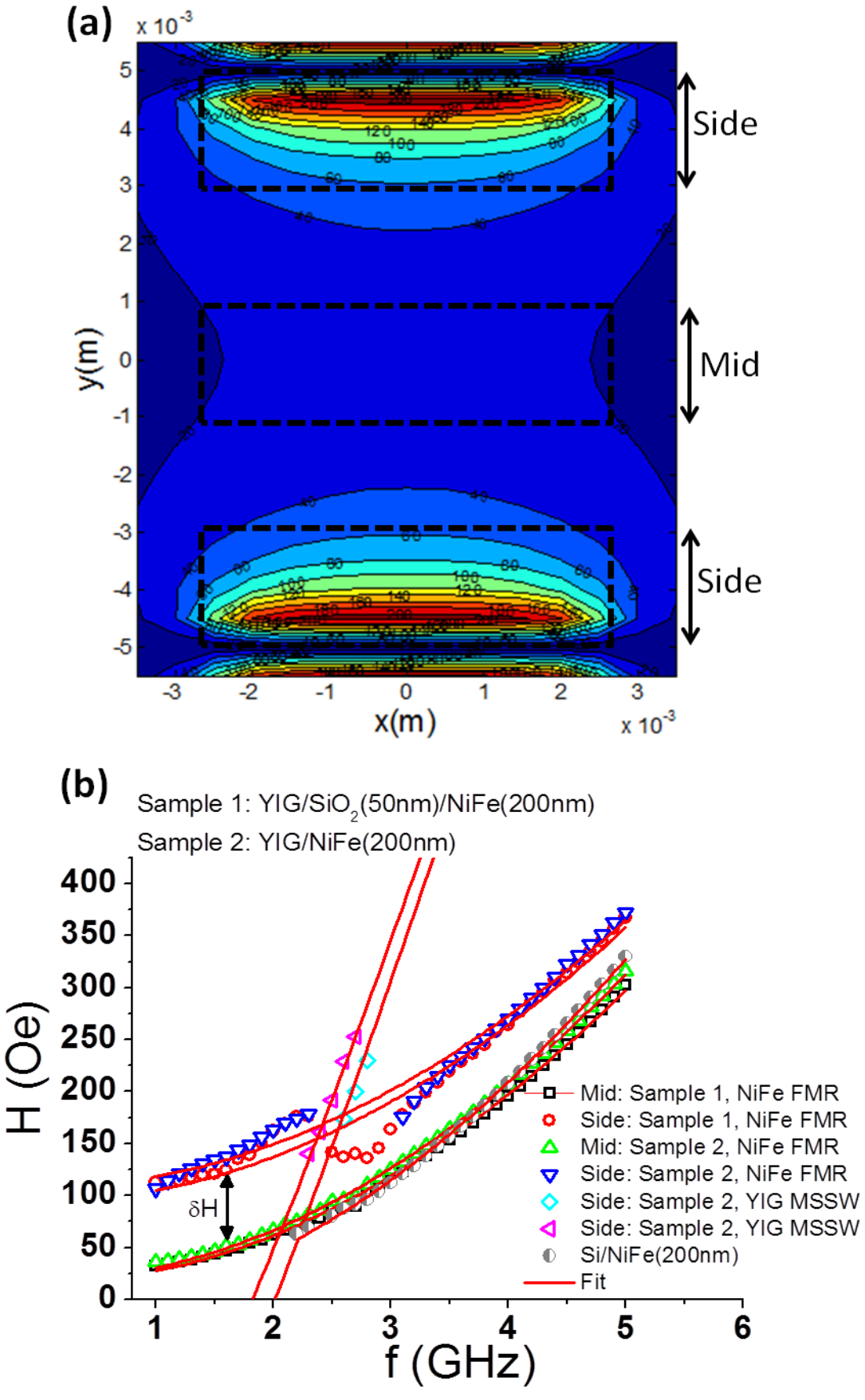
(a)
x 10^-3
Side
Mid
Side
y(m)
x(m)
x 10^-3
(b)
Sample 1: YIG/SiO2(50nm)/NiFe(200nm)
Sample 2: YIG/NiFe(200nm)
H (Oe)
f (GHz)
δH
Mid: Sample 1, NiFe FMR
Side: Sample 1, NiFe FMR
Mid: Sample 2, NiFe FMR
Side: Sample 2, NiFe FMR
Side: Sample 2, YIG MSSW
Side: Sample 2, YIG MSSW
Si/NiFe(200nm)
Fit

Figure 6.10(a) Contour plot of the y-component of the static YIG dipolar field produced by the static y-component of the magnetisation. (b) Variation of resonance field of the modes for various samples as a function of microwave frequency.

6.4.3 Dynamic YIG dipolar field

From the discussion earlier, equation (6.3) describes the total contribution to the measured voltage spectra that comes from both the microwave field $\vec{h}$ and dynamic dipolar field $\vec{h}_{dip}^{\,YIG}$ excitations. The microwave field $\vec{h}$ generates the usual self-SRE of NiFe $V_{SRE}^{\,NiFe}$, while $\vec{h}_{dip}^{\,YIG}$ generates a non-local SRE $V_{SRE}^{\,dip}$ near simultaneous YIG and NiFe resonance. Figure 6.11 shows the corresponding voltages, whereby $V_{SRE}^{\,dip}$ due to the dynamic dipolar fields produced from YIG MSSWs appears in the backdrop of the finite-linewidth $V_{SRE}^{\,NiFe}$.

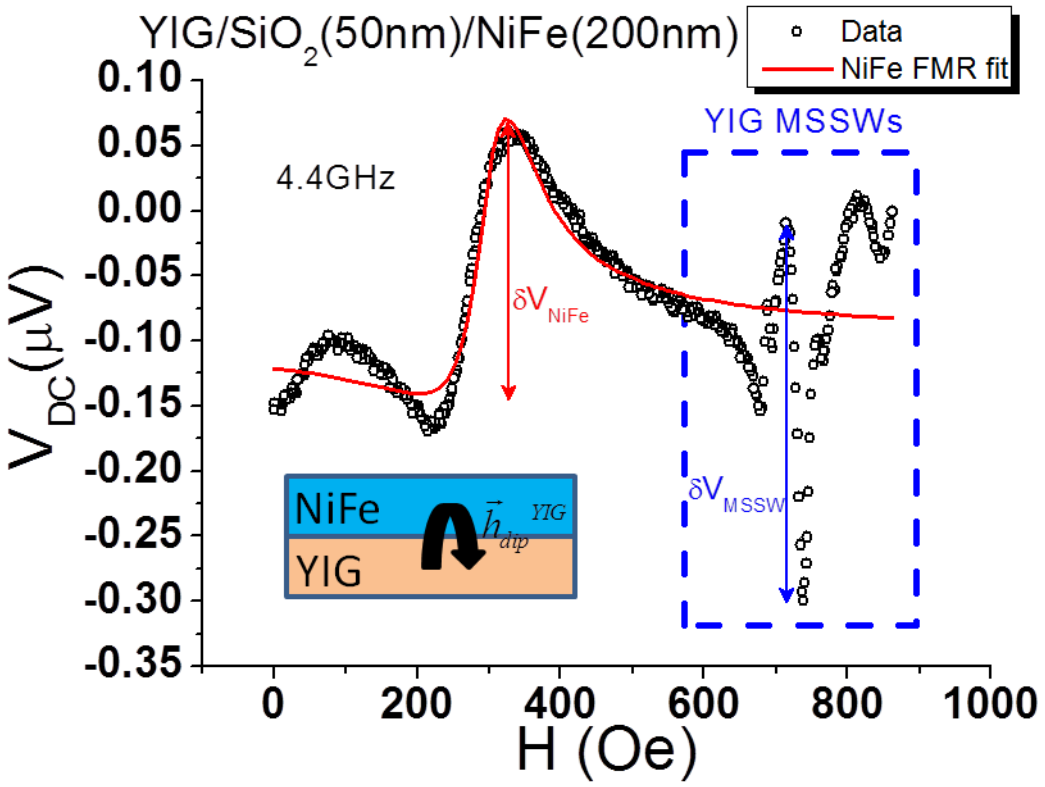

Figure 6.11 Voltage spectra obtained at 4.4 GHz for YIG/SiO_2(50nm)/NiFe(200nm) sample in the side measurement configuration. Inset: Influence of YIG dipolar field $\vec{h}_{dip}^{\,YIG}$ on the NiFe layer.

From (6.3), we may write

$$\begin{aligned} V_{SRE}^{\,NiFe} &= k\left|\vec{h}\right|\left(D^{\mathrm{NiFe}}\cos\Phi - L^{\mathrm{NiFe}}\sin\Phi\right) \\ V_{SRE}^{\,dip} &= k\left|\vec{h}_{dip}^{\,YIG}\right|\left(D^{\mathrm{NiFe}}\cos\Phi - L^{\mathrm{NiFe}}\sin\Phi\right), \end{aligned} \tag{6.10}$$

where k is a common constant. By comparing the measured voltage ratios $V_{SRE}^{\,NiFe}$ and $V_{SRE}^{\,dip}$, and by exploiting the fact $D^{NiFe}=0$ when $H=H_R^{\,NiFe}$ at NiFe FMR, we can express $\vec{h}_{dip}^{\,YIG}$ as

$$\left|\vec{h}_{dip}^{\,YIG}\right| = \frac{\left|\vec{h}\right| \sin\Phi \times V_{SRE}^{\,dip}(H = H_R^{\,YIG})}{\left\{ \frac{2\Delta H_{NiFe}\left(H_R^{\,YIG} - H_R^{\,NiFe}\right)\sin\Phi}{\left[4\left(H_R^{\,YIG} - H_R^{\,NiFe}\right)^2 + \Delta H_{NiFe}^{\,2}\right]} + \frac{\Delta H_{NiFe}^{\,2}\cos\Phi}{\left[4\left(H_R^{\,YIG} - H_R^{\,NiFe}\right)^2 + \Delta H_{NiFe}^{\,2}\right]} \right\} V_{SRE}^{\,NiFe}(H = H_R^{\,NiFe})}, \quad (6.11)$$

where $H_R^{\,NiFe}$ and ΔH_{NiFe} are the FMR field and linewidth of NiFe respectively and $H_R^{\,YIG}$ is the resonance field of the YIG mode. Note that equation (6.11) assumes that $\vec{h}_{dip}^{\,YIG}$ be sufficiently uniform over the local excitation region which may not be correct especially when YIG MSSW modes are involved in our case. With $\left|\vec{h}\right| \approx 0.1$ Oe obtained from finite element simulations of our coaxial probe as discussed in chapter 5, we calculate using equation (6.11), based on data extracted from Figure 6.11, that $\vec{h}_{dip}^{\,YIG} \approx 2.3 \pm 0.2$ Oe . This value is consistent in order of magnitude to the value of around 10 Oe predicted in section 6.4.1.

6.5 Conclusion

In this chapter, we have shown that the static and dynamic dipolar fields produced by a YIG substrate can dramatically influence the magnetisation dynamics of an adjacent ferromagnetic NiFe layer. This can pose potential pitfalls if not properly considered, especially in spin pumping and ISHE measurements since such dipolar fields can also produce spurious dc voltages via SRE. In particular, dc voltages due to YIG modes were detected within the NiFe layer under microwave excitation in YIG/NiFe systems, which persist even in the presence of a 50 nm-thick SiO_2 spacer and in 200 nm-thick NiFe films, thus rendering conventional spin pumping-induced ISHE within NiFe as the source of these

voltages highly unlikely. We attribute the long-range dynamic dipolar field due to YIG spin precession, analogous to a microwave field that drives the self-SRE in NiFe, as the source of these non-local YIG SRE voltages near the simultaneous resonance of both YIG and NiFe.

Further, we have demonstrated how this phenomenon can be utilised to allow a NiFe film to act as a detector of dipolar fields originating from the bulk, insulating ferromagnetic substrate YIG. Through electrical detection of spin resonance via SRE, we isolate the static and dynamic components of the YIG dipolar fields and estimate their respective magnitudes. Our method provides an effective way to study and characterise such dipolar fields as well as an attractive and convenient platform to further study the dynamic couplings between FM layers.

6.6 References

[1] S. Kaka, M. R. Pufall, W. H. Rippard, T. J. Silva, S. E. Russek, and J. A. Katine, Nature **437,** 389 (2005).

[2] D. Houssameddine, U. Ebels, B. Delaet, B. Rodmacq, I. Firastrau, F. Ponthenier, M. Brunet, C. Thirion, J. P. Michel, L. Prejbeanu-Buda, M. C. Cyrille, O. Redon, and B. Dieny, Nat Mater **6,** 441 (2007).

[3] O. Dmytriiev, T. Meitzler, E. Bankowski, A. Slavin, and V. Tiberkevich, J Phys Condens Matter **22,** 136001 (2010).

[4] A. A. Serga, A. V. Chumak, and B. Hillebrands, Journal of Physics D: Applied Physics **43,** 264002 (2010).

[5] P. S. Keatley, P. Gangmei, M. Dvornik, R. J. Hicken, J. Grollier, and C. Ulysse, Physical Review Letters **110,** 187202 (2013).

[6] B. Pigeau, C. Hahn, G. de Loubens, V. V. Naletov, O. Klein, K. Mitsuzuka, D. Lacour, M. Hehn, S. Andrieu, and F. Montaigne, Physical Review Letters **109,** 247602 (2012).

[7] W. T. Soh, B. Peng, and C. K. Ong, AIP Advances **5,** 087184 (2015).

[8] P. Hyde, L. Bai, D. M. J. Kumar, B. W. Southern, C. M. Hu, S. Y. Huang, B. F. Miao, and C. L. Chien, Physical Review B **89,** 180404(R) (2014).

[9] B. F. Miao, S. Y. Huang, D. Qu, and C. L. Chien, Physical Review Letters **111,** 066602 (2013).

[10] H. Wang, C. Du, P. Chris Hammel, and F. Yang, Applied Physics Letters **104,** 202405 (2014).

[11] H. Wang, C. Du, P. C. Hammel, and F. Yang, Physical Review Letters **113,** 097202 (2014).

[12] A. Azevedo, O. Alves Santos, G. A. Fonseca Guerra, R. O. Cunha, R. Rodríguez-Suárez, and S. M. Rezende, Applied Physics Letters **104,** 052402 (2014).

[13] R. Engel-Herbert and T. Hesjedal, Journal of Applied Physics **97,** 074504 (2005).

7 Conclusions and future work

We have presented and discussed in detail two main techniques to characterise the magnetic properties of magnetic films in various systems of interest. The two main methods are the transmission line perturbation technique via impedance analysis, and the electrical detection via SRE and ISHE.

In chapter 2, the transmission line perturbation technique is used to investigate the magnetisation dynamics of NiFe films with and without stripe domains. The electrical method is less suitable for this case in part due the skin depth of the microwaves being unable to penetrate thicker films with stripe domains. However, a more important point is that magnetisation state in films with stripe domains is highly dependent on the external field, and thus a measurement in the field domain, as is the primary mode of detection in electrical measurements, is much more complicated to analyse than one done in the frequency domain where the magnetisation state is fixed during each measurement. This is hence, one limitation of the electrical detection of FMR done for such unsaturated films. Regardless, we point out that for saturated films in general, it is still possible to achieve electrical detection of FMR in the frequency domain, provided that one is able to control and account for the frequency-dependent fluctuations in the microwave propagation characteristics of the measurement fixture involved. (Note that in the perturbation method, this is easily accounted for via VNA calibration since it directly measures such propagation characteristics) Therefore, we believe that future efforts to circumvent this issue would be worthwhile to pursue, and hence increase the flexibility and attractiveness of electrical detection of FMR.

In the subsequent chapters, we have demonstrated the sensitivity and feasibility of the electrical method to detect spin dynamics. Firstly, we characterised simultaneously both the

dynamic magnetic and magneto-transport properties of single-layered and obliquely sputtered FeAlSi films via SRE. The results indicate a large dependence of the strength of AMR and AHE on the oblique deposition angle, which suggests the interesting possibility to tune ISHE in heavy metals via oblique deposition as well. Then, we move on to tackle the issue of separating ISHE from SRE voltages in NiFe/Pt bilayer films in order to quantify the spin-conversion efficiency of the Pt layer in a systematic and accurate manner.

Following, we extend our measurement technique to locally and electrically detect spin dynamics via SRE and ISHE in patterned Pt and NiFe films on YIG substrates. We are able to clearly detect and quantify various YIG FMR and surface spin wave modes in the resulting spectra, measured with a homemade shorted coaxial probe. Our results indicate the feasibility for the electrical imaging of spin dynamics using such local probes, whose spatial resolution is only limited by the probe dimensions and the distribution of the microwave fields produced.

Lastly, we showed that electrical detection of spin dynamics via SRE can also be used to detect and quantify both static and dynamic dipolar fields. The dipolar fields are normally extremely hard to detect directly due to its relatively small magnitude and high frequencies. Such a separation and quantification would be immensely useful to study various magnetic systems whereby the dipolar interactions are dominant, such as those in magnonic crystals and spin torque oscillators.

8 Publications

1) Nguyen N. Phuoc, Wee Tee Soh, Guozhi Chai, and C. K. Ong, Journal of Applied Physics **113,** 073902 (2013).

2) Wee Tee Soh, Nguyen N. Phuoc, C. Y. Tan, and C. K. Ong, Journal of Applied Physics **114,** 053908 (2013).

3) Wee Tee Soh, Bin Peng, Guozhi Chai, and C. K. Ong, Review of Scientific Instruments **85,** 026109 (2014).

4) Wee Tee Soh, Bin Peng and C. K. Ong, Journal of Physics D: Applied Physics **47,** 285001 (2014).

5) Wee Tee Soh, Xiaoxi Zhong, and C. K. Ong, Applied Physics Letters **105,** 112401 (2014).

6) Wee Tee Soh, Bin Peng, and C. K. Ong, Journal of Applied Physics **117,** 153903 (2015).

7) Xiaoxi Zhong, Wee Tee Soh, Nguyen N. Phuoc, Ying Liu, and C. K. Ong Journal of Applied Physics **117,** 013906 (2015)

8) Wee Tee Soh, Yasmin Yeow, Xiaoxi Zhong and C K Ong, Journal of Physics D: Applied Physics **48,** 345002 (2015)

9) Wee Tee Soh, Bin Peng, and C. K. Ong, AIP Advances **5,** 087184 (2015).

10) Wenxu Zhang, Bin Peng, Fangbin Han, Qiuru Wang, Wee Tee Soh, Chong Kim Ong and Wanli Zhang, Applied Physics Letters **108**, 102405 (2016).

Appendix

I. Magneto-optical Kerr effect (MOKE) measurements of YIG

In this section, we present the MOKE measurements of our YIG/SiO_2/NiFe samples to obtain the magnetisation curves of the NiFe film. Note that due to the much smaller NiFe film volume as compared to the YIG substrate, it is not possible to obtain this from usual vibrating sample magnetometer (VSM) measurements due to large signal contribution from the YIG layer that overshadows that of the NiFe film. On the other hand, the MOKE setup (Figure A1) using a red laser (wavelength ~600nm) would be ideal for this case due to the limited skin depth of the laser beam into the conducting NiFe layer. At resonance, the skin depth of NiFe is of the order tens of nm and thus, the laser beam typically does not penetrate into and measure the YIG layer.

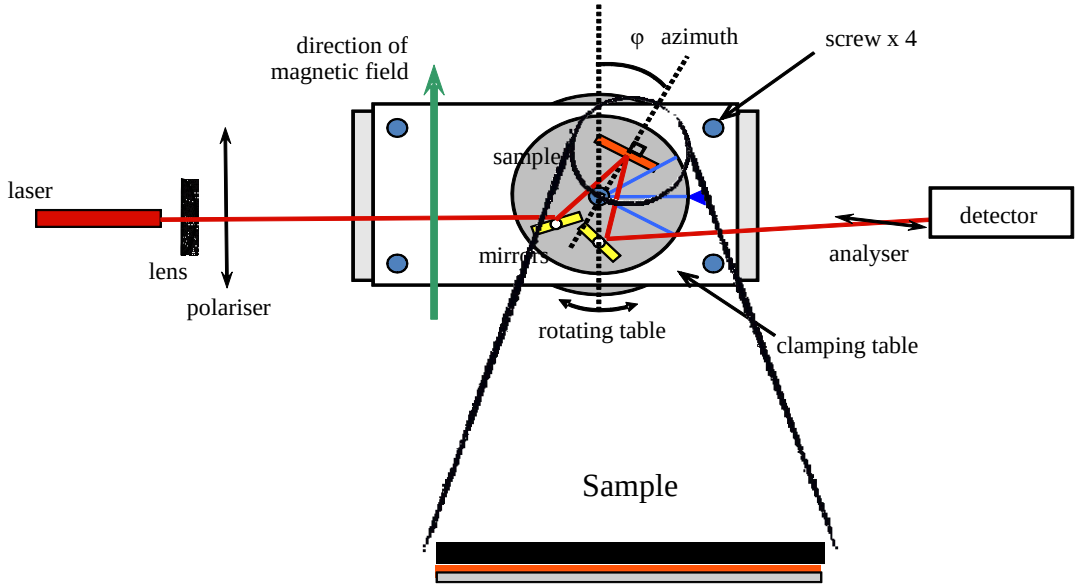

Figure A1 Schematic diagram of the MOKE measurement setup.

The MOKE signal intensity is related[1] to the magnitude of the various magnetisation components. In our measurement setup, the in-plane $M_{in-plane}$ and out-of-plane $M_{out-of-plane}$ components of the NiFe magnetisation as the magnetic field is applied at 45° out-of-plane from the normal can be calculated as

$$\begin{aligned} M_{in-plane} &\propto I_{forward} - I_{reverse} \\ M_{out-of-plane} &\propto I_{forward} + I_{reverse}, \end{aligned} \qquad \text{(A1)}$$

where $I_{forward}$ and $I_{reverse}$ are the MOKE intensities in the forward and reverse geometries (Figure A2) respectively. For sample 1, the corresponding extracted magnetisation components of the NiFe layer are shown in Figure A3. From the results, it is clear that both $M_{in-plane}$ and $M_{out-of-plane}$ have zero remanence. Furthermore, $M_{out-of-plane}$ is almost linear with applied field, which strongly suggest that the NiFe possesses neither perpendicular nor in-plane anisotropy, as the film appears to split into multiple domains at zero field to give a zero net magnetisation.

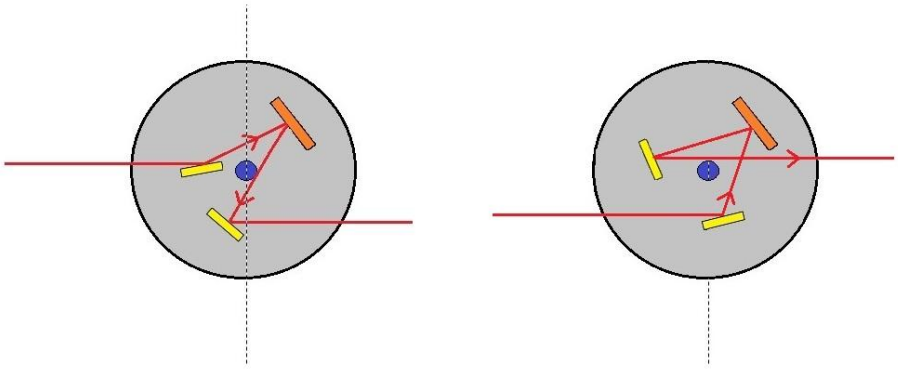

Figure A2 The forward (left) and reverse (right) geometries during the MOKE measurement.

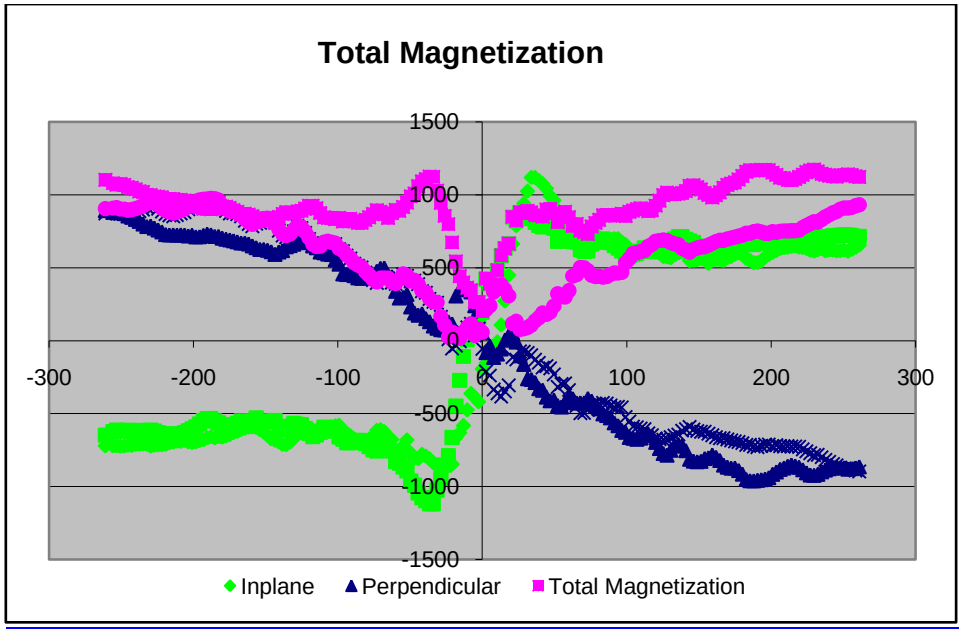

Figure A3 The total magnetisation (in arb. units) against the magnetic field (in mT) applied at 45° incidence out-of-plane from the normal, showing the extracted in-plane $M_{in-plane}$ and perpendicular out-of-plane $M_{out-of-plane}$ components.

[1] John Kerr, "XLIII. On rotation of the plane of polarization by reflection from the pole of a magnet", Philosophical Magazine Series 5, Vol. 3, Iss. 19 (1877).